Ultrafast Laser Interaction for Chemical and Topological Functionalization of Metallic Surfaces

Priya Dominic

N°d'ordre NNT :2023STET056

THÈSE de DOCTORAT
DE L'UNIVERSITÉ JEAN MONNET SAINT-ÉTIENNE
Membre de l'Université de LYON

École Doctorale 488
Sciences Ingénierie Santé SIS

Optique, Photonique, Hyper-fréquences

Soutenue publiquement le 13/12/2023, par :

Priya DOMINIC

Ultrafast Laser Interaction for Chemical and Topological Functionalization of Metallic Surfaces

---

Devant le jury composé de :

Anne-Marie KIETZIG, Professeur, McGill University, Rapporteure

Nadjib SEMMAR, Professeur, Université d'Orléans, Rapporteur

Frédéric CHRISTIEN, Professeur, Ecole des Mines Saint Étienne, Président du jury

Jean-Philippe COLOMBIER, Professeur, Université Jean Monnet, Examinateur

Arnaud WECK, Professeur, University of Ottawa, Co-encadrant de thèse

Florent BOURQUARD, Maître de Conférences, Université Jean Monnet, Co-directeur de thèse

Florence GARRELIE, Professeur, Université Jean Monnet, Directrice de thèse

To,

my loving Mummy & Pappa,

who supported all my decisions

&

never stopped believing in me,

I dedicate you this work

"Experiment is the interpreter of nature. The person who observes anything, whether it was Galileo in the 17th century or a laboratory assistant today, is doing experiments." - Richard P. Feynman

Acknowledgements

It's been four years since I left my hometown, Kerala, a small state in the southern part of India to pursue Ph.D. in Saint Etienne, France. It has been an eventful journey till now when I have finally reached closer to the goal of obtaining the doctorate degree. First and foremost, I am thanking the higher power for blessing me with this opportunity, that led to remarkable experiences and extraordinary people, helping me to learn both personally and professionally. While there were many challenges for me to overcome throughout this journey, I am grateful for the proper guidance and support system that I have received these years. I am extremely grateful to my supervisors for their continuous support, invaluable advice, and immense patience throughout this journey.

Most of all, I want to thank the director of my thesis, Professor Florence GARRELIE for her being an inspiration, significant advice, and enthusiastic encouragement that definitely helped me in staying on the correct track. From the first day of my PhD, she made sure that everything was available for me for the smooth functioning of the thesis. Moreover, I express my gratitude towards her for always being available, for prompt replies, and for frequent meetings despite her busy schedule and her role as the director of Hubert Curien Laboratory.

I would like to express my deep gratitude to the co-supervisor of the thesis Associate Professor Florent BOURQUARD for his immense help from the very beginning of the thesis - starting from administrative procedures to introducing the experimental setups and fruitful discussions. He made sure all my questions regarding the experiments and administrations were answered properly. Thank you for being a wonderful supervisor guiding me through this journey with valuable inputs.

It is with immense gratitude that I acknowledge the support and help of my co-supervisor, Professor Arnaud WECK for his guidance and insights that have helped me to finish the thesis. I thank him for making me feel very welcome at his lab at the University of Ottawa, for his active participation in the weekly meetings, and for arranging all the facilities at uOttawa so that I could do characterizations with other universities in Canada. Thank you for making me a part of your team and also for the timely notifications whenever there was a possibility of an extra funding opportunity.

It gives me great pleasure to acknowledge Professor Jean-Philippe COLOMBIER to whom I am indebted for sharing his wisdom and knowledge, especially on the theoretical part of the thesis. I express my gratitude towards him for his encouraging words and for supporting the thesis with the funds that helped to collaborate with the

University of Ottawa. Thank you for being the 'unofficial supervisor' and the frequent participation in the meetings.

Once again, I thank all my supervisors for making sure that I was comfortable personally, professionally, and financially in my Ph.D., especially with the collaborative travels between France and Canada, in addition to encouraging me to take part in various workshops and conferences that were helpful in accumulating valuable exposure and network-building, all of which will be helpful for my future career. Moreover, I am forever grateful for them to be persistent with me whether it be the preparation of a presentation, writing an article, or my thesis.

I express my sincere thanks to Ms.Stephanie Reynaud of Hubert Curien Laboratory, for her assistance in retrieving high-resolution STEM, many hours of her work in extracting the lamellae, and her valuable inputs to obtain and process the microscopy data and images. I am also grateful to Mr. Nicolas Faure and Mr. Yaya Lefkir for the training on various instruments. I also acknowledge Dr. Gabriele Schatte of Queen's University, Canada, and Mr. Oltion Kodra of the National Research Council (NRC), Canada for their valuable time in extracting the XPS data. I would also like to thank the administrative staff, especially, Patricia Puma and Sandrine Laurent for their efforts in making sure that I have convenient travels to the collaborative visits to Canada and other conferences.

I am deeply grateful to my colleague, Dr. Djafar Iabbaden for his immense contribution in the form of simulations, that provided solid support to various experimental results throughout the thesis. I thank him for his kindness, for all the discussions, and his collaboration to my work. Special thanks to Dr. Anthony Nakhoul for his hard work involved in polishing tungsten samples, whenever I needed them, without which the experiments would not have been possible. I extend my gratitude to Dr. Mathilde Prudent for helping me to get to know not only the lab and the equipments but also exploring France. I am also grateful to Ms. Emilie Laffont for the joint ventures to Canada. I have immense pleasure to thank my colleagues at the University of Ottawa Mr. Graham Jerrey Rivers Killaire, Mr. Xietong Xie, Miss. Shuo Yan, Miss. Katerina Luiza Monea for their kindness and help with the experiments throughout the Ph.D. Thank you Yannick, Gerges, Alexis, Cedric, Erwan, and Florencia for being the best company. Thank you all for being such amazing colleagues and reliable friends that anyone could ask for. Not least of all, I would like to thank my parents, sisters, cousins, relatives, and friends for being a strong support system.

* * *

Abstract

Ultrafast laser irradiation of materials is becoming an important and scalable process in developing new surface functionalizations. This is achieved by manipulating the surface topography and surface chemistry. While surface topography has been extensively explored in recent years, comparatively little work has focused on the accompanying chemical alterations. This thesis contributes to this gap primarily focusing on femtosecond (fs) laser-induced oxidation of tungsten linked with the formation of high spatial frequency laser-induced periodic surface structures (HSFLs). This is achieved by performing experiments in various gaseous and pressure conditions (ambient, air at 10 mbar, nitrogen at 10 mbar, argon at 10 mbar, and vacuum at 10^{-7} mbar) to generate HSFLs of sub-20 nm amplitude and sub-100 nm periodicity. The initial results show a negligible role of oxidation in the formation of HSFLs and suggest a hydrodynamics-based phenomenon. This answers one of the main debates in the scientific community regarding the necessity of oxidation for such nanostructure formation. Our study suggests fs laser-induced Rayleigh-Bénard-Marangoni instability as the main mechanism for the formation of HSFLs, confirmed by observations of subsurface voids. The thesis concentrates on HSFLs generated in ambient and vacuum conditions to differentiate between laser-generated oxides and oxides accumulated on HSFLs over time due to ambient exposure. Interestingly, we observe that laser-generated oxides are crystalline, and oxides accumulated over time are amorphous, a result backed by differences in wettability between the two types of oxides. These results demonstrate the potential for tuning the physicochemical response of laser-irradiated surfaces based on surface chemistry variations. Moreover, the oxidation mechanism accompanying femtosecond laser irradiation is investigated and supported by literature, experiments, and numerical analyses. This approach helped us propose an oxidation mechanism based on a multi-pulse oxide accumulation during laser irradiation governed by the diffusion of oxygen. These results provide an important contribution to the laser-matter interaction community by establishing a time frame for laser-induced oxidation and proposing a way to control oxidation via ultrafast laser irradiation.

Keywords: Femtosecond lasers, nanostructures, surface chemistry, oxidation, vacuum, HSFLs, Rayleigh-Bénard-Marangoni instability, TTM-MD, tungsten, polymorphism, wettability.

* * *

Résumé

L'irradiation ultra-rapide au laser des matériaux devient un élément clé du développement de nouvelles fonctionnalisations de surface. Cela est réalisé en manipulant la topographie de surface et la chimie de surface. Alors que la topographie de surface a été largement explorée ces dernières années, relativement peu de travaux se sont concentrés sur les altérations chimiques qui l'accompagnent. Cette thèse comble principalement cette lacune en se concentrant sur l'oxydation induite par laser femtoseconde (fs) du tungstène liée à la formation de fréquentes ondulations de haute fréquence (High Spatial Frequency Laser induced periodic surface structures (HSFL)). Cela est réalisé en effectuant des expériences dans diverses conditions gazeuses et de pression (ambiante, air à 10 mbar, azote à 10 mbar, argon à 10 mbar et vide à 10^{-7} mbar) pour générer des HSFL d'amplitude inférieure à 20 nm et de périodicité inférieure à 100 nm. Les premiers résultats montrent le rôle négligeable de l'oxydation dans la formation des HSFL, mais sont significativement guidés par des phénomènes hydrodynamiques. Cela répond à l'un des principaux débats au sein de la communauté scientifique concernant la nécessité de l'oxydation pour la formation de ces nanostructures HSFLs. Cette étude suggère que l'instabilité Rayleigh-Bénard-Marangoni induite par laser fs explique bien à la formation des HSFL, comme le confirme l'observation de nano-cavits en sous-surface associés à celles-ci. De plus, la thèse se concentre sur les HSFL générées dans des conditions ambiantes et sous vide pour différencier entre les oxydes générés par le laser et les oxydes accumulés au fil du temps en raison de l'exposition à l'ambiante. De manière intéressante, nous observons que les oxydes générés par le laser sont cristallins, tandis que les oxydes accumulés au fil du temps sont amorphes, ce qui est également confirmé par la différence de mouillabilité entre les deux types d'oxydes. Cela ouvre la voie à la possibilité de régler la réponse physico-chimique des surfaces irradiées par laser en fonction des variations de la chimie de surface sur la même topographie de surface (HSFL sur W). De plus, le mécanisme d'oxydation accompagnant l'irradiation laser femtoseconde est étudié en utilisant la littérature, des analyses expérimentales et numériques. Cette approche nous aide à proposer une accumulation d'oxydes par les multiples impulsions laser successives, gouvernée par la diffusion de l'oxygène. Cela constitue une contribution essentielle à la communauté scientifique, car cette étude établit la temporalit de l'oxydation induit par laser, ce qui est un aspect important de l'interaction laser-matière, en plus de proposer un moyen de contrôler l'oxydation qui accompagne l'irradiation laser ultra-rapide.

Mots-clés: Lasers femtosecondes, nanostructures, chimie de surface, oxydation, vide, HSFL, instabilité Rayleigh-Bénard-Marangoni, TTM-MD, tungstène, polymorphisme, mouillabilité.

* * *

Contents

List of Figures

* * *

List of Tables

* * *

Nomenclature

List of Abbreviations

AES: Auger electron spectroscopy

AFM: Atomic force microscopy

a-LIPSS: Anomalous LIPSS

BSE: Back scattered electron

CA: Contact angle

CPA: Chirped pulse amplification

CW: Continuous wave

EDX: Energy dispersive X-ray spectroscopy

EAM: Embedded atom model

EELS: Electron energy loss spectroscopy

EM: Electromagnetic

FEPA: Federation of European producers of abrasives

FDTD: Finite difference time domain fs: Femtosecond

FFT: Fast fourier transform

GD-OES: Glow discharge optical emission spectroscopy

HAADF: High angular annular dark field

HR: High resolution

HSFL: High spatial frequency LIPSS

LIPSS: Laser-induced periodic surface structures

LSFL: Low spatial frequency LIPSS

MD: Molecular dynamics

NSE: Navier Stokes equation

ns: Nanosecond

n-LIPSS: Normal LIPSS

PIC: Particle in cell

PLD: Pulsed laser deposition

ps: Picosecond

RSTT: Reciprocal sliding tribological tests

SAD: Selected area diffraction

SEM: Scanning electron microscopy

STEM: Scanning transmission electron microscopy

SE: Secondary electron

SEW: Scattered electromagnetic wave

SERS: Surface-enhanced Raman spectroscopy

SPP: Surface plasmon polarioton

TEM: Transmission electron microscopy

TE-SSW: Transverse electric scattered surface wave

TTM: Two temperature model

TTM-MD: Two temperature model- molecular dynamics

TLIPSS: Thermochemical laser-induced periodic surface structures

TM-HPW: Transverse magnetic hybrid plasmon wave

TTIPSS: Thermochemical tip-induced periodic surface structures

UV: Ultraviolet

WCA: Water contact angle

WDM: Warm dense matter

XPS: X-ray photoelectron spectroscopy

* * *

Introduction

As this thesis begins, this section consists of a short introduction to the thesis. Initially, it establishes the background of the thesis, and the scope of the subject, followed by the main questions to be addressed, and finally, a synopsis of different chapters.

Lasers are becoming an inevitable component in the precise modification of material surfaces for various scientific and technological advances. This is due to the directionality and coherence of a laser beam that enables the control over localized modification of surfaces. Hence, laser-matter interactions have been extensively studied in the past decades, revealing their wide potential for one-step functionalization of surfaces. Lasers can be used to produce topographic and chemical functionalization of surfaces. Topographic functionalization depends on various structural modifications that can be attained ranging from a few nanometers scale to micrometers scale. These kinds of structures are broadly explored regarding their origin, types, applications etc. Even though the influence of laser-generated surface chemistry on materials used in various industrial applications cannot be ignored (e.g. tribology [1, 2], thermal properties [3, 4], color marking [5] etc.), discussions on laser-induced surface chemical alterations are limited. This calls for a detailed study of ultrafast laser-induced surface chemical alterations.

Laser-induced surface chemistry is material dependent and its mechanisms may not be applicable to other materials. There are various ways to investigate laser-assisted surface chemistry. The most common chemical change observed during laser irradiation of metals is the formation of laser-generated oxides [6, 7, 8]. This is what we will be focusing on in this thesis. When we look at past works, continuous wave laser-matter interactions and nanosecond laser-matter interactions are comparatively more explored for their oxidation mechanisms [9, 10]. However, femtosecond interactions are different from continuous wave and nanosecond interactions, considering that the femtosecond pulse duration is shorter than the electron-phonon relaxation time, expansion time induced by lattice heating, and the resulting direct solid-vapor transition [11].

The final response of the surface depends not only on morphology but also on chemistry hence it is important to understand the oxidation mechanism during laser irradiation. A thorough review of the literature will allow us to identify the major questions to be answered and to address the more often ignored context of laser-induced surface chemistry.

The following are some of the main questions we will be addressing in this thesis:

- **What is the influence of oxidation on the formation of nanostructures - Is it a necessary factor for nanostructure formation?**
- **When does oxidation take place? - Is it possible for the laser-induced temperatures lasting only a few nanoseconds to cause oxidation, considering the very short time period of the fs laser pulse?**
- **What is the mechanism of laser-induced oxidation?**
- **Is it possible to control ultrafast laser-assisted oxidation?**

The thesis can be outlined as follows,

Chapter 1, 'Ultrafast Laser Matter Interactions & Role of Surface Chemistry' introduces different concepts and literature that form the basics for the thesis. This chapter begins with a detailed discussion of the mechanisms of ultrafast laser-matter interaction. It details the absorption, relaxation, melting, ablation, and resolidification associated with ultrafast laser-matter interactions. This is followed by an analysis of the different types of nanostructures that can be achieved on the surfaces by femtosecond laser irradiated materials. Later, the different types of theories that are proposed for the formation of nanostructures like the electromagnetic theories, self-organization theories, and oxidation-based theories are reviewed. In addition, different numerical models including the finite difference time domain (FDTD), particle in cell (PIC), and two temperature model-molecular dynamics (TTM-MD) simulations that are used for understanding the mechanisms involved with ultrafast laser-matter interactions are reported. Various applications of laser-induced periodic structures are presented. The second part is on surface chemistry due to laser-matter interactions with discussions focusing on the aging after laser irradiation and the significance of laser-assisted oxidation in the final response of the material. This is followed by discussions on the various literature available on the oxidation mechanisms accompanied by laser-matter interactions. In the final part, a detailed description of the motivations for this work is given.

Chapter 2, 'Experimental Methods' provides a detailed view of the instrumentation and techniques utilized in the thesis. It details sample preparation, laser irradiation, vacuum system, and various microscopy and spectroscopy characterization techniques such as SEM (scanning electron microscopy), AFM (atomic force microscopy), STEM (scanning transmission electron microscopy), STEM-EDS (STEM-energy dispersive X-ray spectroscopy), STEM-EELS (STEM- electron energy loss spectroscopy), XPS (X-ray photoelectron spectroscopy) and contact angle measurements that are used in the thesis.

Chapter 3, 'Oxidation - a precondition for LIPSS formation?' begins with an analysis of the different types of nanostructures that can be generated on tungsten (W). Topography characterizations are performed for periodic structures generated in tungsten for ambient air, and other gaseous conditions like argon, nitrogen, and vacuum. Later on, the influence of oxidation on nanostructure formation (HSFLs) on W is analyzed with SEM, AFM, and STEM analyses. This leads us to the conclusion that HSFLs have more of a hydrodynamics-based origin rather than an oxidation-based origin. Subsurface cavitation obtained by STEM images and TTM-MD

simulations back up this result.

Chapter 4 'Establishing Ultrafast Laser-assisted Oxidation Mechanism for HSFLs on Tungsten' is the second and main chapter of the results. This chapter focuses on establishing an oxidation mechanism on W during HSFL formation. This is done by differentiating laser-generated oxide from oxides accumulated over time under ambient exposure. The main results are based on a comparison between the wettability results and XPS analyses. Crystal indexing from STEM images reveals crystalline tungsten oxides and hints to the roles of polymorphism in oxide formation. TTM-MD analysis is used obtain the time scale of temperature evolution during ultrafast laser irradiation, which is an important factor in establishing a proper oxidation mechanism based on classical oxidation literature.

Finally, the main conclusions and perspectives for future work are given.

This thesis is a collaboration between the Hubert-Curien laboratory (Laser matter interaction team) of Jean Monnet University, Saint-Etienne, France, and CRPuO (Centre for Research in Photonics) at the University of Ottawa (uOttawa), Canada. The SEM and AFM facilities at both universities were helpful in extracting topography information. The STEM-imaging, EDX, and EELS facilities at labHC contributed to the sub-surface imaging and surface-sensitive characterization. These results were confirmed by the wettability measurements and XPS analyses accessible from uOttawa. In addition, the TTM-MD simulations to support our experimental evidence were carried out by Dr. Djafar Iabbaden of Hubert Curien laboratory under the supervision of Prof. Jean-Philippe Colombier. The polishing of the sample was done at Ecole des Mines de Saint-Étienne, with the help of Dr. Anthony Nakhoul.

* * *

Chapter 1

Ultrafast Laser Matter Interactions & Role of Surface Chemistry

"Because the high-intensity pulses are short, the laser only damages the area where it's applied. The result is precise, clean cuts that are ideal for transparent materials."
-Donna Strickland, 2018 Nobel laureate in Physics

"We should see extensions to studies of the femtosecond dynamics of single molecules and of molecules on surfaces"
-Ahmed Zewail, 1999 Nobel laureate in Chemistry

This chapter will establish a literature background of laser-matter interactions, specifically that of ultrashort laser, and the significance of surface chemistry modifications associated with it. The first section will discuss the fundamentals of ultrafast laser and the mechanisms involved in ultrafast laser-matter interactions. In the second section will cover the different types of laser-induced topographies achieved by laser surface structuring, the different modeling approaches proposed to explain them and their industrial applications. This section highlights the role of both laser-induced topography and laser-induced surface chemistry in the final physicochemical response of the material. Later, the chapter focuses on the different surface chemical modifications achieved with a laser. The most common laser-assisted surface chemical modifications are detailed with a review of the oxidation mechanisms proposed for lasers of different pulse duration. Finally, the main objectives of this work are outlined.

1.1 Fundamentals of Ultrafast Lasers

LASER (Light Amplification by Stimulated Emission of Radiation) are devices that generate and amplify light of various wavelengths ranging from far infrared to X-ray region in the electromagnetic (EM) spectrum [12]. There are of two kinds: Continuous Wave (CW) and pulsed lasers. In general, due to their coherence, monochromaticity, and directionality, lasers have a wide variety of applications. CW laser are used for cutting, welding, engraving, and drilling [13]. They are easy to maintain and are efficient. However, their output peak power is small compared to pulsed laser. Hence pulsed lasers are used for micro-machining, medical applications, and spectroscopy [14, 15, 16]. Nowadays, ultrafast lasers (with light pulses having a duration of 5 fs to 100 ps) are popular for various industrial applications since they can generate fine cuts with sharp edges, no micro-cracks, and reduced debris enabling precise processing as shown in figure 1.1 (a).

Femtosecond lasers are advantageous since they can interact with any materials and can become reasonably wavelength insensitive. Also, the shorter pulses and nonlinear interactions give rise to better edge quality and precision [17, 18, 19, 20, 21, 22, 23]. These pulses are generated by using a specific technique called Chirped Pulse Amplification (CPA) [24], where an initial nanosecond pulse is stretched, amplified, and re-compressed, resulting in a femtosecond laser pulse as can be seen from figure 1.1 (c). Femtosecond lasers can be of many kinds. They can be solid-state lasers, fiber lasers, dye lasers, or semiconductor lasers. Solid state lasers like Titanium-sapphire lasers can emit laser pulses with a duration below 10 fs and with powers as high as several megawatts. The specialties of femtosecond laser make it very advantageous for novel applications (figure 1.1 (b)) that enable the observation and manipulation of the ultrashort process in biology, chemistry, etc. [23, 25].

1.2 Ultrafast laser interaction with metals

1.2.1 Absorption and relaxation of laser energy

The first step involved in laser-matter interaction is the absorption and reflection (if any) of light energy by the solid-state material. Depending on the material, the nature of the absorption and reflection varies. This thesis will focus on metals, because of their high optical absorption properties and potential applications.

Various factors affect the initial absorption of light energy on metal, including surface roughness, native oxide layer, hydrocarbon contamination adsorbed from the atmosphere, etc., in addition to some part of this energy being reflected by the surface of the metal.

The absorption of laser light on metallic surfaces takes place via free electrons through the inverse bremsstrahlung mechanism. It is the process where an electron absorbs a photon while colliding with another electron or ion, and the total energy is conserved. In the case of transition metals, electron excitation to the conduction band also takes place during photon absorption.

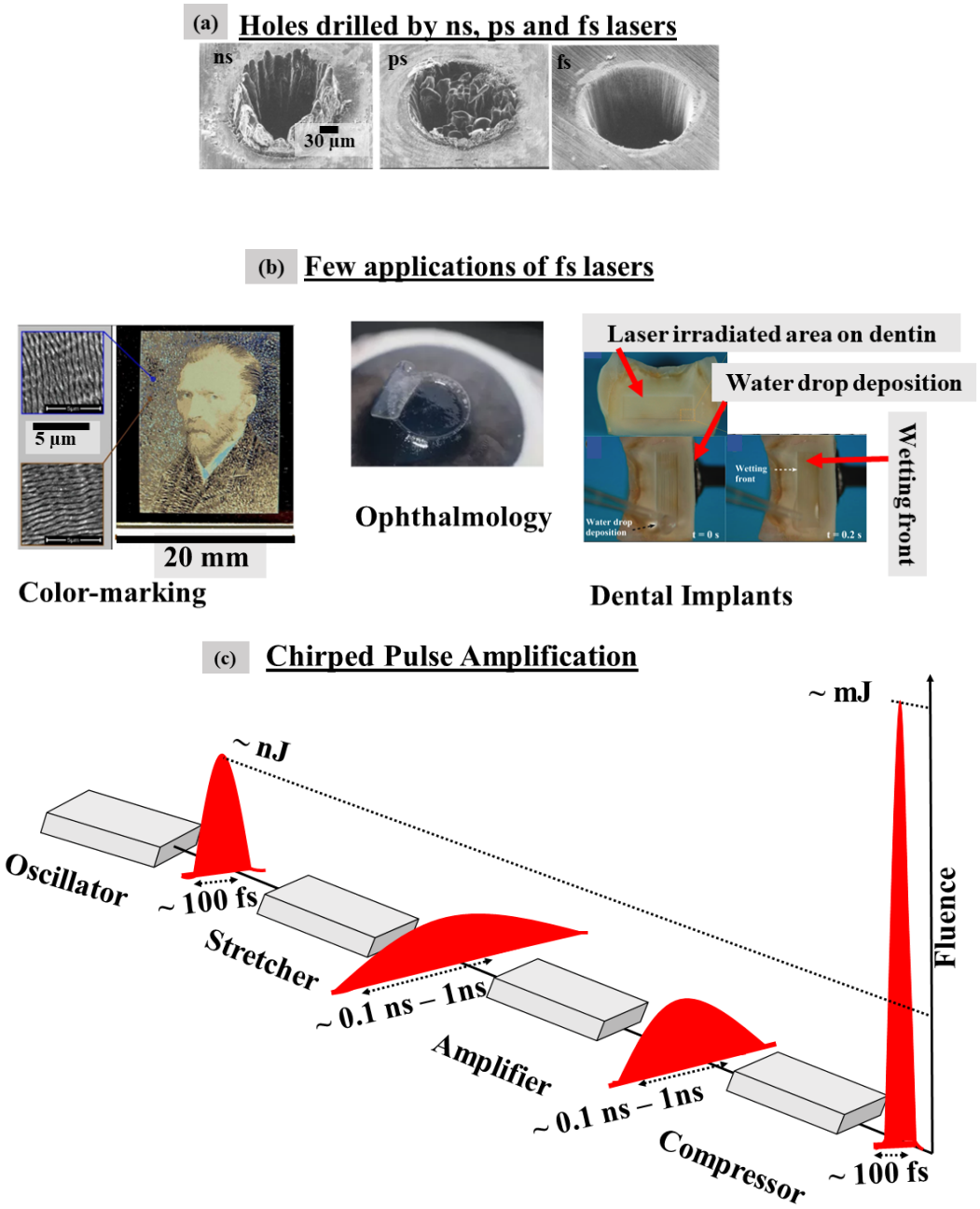

Figure 1.1: Holes drilled by using ns, ps, and fs laser on the surface of the steel, adapted from [26]. (b) Applications of fs lasers in color marking (adapted from [26]), ophthalmology (adapted from [15]), and dental implants (adapted from [16]). (c) Chirped pulse amplification used in fs laser.

Once absorbed, the intensity of the light I(z) exponentially decays along the depth (z), depending upon the absorption coefficient (α), given by the Beer- Lambert's law [27]:

$$I_z = I_0 e^{-\alpha z}, \tag{1.1}$$

where I_0 is the intensity at the surface after reflection. The optical penetration depth or skin depth, δ, is defined as the inverse of the absorption coefficient, α, and is the distance at which the intensity of the light drops to $1/e$

of its initial value at the surface. The skin depth is given by,

$$\delta = \frac{\lambda}{4\pi k}. \tag{1.2}$$

For an ultrafast laser-irradiated tungsten (W) sample (as the one used in this thesis), a laser wavelength of 800 nm and extinction coefficient, k =2.9, result in a skin depth δ of 25 nm [28, 29].

Ultrafast laser-matter interaction with metals can be categorized into three time-intervals. While these time frames are well-established in the scientific community as shown in figure 1.2, the time frame for surface chemical changes accompanying the laser-matter interactions is yet to be explored. Initially, upon laser excitation, the electron system will be in non-equilibrium. This time frame involves the ballistic motion of electrons and the collision of excited electrons with other surrounding electrons to achieve a thermal equilibrium between the electrons. The second time interval is governed by electron-phonon coupling and can be described by the Two Temperature Model (TTM) as discussed in the coming sections. In the final time frame, after electron-lattice thermal equilibrium is achieved by heat exchange between two systems, melting and ablation can then take place giving rise to surface structures [30].

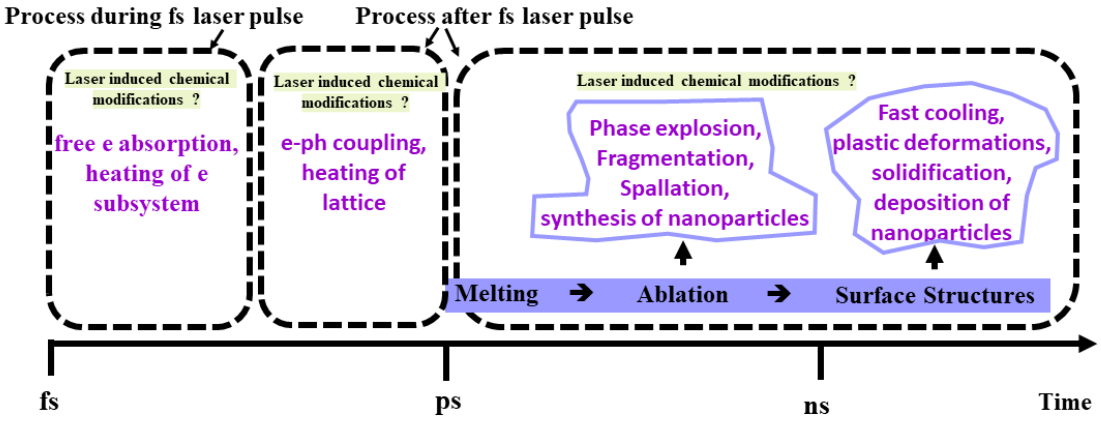

Figure 1.2: Time scales involved in fs laser irradiations for energy transfer, material relaxation, and cooling (inspired from [31] and [30]).

Transient state of materials

The transient state of the material upon ultrafast laser irradiation is defined as follows. Ultrafast laser pulses cause high-speed material excitation which is faster than the material relaxation time giving rise to isochoric heating of free electrons. The heated surface layer is typically 10 nm to 20 nm for metals, equivalent to the optical penetration depth. In a plasma hypothesis, the expansion velocity is given by,

$$v_s = \sqrt{\gamma_e N_e k_B T_e / M_i}, \tag{1.3}$$

where M_i is the mass of the ion, N_e is the number of free electrons per atom, k_B is the Boltzmann constant, T_e is the electron temperature, γ=3 is the adiabatic constant of a solid [32]. This expansion velocity for the laser-irradiated surface layer is closer to the speed of sound ($\sim$ 5000 ms^{-1}) during 100 fs. In the regime of solid-density electron heating, the kinetic energy of electrons corresponds neither to conventional matter nor the plasma physics regime. Hence, the term Warm Dense Matter (WDM) [33, 34] has emerged to describe this regime. In this regime, the density of the material goes from an order of magnitude below that of the solid (ρ_0/10) to ten times its value, (10 ρ_0). The temperature varies up to a few tens of eV. Figure 1.3 (a) shows the thermodynamic regime upon ultrafast laser irradiation [35]. Our focus in this work is on LIPSS formation on metals, so the regime is located at the solid-liquid transition and is not supposed to go beyond the liquid-gas binodal line.

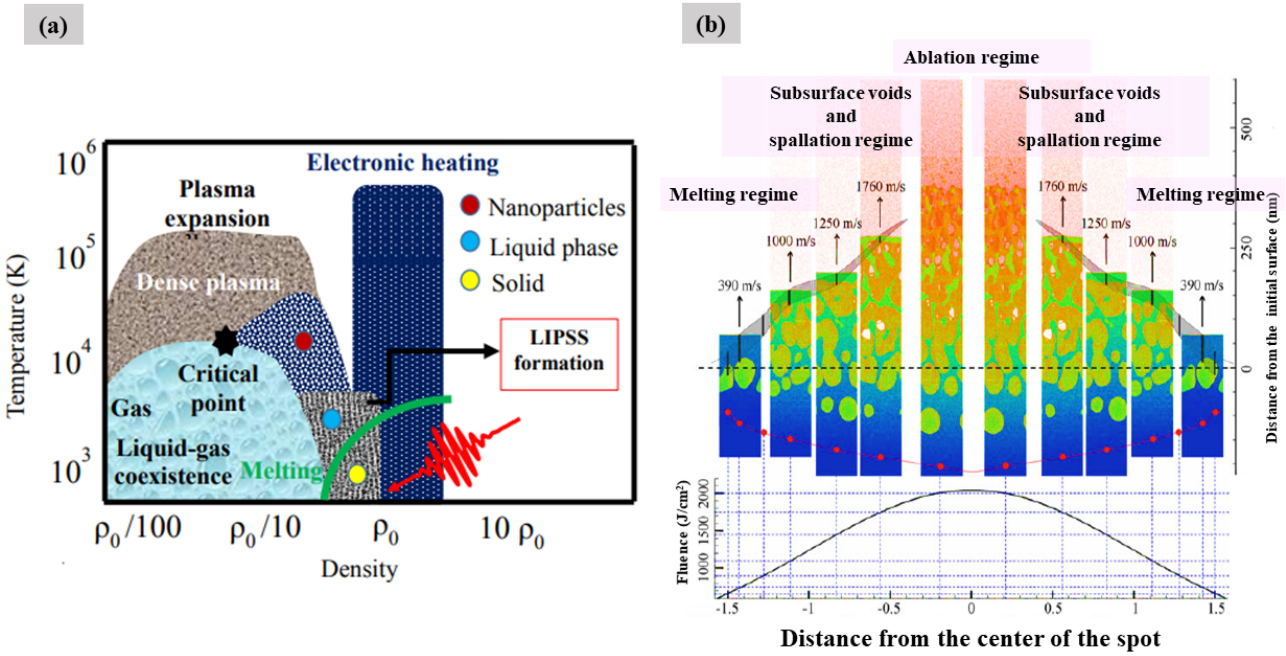

Figure 1.3: (a), Thermodynamic diagram representing the transient phases achieved by the material as a result of ultrafast laser irradiation as adapted from [35] (b), Molecular Dynamics simulations showing the evolution of Al surface as a result of 100 fs laser irradiation, adapted from [36].

1.2.2 Laser induced melting and ablation

As the energy deposited on the metal is absorbed by the electrons and transferred to the lattice, ablation takes place, which is the removal of material from the surface. Mechanisms driving laser ablation are strongly dependent on laser fluence. It involves melting and resolidification at lower fluences, cavitation and spallation regimes as the fluence increases and explosive boiling at higher fluences [36] as shown in figure 1.3 (b). In this work, we are focusing on LIPSS, which usually occur between the melting and ablation regimes. Specifically, we are interested in high-frequency LIPSS (HSFLs), that exist in the melting regime.

Usually, for slow normal heating (when the heating time is longer than the time needed for the melting front to pass through the heated region), heterogeneous melting occurs [37, 38], where the nucleation of the

liquid melt happens at the surface and around crystal defects, at the melting point of the material. This melting front travels into the bulk of the crystal and requires almost a nanosecond to reach the melting depth. However, the heating rates associated with fs laser irradiation (10^{14} K/s and higher [39]) are very high and hence move faster than the heterogeneous melting front. Therefore, fs laser irradiation is dominated by homogeneous melting [40, 39], which is a volumetric process where random nuclei of melt appear and join together as shown in figure 1.4. Laser-induced removal of material can occur in various forms including normal boiling, normal evaporation,

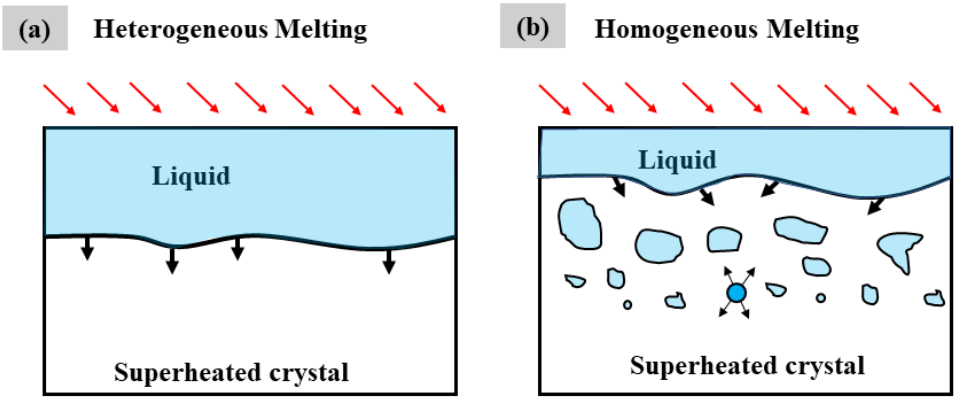

Figure 1.4: Schematic illustrations of (a) heterogeneous melting process and (b) of laser-induced melting where homogeneous nucleation occurs ahead of the melting front, illustrations inspired from [37].

spallation, or phase explosion. The specific mechanism usually depends upon the laser pulse duration and fluence. For ultrashort laser pulses, spallation and phase explosion dominate as discussed below.

1.2.3 Laser induced stress waves and nucleation

Laser irradiation is accompanied by the build-up of strong mechanical stresses. The rapid localized energy deposition of fs laser pulses results in the generation of mechanical stresses in the material. They can be categorized as (1) dynamic transient stresses and stress waves due to stress confinement, (2) thermo-elastic stresses due to temperature gradients, and (3) residual stresses due to the structural changes in the material [38]. Since the time scale for mechanical relaxation of the heated material is longer than the laser pulse duration there will be high-stress confinement and hence generation of compressive stresses. Rapid melting of the surfaces also adds to this compressive stress which will propagate into the bulk of the target. A tensile wave is also generated as a result of material relaxation, which will be traveling in the opposite direction to this compressive wave, resulting in cavitation bubbles in the molten material. These cavitation bubbles can either collapse, be frozen upon resolidification leading to surface swelling, or grow and join together leading to photo-mechanical spallation, which will separate the molten part from the material [41, 42, 43]. This is visualized using simulations as shown in figure 1.5.

Photo-mechanical spallation is the separation or ejection of the molten layer due to the relaxation of the photo-mechanical stresses and the creation and coalescence of vapor nuclei [44, 36]. For a higher energy deposition, when a liquid is heated beyond its melting point into a super-heated meta-stable thermodynamic state, a rapid

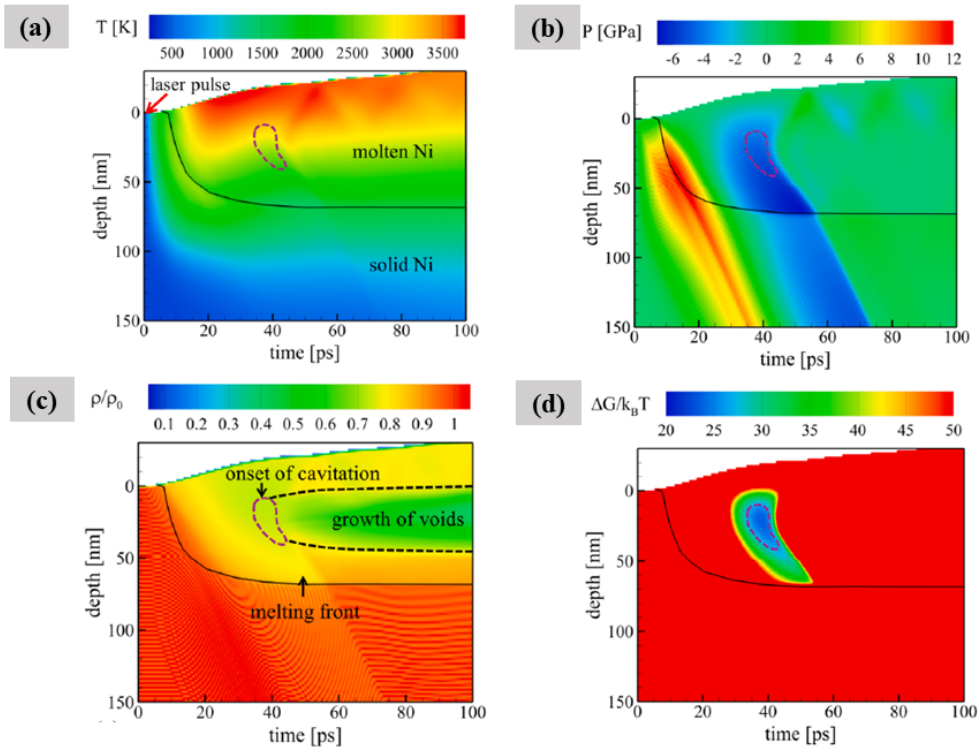

Figure 1.5: Temporal and spatial evolution of temperature (a), pressure (b), density (c) free energy barrier for the onset of cavitation (d) inside femtosecond laser irradiated bulk Ni. The solid-liquid interface is outlined by the black line. Figure (b) shows the compression (red) and rarefaction wave (blue) inside the target. The region enclosed in purple dotted lines is the region of nucleation for cavitation having a free energy barrier below 25.5 K_BT as theoretically predicted and as seen by the simulations [43], (pictures adapted from [43]).

phase transition to the vapor state occurs, resembling an explosion, and is called phase explosion or explosive boiling [36, 38]. This arises when the laser-induced super-heating of the melt leads to a rapid phase transition to vapor, like an explosion.

For a spherical cavity in the regime of photo mechanical spallation, the Gibbs energy change, ΔG is zero at the critical radius r_c of the void for the onset of cavitation [38],

$$(\frac{d\Delta G}{dr})_{rc} = 0, \tag{1.4}$$

where,

$$\Delta G = P_l V + \gamma_{lv} A \tag{1.5}$$

where P_l and γ_{lv} are the pressure of the liquid and the surface tension of the liquid-vapor interface. V and A are the volume and area of the cavity of radius r, respectively. In the phase explosion regime, equation 1.5 will also include P_v, the vapor pressure as $P_l - P_v$ instead of just P_l.

The cavity nucleation rate can be given as,

$$R = R_0 \; exp(-G_0/k_B T) \tag{1.6}$$

Where R_0 is expressed in nuclei per second per cubic meter, k_B and T are Boltzmann constant and temperature respectively. For instance, in the case of Al and Au [45, 46], this rate is found to be around 10^{34} $s^{-1}m^{-3}$, with a nucleation-free energy barrier $G_o^{th} \sim$ 23 $k_B T$. Hence, the temperature dependent threshold for cavitation by tensile pressure is given as,

$$P_{th}^2 \propto \gamma_{lv}^3 / T \tag{1.7}$$

While the laser-induced stresses come back to zero, the thermo-elastic stresses cannot completely relax due to the constrictions in the lateral direction by the surrounding material. As a result, some residual compressive stresses may remain after resolidification, until the temperature drops to room temperature. This lateral compression can give rise to vacancies and dislocations during cooling [47, 48].

1.2.4 Resolidification

As the laser-induced heat conducts into the bulk of the sample, cooling takes place. This cooling rate can be as high as 10^{12} K/s [49], especially for metals due to their high conductivity. This leads to strong under-cooling and very rapid resolidification. Depending on the material and irradiation conditions, simulations show that for ultrafast laser irradiations melting and resolidification of metals occur in a time span of a few nanoseconds [50, 51]. This rapid solidification can control surface phase composition and homogenization, generation of crystal defects, size and distribution of grains, and complex surface morphology [52]. Surface amorphization using laser pulses has been observed for crystalline Al-Cu-Ce alloy [53]. Various defects like twin boundaries for Ni [51] and vacancy formations in Fe-Ni alloy [49] are reported as a result of the fast-moving melt front. Since ultrafast laser irradiation can result in a thin nanolayer of melt, the deep under-cooling can result in nanograins of random crystal orientation accommodating various defects like high-density twin boundaries resulting in high strength and ductility [38, 54, 55, 56] as shown in figure 1.6. The final surface roughness of a laser-irradiated Cr crystal has been shown to depend on the velocity of the solidification front and crystal orientation [57].

1.3 Laser Induced Topographies

1.3.1 Types of nanostructures: LIPSS

Laser-Induced Periodic Surface Structures or LIPSS are the most typical kind of laser-induced nanostructure. As the name suggests, they are laser-induced nano/micro-structures having a particular period and are usually found to be oriented in a specific direction with respect to laser polarization. There are various types of LIPSS: they can be ripple-like structures commonly called low spatial frequency LIPSS (LSFLs) or high spatial frequency LIPSS (HSFLs) or they can be grooves, spikes, nano pits, or nano peaks as shown in figure 1.7. In most cases, their period (Λ), orientation, and type can be controlled by polarization, irradiation wavelength (λ), fluence, and

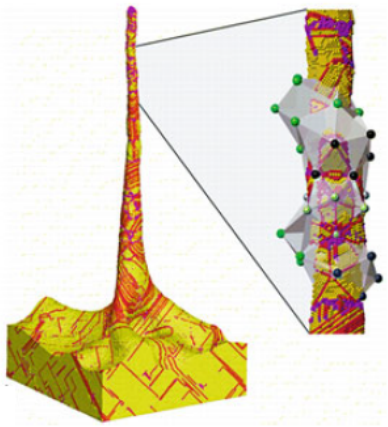

Figure 1.6: Frozen nanospike generated in fs laser irradiated Ag by simulations where the yellow atoms correspond to FCC structure, red represents stacking faults and twin boundaries, and purple stands for other kinds of defects, adapted from [56].

number of laser pulses.

The most common LIPSS are low spatial frequency LIPSS or LSFLs and high spatial frequency LIPSS or HSFLs. LSFLs have periods larger than half the wavelength of the laser used (figure 1.7 (d)) and HSFLs have smaller periods, less than half the wavelength of the laser used (figure 1.7 (a)). LSFLs can be perpendicular (LSFL-I) (figure 1.7 (e)) or parallel (LSFL-II) to the polarization of the laser beam (figure 1.7 (f)). Depending on their depth-to-period aspect ratio (A), HSFLs can either be deep HSFL, HSFL-I (A $>$ 1), perpendicular to laser polarization (figure 1.7 (b)) or shallow HSFL, HSFL-II (A$<$1), parallel to the laser polarization (figure 1.7 (c)) [58]. Local laser fluence highly influences the formation of LIPSS and for metals, generally, the period of LIPSS (especially for LSFLs) decreases with an increase in the number of pulses with the inter-pulse feedback effects considerably influencing the morphology of the LIPSS. As mentioned earlier, the polarization of the laser beam mainly influences the orientation of LIPSS, making it parallel or perpendicular to the electric field vector of the laser beam. While the wavelength of the laser beam can be used to control the period of LIPSS, they are not significantly influenced by the laser pulse duration. Moreover, the angle of incidence of the laser beam affects the LSFL period but does not significantly affect the HSFLs period.

In addition to LSFLs and HSFLs, the other kinds of LIPSS obtained at higher fluences like grooves are oriented usually parallel to laser polarisation (figure 1.7 (g)) and have a size of a few micrometers, whereas spikes are more irregular and have negligible relation to the laser polarisation (figure 1.7 (h)).

There are recent reports of self-organised periodic structures with smaller dimensions, up to ten times smaller than conventional LIPSS, like nanocavities and nanobumps [59, 60] as shown in figure 1.7 (i).

The origin of these nanostructures has been explored widely and many theories based on electromagnetic

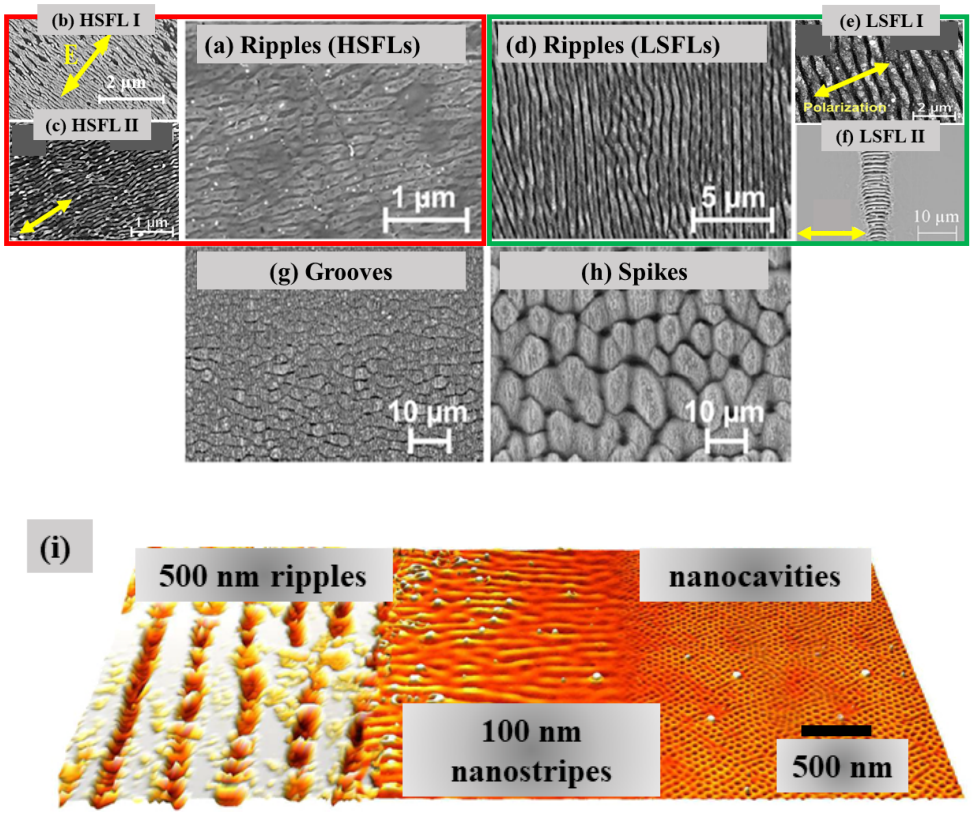

Figure 1.7: Various types of LIPSS that can be generated. SEM images of - HSFLs (a)-(c): on steel (a), Indium oxide film (b), and Ti (c). LSFLs (d)-(f): on steel (d), Ti (e), and fused silica (f). Grooves (on steel) (g) and Spikes (on steel) (h). AFM image of self-organized nanostructures produced on nickel (i) such as ripples, nano stripes, and nanocavities by femtosecond laser irradiation.((a)-(i) adapted from [61, 62, 63, 60])

models, hydrodynamic phenomena, and surface oxidation have been put forward to explain the formation of LIPSS.

1.3.2 Theories proposed for LIPSS formation

Electromagnetic theories

The most widely accepted theory on LIPSS formation is the electromagnetic theory as put forward by Emmony et al. [53] and later developed by Sipe, which is based on the interference of scattered electromagnetic waves (SEWs) from surface roughness. The idea is simply illustrated in figure 1.8. When a laser beam interacts with the material surface, it is scattered by roughness in the material. In addition to this, other surface modes also get excited such as surface plasmon polaritons (SPPs), which are electromagnetic (EM) waves that propagate along the metal-dielectric interface arising from delocalized coherent electron density oscillations [64]. These SEWs and SPPs will interfere with the incoming laser beam, giving rise to an interference pattern, and spatially modulating the intensity [65]. This gives rise to spatially modulated removal of the material from the surface, resulting in LIPSS, a term put forward by Van Driel et al. [66]. Sipe and his co-workers put forward an analytical approach to analyze the interaction of the electromagnetic (EM) wave with the surface roughness by introducing a scalar

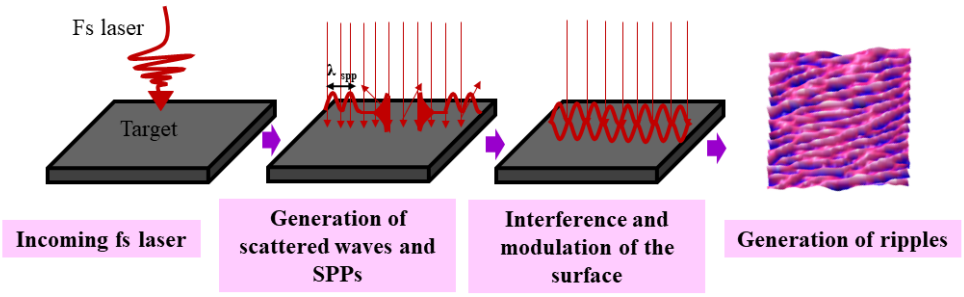

Figure 1.8: LIPSS formation based on the electromagnetic model (image inspired from [67])

factor proportional to the inhomogeneous energy absorption, called the efficacy factor, η [68]. The relation is given by [68], $A \propto \eta \times |b|$, where b is the Fourier spectrum of surface roughness and η is the efficacy with which the surface roughness leads to the inhomogeneous energy absorption. This theory was able to predict the period of LIPSS by considering the laser and surface parameters.

Later Skolski et al. [69] put forward a numerical approach based on Finite Difference Time Domain (FDTD) (as we will discuss in the next section) that confirmed the Sipe model. Even though Sipe's approach successfully predicted the formation of LIPSS to some extent, they were not able to incorporate the pulse-by-pulse feedback mechanisms influencing the topography.

Self-organization theories

Matter reorganization theories are based on the laser-induced melt flow governed by hydrodynamic instabilities, which will transport the melt and rearrange the surface morphology as shown in figure 1.9. These self-organization regimes are triggered depending on the laser parameters, initial surface conditions, and inhomogeneous response of different crystal orientations. The role of hydro-dynamic effects is detailed by various groups considering surface tension dependence on temperature or recoil pressure. Surface tension dependence on temperature gives rise to the Marangoni effect or thermocapillary forces. The hydrodynamic flow at the surface can be computed by using the Navier-stokes equation (NSE) in combination with the continuity equation, in space and time [65]. The NSE equation is given by [70],

$$\frac{\partial \rho \vec{u}}{\partial t} + (\vec{u}.\nabla)(\rho\vec{u}) + (\rho.\vec{u})\nabla.\vec{u} = -\nabla P + \mu\nabla^2\vec{u} + 1/3(\mu\nabla(\nabla.\vec{u})) \tag{1.8}$$

Where ρ is the mass density, μ is the viscosity, P is the pressure and $\vec{u}$ is the displacement velocity of the fluid. The continuity equation for a volume V is,

$$\frac{\partial(\rho V)}{\partial t} + \nabla.(\rho V\vec{u}) = 0 \tag{1.9}$$

This can be combined with electromagnetic theories to explain the formation of nanostructures (like in 3D FDTD approaches). By combining these approaches it was observed that there is an EM field enhancement at surface defects causing local heat confinement triggering Marangoni convection instability and hence the destabilization

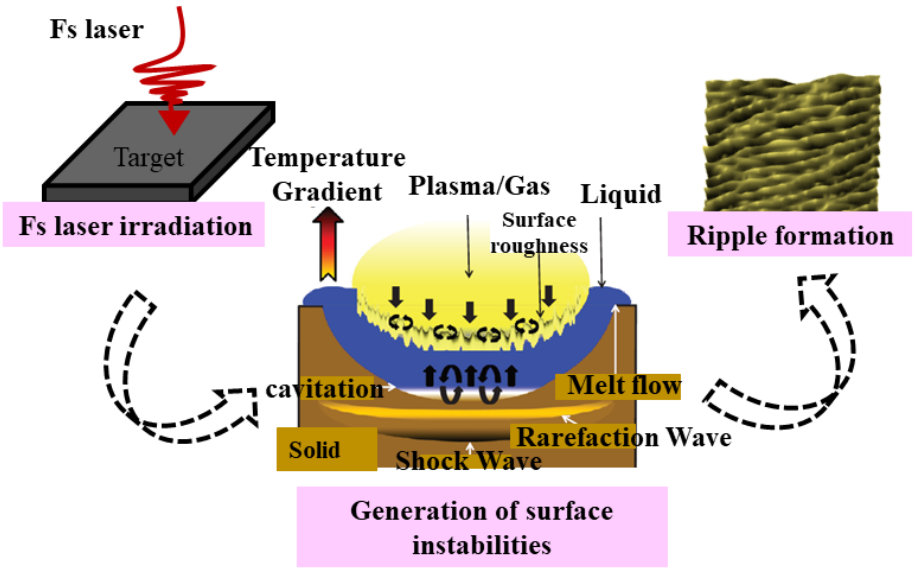

Figure 1.9: Mechanism of hydrodynamic instabilities upon laser irradiation leading to ripples formation (image adapted from [71])

of laser-induced melt layer causing the nanostructure topography. This approach can also reproduce many experimental results [70].

Self-organization theories are based on laser-induced non-equilibrium defects like vacancies, voids, etc., in the subsurface, a few nanometers thick. The destabilization of the crystal lattice in this thin layer, which is far away from thermodynamic equilibrium, causes the formation of nanostructures [85, 65]. The time evolution of the growing surface profile is described by the competition of elementary processes taking place (surface erosion and smoothing) and surface tension gradients. This can be represented as follows which shows the temporal evolution of a growing surface profile h(x,y,t) [86, 87],

$$\frac{\partial(h)}{\partial t} = -v(h)\sqrt{1+(\nabla h)^2} - D\Delta^2 h \tag{1.10}$$

The first term on the right-hand side is for surface erosion and the second term is for thermal self-diffusion. v(h) is the surface curvature-dependent erosion velocity and D is the diffusion that depends on surface diffusivity, activation energy, temperature, and surface density of diffusing atoms.

Different types of surface structures and their possible feedback mechanisms are given in table 1.1.

Oxidation based theories

One of the very notable attempts in recent years to understand the formation of HSFLs is to recognize the role of oxidation associated with it. Öktem et al. [88] proposed a theory based on a feedback mechanism between oxide and nanostructure formation, where an initially positive feedback for nanostructure formation takes place by

Types of LIPSS	Origin of periodicity	Feedback	References
HSFL-ll	Marangoni convection instability	Melt flow	[72], [73], [74], [75], [76]
HSFL-⊥	Marangoni convection instability	Melt flow + possible ablation	[75], [76], [77]
LSFL-⊥	Interference	Ablation	[78], [77], [79], [80]
Grooves-ll (electromagnetic)	Interference	Ablation	[75], [81]
Grooves-ll (hydrodynamic)	Marangoni convection instability	Melt flow	[81], [82]
Hexagonal nanostructures	Marangoni convection instability	Melt flow + Cavitation	[83], [82]
Hexagonal micro-structures (spikes)	Marangoni convection instability	Melt flow + Ablation	[84], [82]

Table 1.1: Different types of LIPSS as a result of femtosecond laser irradiation, their origin of periodicity, and feedback as reported over time, adapted from [71].

oxygen incorporation into the surface followed by a negative feedback as the thickness of this oxide layer increases, slowly breaking the nanostructure growth as shown in figure 1.10. Dostovalov et al. [89] introduced TLIPSS (Thermochemical LIPSS) which are LIPSS formed due to metal oxidation rather than ablation. These TLIPSS have unique characteristics including a rise in relief height, a high degree of order, and an orientation parallel to the polarization direction of the incident beam. The formation of TLIPSS on Ti, Ni, and Cr is explained based on a thermodynamic theory called Wagner theory [90],[6]. The same group later recognized that HSFLs cannot be explained by Sipe's theory [68], and proposed an HSFL formation mechanism based on different modes of propagation associated with SEWs (Scattered Electromagnetic Waves) which evolve with different percentage fractions of oxide [91]. Another recent study by Florian et al. [92] based on FDTD simulations, is the requirement for a 100 nm thick oxide layer for the formation of HSFLs on CrN (figure 1.12). But the existence of sub-100 nm HSFLs with amplitude as small as a few tens of nanometers [63, 51] may appear contradictory to previously mentioned theories.

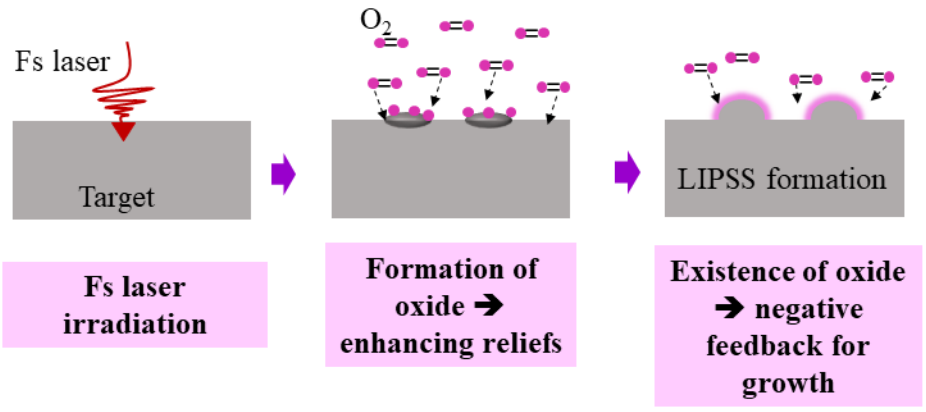

Figure 1.10: (a) Oxidation influencing LIPSS formation (inspired from [88]).

While oxidation as a necessity for the formation of LIPSS is still debated, studies show that oxidation can influence their formation. The generation of anomalous LIPSS or a-LIPSS (oriented parallel to the polarisation with a spatial period in the deep sub-wavelength regime and whose formation mechanism is attributed to scattering of laser light by surface roughness) obtained in ambient conditions and normal LIPSS or n-LIPSS (oriented perpendicular to the polarisation with a spatial period at the sub-wavelength regime and whose formation is attributed to the surface plasmon excitation) obtained in a vacuum environment on Cr/Si films is discussed by Xie et al. [93] (as shown in figure 1.11 (a) & (b)). Here, the formation of anomalous LIPSS (a-LIPSS) is attributed to the transverse electric scattered surface wave (TE-SSW) first excited on the oxide layer and the further interference between the incident wave and TE-SSW giving rise to a-LIPSS with strong oxidation on the intensity maxima. On the other hand, the transverse magnetic hybrid plasmon wave (TM-HPW) in the absence of an oxide layer is given as the reason for the formation of normal LIPSS or n-LIPSS. In other words, a transition from n-LIPSS to a-LIPSS is observed as the air pressure changes and as oxygen becomes more available in the surroundings. This puts forwards a concept where surrounding oxygen will have a significant role in the formation of these nanostructures.

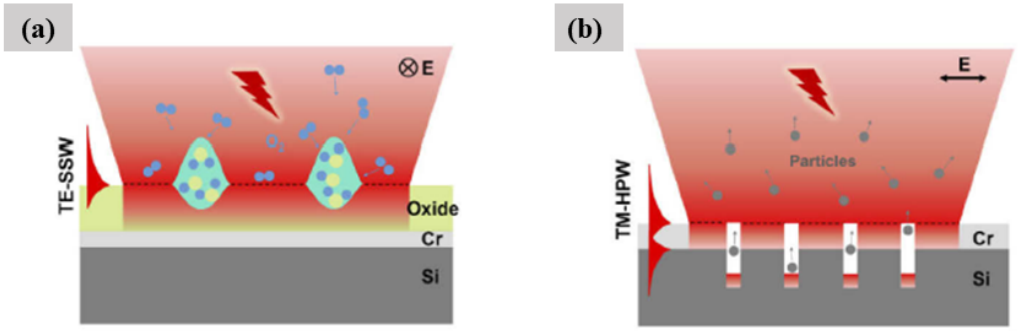

Figure 1.11: (a) formation of anomalous LIPSS (a-LIPSS), oriented parallel to polarization with period at the deep sub-wavelength regime, (b) formation of normal LIPSS (n-LIPSS), oriented perpendicular to the polarization and period at the sub-wavelength regime on Cr/Si films (adapted from [93]).

1.3.3 Numerical models for laser-matter interactions

FDTD simulations

Finite Difference Time Domain (FDTD) simulations introduced by Yee [94], are based on the electromagnetic field analysis surrounding the nanostructures obtained by solving Maxwell's equations. Since it uses an electromagnetic approach it can take into account the laser beam propagation effects, field enhancement, scattering, and propagation in addition to considering the spatio-temporal intensity distribution of the beam. The FDTD model was expanded to include inter-pulse feedback effects, which later was developed by Diezel et al. [76] to explain expansion-like phenomena based on hydrodynamics to account for the laser-generated morphologies on metals. While they are prominently used to discuss semiconductors and dielectrics, this model was applied to metals by Zhang et al. [95]

to detail the LSFL and HSFL formation on the basis of interference of scattered far-field and scattered near-field waves with the incident beam respectively. Rudenko et al. [77] (figure 1.12 (a)) have demonstrated that laser energy deposition and the resultant interference patterns from nanoholes and nanobumps in dielectrics and metals influence the absorbed energy being perpendicular or parallel to the light polarisation and ultimately influence the formation of nanostructures. This study provides qualitative and quantitative analysis of scattered radiative and non-radiative patterns below the material surfaces. In addition, FDTD models have also been used (as mentioned earlier) to confirm the necessity of an oxide layer for the formation of certain nanostructures [92] as shown in figure 1.12 (b).

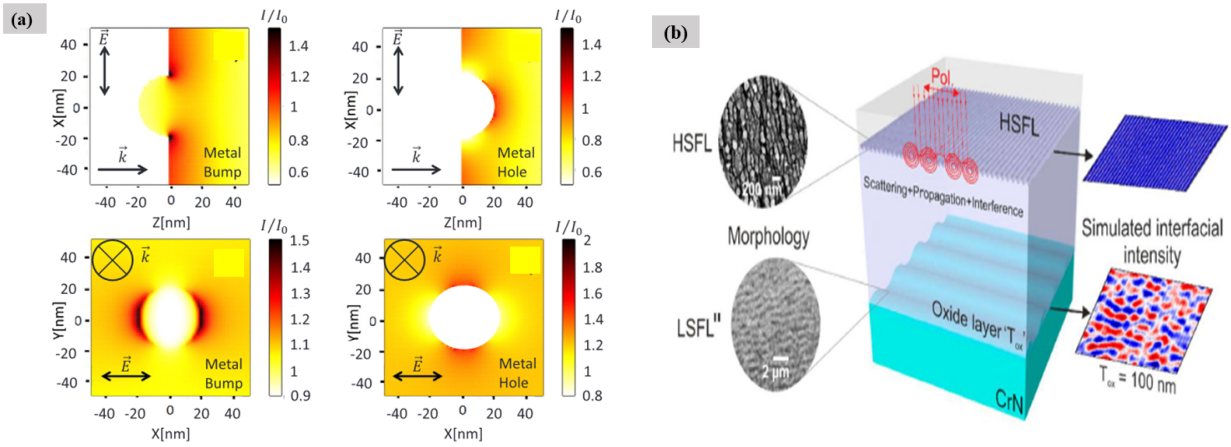

Figure 1.12: (a) FDTD simulations showing the energy deposition below a metal surface with a bump and a hole, adapted from [77], (b) FDTD simulations showing the necessity of 100 nm oxide layer for HSFL formation on CrN, adapted from [92].

PIC simulations

Particle-in-cell (PIC), simulations are based on the collective coupled behavior of electrons and enable the calculation of the trajectories of charged particles in a self-consistent electromagnetic field. Djouder et al.'s work [96, 97] based on this simulation on Cu has indications of LIPSS appearing after a laser pulse with sub-wavelength characteristics as shown in figure 1.13. Further, the evidence of strong near-field enhancement due to surface electromagnetic wave excitations caused solely by laser pulses on the Cu surface upon fs laser irradiations was elaborated by Russel et al. [98] using this model. Wang et al. [99] have also made use of PIC simulations to show that a competition between the surface Coulomb ablation and direct laser ultrafast ablation results in the structuring of the material by a Gaussian pulse. However, the disadvantage of the PIC approach involves noisy results because of simulating a finite number of macro-particles and poor statistical resolution [100].

Two Temperature Model - Molecular Dynamics (TTM-MD) simulations

The two-temperature model: When a laser beam interacts with a metal, the free electrons absorb the heat energy first and then transfer it to the lattice by electron-phonon scattering. For metals, the electrons to lattice energy transfer rate (10^{16} $W/m^3/s$ [101]) and hence the electron-phonon coupling time (few ps) is much slower

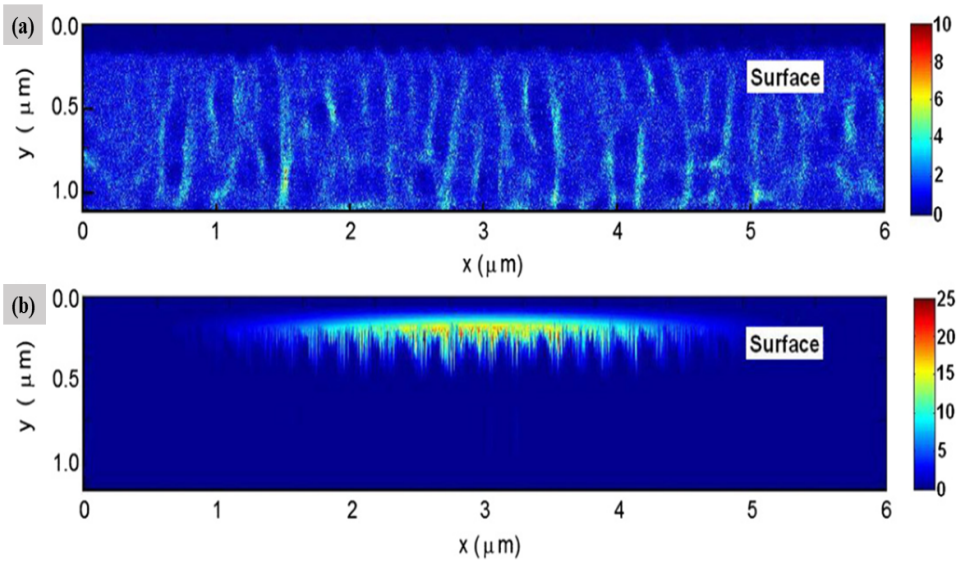

Figure 1.13: PIC simulations giving the electron density profile (a) and the electrical field profile (b) for fs laser irradiated copper. The patterns obtained by PIC simulations are similar to those of ripples, whose periods as seen from the simulations agree with the experimental observations, adapted from [96].

than the material expansion time (several tens of ps). Hence we need to consider the electrons and ions subsystem separately. This electron-phonon coupling is continuous until a thermal equilibrium is established between the hot electron system and cold ion system [102, 103].

The two-temperature model (TTM), proposed by Anisimov et al. [104] gives the energy balance between the electron bath and the lattice by two differential heat diffusion equations governing the temporal evolution of electron and lattice through a coupling parameter related to the electron-phonon scattering rate. Because of the limitations with finding these imbalances experimentally, TTM equations can theoretically predict the heating rates or melting thresholds and are extensively applied for various laser-matter interaction studies [104, 18].

The equations are given by [105, 106],

$$C_e \frac{\partial T_e(t,x,z)}{\partial t} = \nabla.(\kappa - e\nabla T_e) - \gamma_{ei}(T_e - T_i) + S(t,x,z) \tag{1.11}$$

$$C_i \frac{\partial T_i(t,x,z)}{\partial t} = \nabla.(\kappa_i \nabla T_i) - \gamma_{ei}(T_e - T_i) \tag{1.12}$$

where T is the temperature with 'e' and 'i' standing for electrons and lattice respectively. C is the specific heat capacity, κ is the conductivity and γ_{ei} is the coupling factor. S(t,x,z) is the source term representing the absorption of laser energy.

This model was applied to metals such as Ti [107] and Au [106] to include phase transition and heat diffusion effects. This model explains LSFLs having few hundred nm periods. But it has to be further extended to include the sub-wavelength period of HSFLs and laser ablation resulting in a phase transition to vapor. The

limitation in explaining the small periods of HSFLs comes from thermal diffusion effects washing out the small spatial modulation in the absorbed energy [108].

To summarise the basic concept, the interference between the incident beam and surface electromagnetic waves will induce spatially modulated electron density and electron temperatures within a specific period. The electron-phonon coupling and heat diffusion will modulate the lattice temperature exceeding the boiling temperature. Later, the ablation, material transport, and solidification will lead to the final topography [65].

In another model called **Molecular Dynamics (MD) model**, trajectories of interacting atoms in 3-D space and time are evaluated by using Newton's equations of motion [109]. It uses empiric interatomic potentials to account for the potential energies and the forces acting between the atoms. Time-dependent interatomic potentials to calculate the collective motion of atoms are not well suited as they cannot properly explain the thermal or non-thermal melting. Hence, the most commonly used model is the time-independent embedded atom model (EAM) for metals [110].

Analyzing all the above models to study ultrafast laser-matter interactions, the best suited will be the one that will consider heat diffusion in thermal non-equilibrium between the electron-lattice system and also the behavior of atoms in 3-D space and time to properly capture ultrafast laser-matter interactions and morphology changes. Hence, a hybrid model, **TTM-MD** has been proposed.

Ivanov et al. [111] were one of the first to combine TTM and MD to explain laser-induced topography based on material reorganization on an Au target. They identified laser-induced compressive stresses and material relaxation giving rise to tensile waves resulting in subsurface voids. This relaxation gives rise to a hydrodynamic motion of the melted material. At the same time, due to heat conduction into the bulk, high cooling rates resulted in rapid solidification. Another study by Shugaev et al. [112] on Cr targets under air and vacuum irradiation conditions related the surface morphology observed to phase explosion as shown in figure 1.14. These studies show that rather than liquid flow from the molten region of the sample experiencing recoil pressure from ablation, the redistribution of material below the ablated part plays a key role in the final morphology [65].

1.3.4 Applications of LIPSS

Ultrafast laser-induced periodic nanostructures or LIPSS are highly advantageous for various industrial applications, because of their simplicity, cost-effectiveness, and robustness. In this section, topography-based applications for the LIPSS are discussed.

Structural Colors: The colors on material surfaces generated by a material structure are called structural colors. They can be observed in nature when you look at a Morpho butterfly, where the wings exhibit bright colors due to the light interference and diffraction on periodic structures naturally present on its wings. LIPSS on metallic surfaces are also seen to exhibit a similar type of behavior. In fact, these kinds of structured surfaces

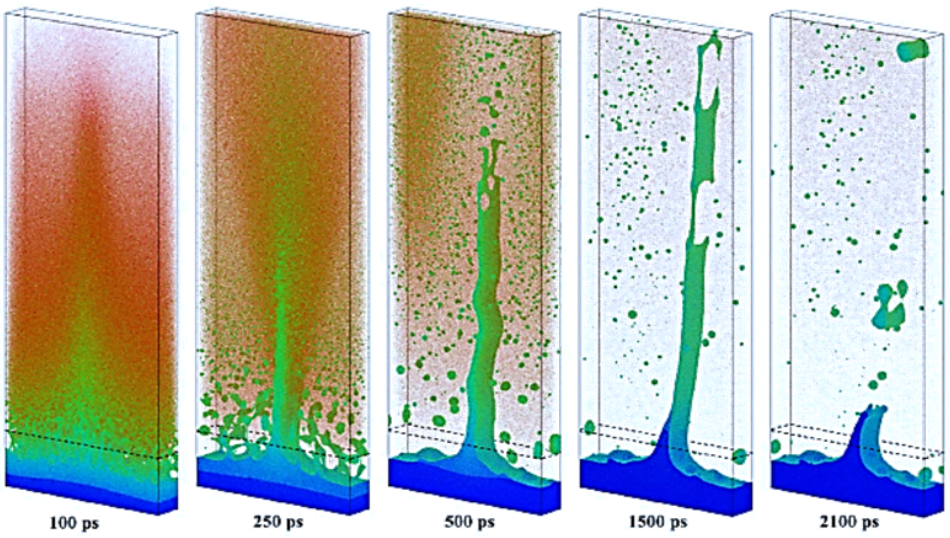

Figure 1.14: Temporal evolution of atomic snapshots obtained by TTM-MD of a Cr target irradiated by fs laser demonstrating the formation of a liquid wall in the ablation process followed by rupture of the wall and generation of a solidified protrusion. Dark blue corresponds to the solid phase, light blue and green to the liquid phase, and the red atoms to the vapor phase, as adapted from [112].

.

change their colors with different viewing angles because of diffraction. An example of this is shown in the figure 1.15 (a), where LIPSS on the surface of platinum shows iridescent colors [31]. On a much larger scale, Dusser et al. [26] have shown that it is also possible to achieve color pictures by producing LIPSS on metallic surfaces with different orientations.

Tribological applications: LIPSS are widely known to exhibit efficient tribological performance. Bonse et al. [113], [61], Wang et al. [114], and Voyer et al. [115] have reported a reduction in the friction and wear of LIPSS-incorporated metallic surfaces. The most recent studies were made by Bonse et al. on Ti and steel surfaces. It was seen that compared to a polished surface the wear on LIPSS-generated surfaces is negligible. This is as shown in the figure 1.15 (b), where you can see wear tracks on Ti surfaces [116].

Biomedical applications: Biomedical engineering of surfaces based on femtosecond laser irradiation is becoming a popular advanced technology. LIPSS have a significant influence on the cell growth. Kai Borcherding et al. [117] have seen that for laser-textured Ti surfaces the cell adhesion (osteoblast-like cells) is greatly improved compared to non-textured surfaces. Raimbault et al. [118] have studied the influence of initial cell response for femtosecond laser generated structures on Ti surfaces and found that stem cells are more sensitive to nano-scale structures than micro-scale structures, unless the size of the cells are comparable with those of the micro scale structures. In addition, for LIPSS-generated Ti surfaces cell area and adhesion area were also seen to be enhanced for human stem cells [119] as can be seen from figure 1.15 (c). It was also observed that for Fe-Mn alloy surfaces with LIPSS bio-degradation rate can be significantly improved [120].

Femtosecond laser-induced ripples have also found other applications such as enhancement in thermal emis-

sion [121, 122], surface-enhanced Raman spectroscopy (SERS) [123, 124], heat transfer performances [125], applications with improved thermoelectric properties [126] etc. While industrial applications mostly use laser-

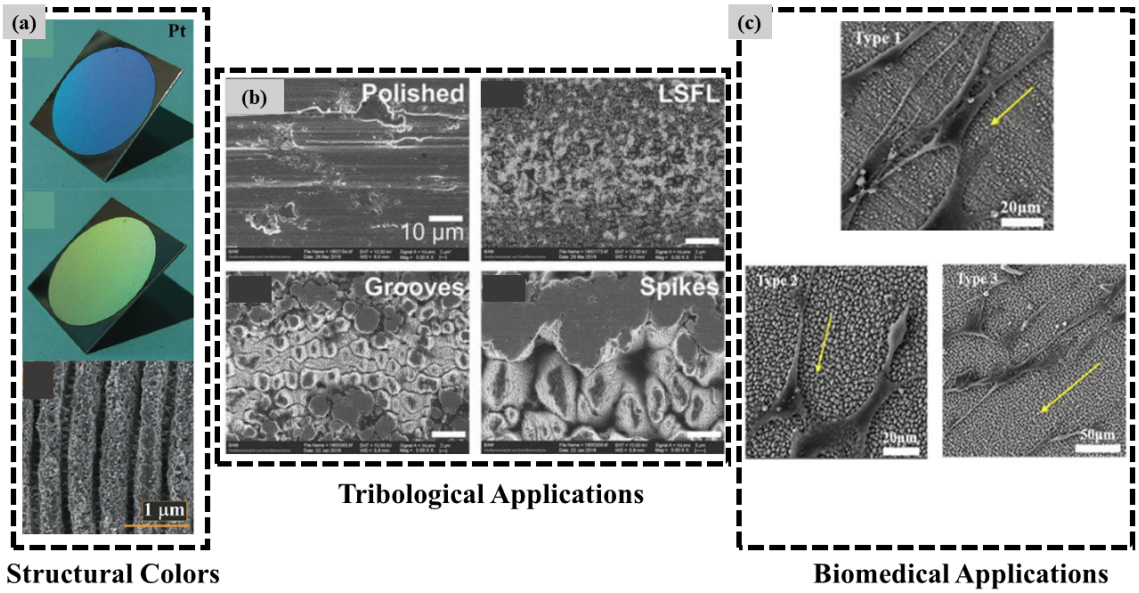

Figure 1.15: (a) structural colors on Pt surfaces covered with LIPSS, (as adapted from [127]) (b) The SEM images after the tribological tests done on Ti surfaces covered with grooves, LSFLs and spikes along with a polished, non-irradaited surface, (as adapted from [116]) (c) SEM images of cell adhesion on Ti covered with LIPSS (type 1), grooves and ripples (type 2) and columns with overlapping LIPSS (type 3), (as adapted from [119]).

based morphologies created on a variety of materials, some applications require control over surface chemistry which will be explored in the following section.

1.4 Surface chemistry due to laser-matter interactions

1.4.1 Laser induced surface chemistry

Laser-induced surface chemistry points to the chemical changes occurring on a material surface during or due to laser irradiation. While lasers in gas-surface studies are known to provide fundamental insight into the mechanism and dynamics involved in chemical interactions, they also help in achieving various practical applications.

The laser-induced chemical change can occur during or after the laser pulse. When dealing with laser-induced surface chemistry one should think about the thermal and non-thermal aspects of surface chemical alterations caused by the laser. Non-thermal laser-induced surface chemistry is mainly the result of electronic or vibrational excitations of the gas and the direct laser excitation of the solid [128, 129]. For example, SF_6 is usually inert towards Silicon but can be made to react with Si by bringing SF_6 to a laser-induced excited state [130]. Even in the case of laser-induced oxidation by UV photons, non-thermal effects are responsible for enhanced oxidation in semiconductors like Si, or GaAs [131, 132]. Most of these studies focus on continuous wave lasers or UV lasers, with limited available information on ultrashort laser pulse systems. In addition, all these cases saw a laser enhanced chemical reaction like enhanced oxidation for semiconductors [131, 132] or SF_6 becoming more

reactive towards Si, that could not be solely explained by the classical thermodynamic approaches.

Laser radiation can trigger chemical reactions between a gas and a solid target, ultimately resulting in a new chemical product at the surface. Laser-induced nitrides on metals are one such case that arises due to the reaction between the metal and the nitrogen from the atmosphere. For example, a surface compound Ta_3N_5 along with Ta oxides is formed on Ta irradiated with ns laser, in a mix of oxygen and nitrogen atmosphere as characterized with XPS [133]. It is concluded that the composition of the gas phase, the ratio between oxygen and nitrogen, and the laser irradiance are the key factors influencing the surface chemistry in this case. Similar surface nitration of Ti, Zr, and Hf has also been achieved with pulsed lasers [134]. For Ti, TiN is formed under both fs and ns laser pulses [135, 136]. A recent study [137] focuses on the influence of different processing and further exposure environments on femtosecond laser-generated LIPSS on Cu surfaces to explore the variation in the levels of carbon contamination after laser texturing. This study indicates that femtosecond laser-texturing makes surfaces more sensitive to carbon contamination from the atmosphere, and is highly dependent on the exposure surroundings.

However, the common surface chemical modification associated with laser irradiation on metals is the formation of oxides since most laser machining takes place in ambient conditions [20, 21, 22]. In all cases, irradiation with lasers, whether it be CW, pulsed, or ultrafast, the metal surfaces are always accompanied by oxidation. The thickness of these oxide layers increases with accumulated fluence [138]. For fs laser irradiated Al, it is seen that at low laser fluences hydroxides dominate over oxides and as the fluence increases, more oxides are accumulated [139]. In another study involving Ta and Al, laser irradiation in a vacuum and inert gas atmosphere (respectively) does not eliminate surface oxidation [133, 140]. This could be due to contamination from the atmosphere accumulated after laser irradiation or could be due to contamination inside the chamber. In the case of Ti, under inert gas conditions (Ar gas), TiO_2 formed in ambient conditions restructures to form TiO and TiO_3 [135].

LIPSS on metals are also seen to be associated with oxides. For example, LSFLs, grooves, and spikes produced on Ti alloy by femtosecond laser irradiation show a few hundred nm of oxide layer as indicated by glow discharge optical emission spectroscopy (GD-OES) [116]. This is in accordance with another study on Ti that reported a 200 nm thick oxide layer for LSFLs and around 150 nm for HSFLs as confirmed by micro Raman, AES (Auger Electron Spectroscopy), and XPS (X-ray Photon Spectroscopy) analyses [141]. HSFLs with relief heights as small as a few tens of nanometers have also been reported. As small as 20 nm for HSFLs on Ni [51] and 50 nm for ps-induced HSFLs on Ti [63], meaning they could be generated with a smaller thickness of oxide layer depending on the material and laser parameters.

Surface oxidation therefore appears to be an inevitable surface chemical modification accompanying laser processing in ambient conditions and it is important to understand the mechanism of oxidation associated with laser processing to utilize it to maximum potential. And while there has been no significant work done to understand the oxidation mechanism and the surface chemical alterations taking place during ultrafast laser irradiation, a significant amount of work exist on the aging of laser-irradiated surfaces as follows.

1.4.2 Aging of laser irradiated surfaces

Surface chemistry in laser-matter interactions is not a new topic but is studied to some extent. A major part of these studies deals with the aging associated with wettability of laser-irradiated surfaces. That is, these studies analyze how surface chemistry and hence the water contact angle evolves over time after laser irradiation. Two main approaches are usually encountered as shown in figure 1.16:

(i), wettability and aging is a result of surface carbon contamination,

(ii), wettability and aging is related to oxides.

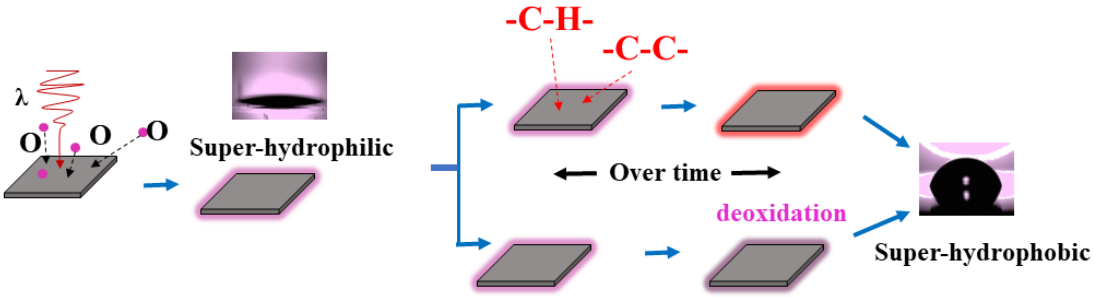

Figure 1.16: surface chemical alterations with aging explaining wettability transition

Regarding the first point on carbon contamination, Kietzig et al. [142] were one of the first in 2009 to explain the wettability evolution on the basis of surface chemistry after laser irradiation. It was shown that metallic alloys under femtosecond laser irradiations become super-hydrophobic over time with laser-generated dual-scale roughness. The explanation was grounded on the decomposition of carbon dioxide into carbon at the iron oxide sites. Similarly, for micro-pillars and micro-cavities produced on Al by ps laser stored in an organic-rich environment [143], a transition from super hydrophilicity to superhydrophobicity was observed contrary to samples stored in carbon dioxide, oxygen, and nitrogen which remained super-hydrophilic. This was a clear indication that the transition to superhydrophobicity is highly influenced by the organic compounds in the surrounding environment. The C/Al ratio obtained from XPS spectra is used as an indicator for the amount of adsorbed organic compounds under various conditions. Recent studies in Al irradiated by ns laser show identical behavior, where the XPS spectra on laser-generated protrusions reveal that the increase in C-C/C-H bonds increases the non-polarity of the surfaces and contributes to the hydrophobicity [144]. This transition is also seen for fs laser irradiated copper surfaces, with micro-pits and micro protrusions [145] and is attributed to carbon contamination.

Another study looked at fs laser generated 1D and 2D periodic structures on stainless steel and observed C-C, C-H, C-O, and C=O, constituting adventitious carbon from C 1s XPS spectra. They observed that the surfaces became richer in hydrocarbons over time. Hence, the evolution of contact angle is backed by the variation of adventitious carbon content [146]. Further, we can see investigations done on microgrooves produced in brass

by a ns laser and kept in different liquid storage conditions (vinegar, IPA Sodium bicarbonate, saltwater compared to air). The samples stored in IPA attained hydrophobicity faster than in the other conditions, confirming that the presence of the organic compounds dramatically influences the wettability transitions [147].

The role of carbon contamination in the wettability transition is also discussed for various femtosecond laser-textured metals like Cu, Co, Fe, Al [148]. Here they conclude that laser-induced surface reaction must be responsible for the evolution of contact angle over time and is independent of the type of metal [148], which is what we can also say from the above literature analysis. Most of these papers draw similar conclusions where the surface goes from super hydrophilic to super-hydrophobic over time due to non-polar organic contamination or adventitious carbon (airborne molecular contaminations) compound from the atmosphere as shown in figure 1.16. In fact, the presence of even a monolayer of hydrocarbon contamination is widely accepted as the reason for this behavior of the laser-irradiated surfaces [149].

The other factor influencing wettability is related to oxides. Laser-processed surfaces are initially super hydrophilic due to laser-generated oxides, which are polar in nature [144, 150]. In fact, there have been some attempts to explain the wettability transition over time based on the type of oxides on Cu surfaces [151] and Ti surfaces [152]. In picosecond laser-textured copper surfaces it was observed that partial deoxidation of laser-generated CuO to form Cu_2O over time is the reason for the transition to hydrophobicity [151]. And for femtosecond laser-irradiated Ti surfaces the transition from Ti_2O_3 to TiO_2 over time is regarded as the major contributor to hydrophobicity with aging [152]. These significant results are shown in table 1.2.

Material	Laser	Types of structures	Surface chemistry on aging	Reference
Steel	Femtosecond laser	dual scale roughness, 1-D & 2-D periodic structures	Carbon contamination	[142],[146]
Ti	Femtosecond laser	LSFLs	Oxide transformation	[152]
Cu	Femtosecond laser	mix of micro pits, micro-grooves & nano structures	Carbon contamination	[145]
Cu	Picosecond laser	mix of ripples, micro & nanostructures	Oxide transformation	[151]
Al	Picosecond laser	micro pillars & micro cavities	Carbon contamination	[143]
Al	Nanosecond laser	micro protrusions	Carbon contamination	[144]
Brass	Nanosecond laser	micro & nano dual scale structures	Carbon contamination	[147]

Table 1.2: Tabular representation of review on wettability transition of various materials

These results show that the literature on aging of laser-irradiated surfaces is mature in the scientific community. The data collected from XPS spectra together with water contact angle studies are accepted as good indicators of the surface chemistry alterations upon femtosecond laser irradiation. Not only wettability but also other surface properties are dependent on laser-induced surface chemistry alteration as will be seen in the following section.

1.4.3 Influence of ultrafast laser-assisted oxidation on surface properties

Kruse et al. [3, 4] have studied the heat transfer performance of laser-machined surfaces, made of mounds and LIPSS on Cu and stainless steel. It was observed that the heat transfer coefficients are highly dependent on the thickness and type of nanoparticles containing layer generated by the laser, which are oxides that usually act as insulating layers due to their low thermal conductivity. Ultimately the heat transfer performance depends on the change in surface area, capillary wicking, effective thermal conductivity, escaping vapor efficiency, and potential nucleation sites in this oxide layer.

The tribological performance of LIPSS is also strongly dependent on this laser-generated oxide layer. For example in Ti, HSFLs - which have a modulation depth 5 times smaller than LSFLs - do not endure the RSTT (Reciprocal Sliding Tribological Tests), and the first layers removed by this wear test are oxide layers. Whereas for LSFLs the coefficient of friction was reduced by a factor of 2-3 with a strong reduction in wear. This is attributed to the oxide layer on HSFLs not being sufficient enough for the lubricants to deploy their beneficial tribological activity [1, 2].

Metal color marking is also an important property that depends on the oxide layer. Antonczak et al. [5] produced different colors on Ti surfaces which were dependent on the oxide layer thickness. In an interesting study by Jwad et al. [153] on Ti, it is shown that such laser-induced oxide-dependant colors can be erased from the surfaces using laser-induced oxygen reduction to eject the oxygen. Similar results can also be seen for LIPSS obtained on Cu by Graham et al. [154] where the complex colors obtained on the laser-fabricated surfaces are attributed to the thickness of copper oxide. They observe that this copper oxide can retain the color generated by laser irradiation over a long period of time since it (laser-generated copper oxide) is stable at room temperature and low humidity.

Hence, it can be concluded from the last few sections (mainly section 1.3.4 and section 1.4.3) that by carefully tuning the surface chemistry together with the surface topography, plausible enhancement in the efficiency of laser-based applications can be achieved. This is however possible only by carefully understanding the chemical modifications accompanying the laser irradiation on various materials.

1.4.4 Mechanism of oxidation

Classical theories of oxidation and laser-assisted oxidation

Conventionally, oxidation on metals is associated with theories such as the Cabrera-Mott theory or Wagner theory. Some groups have tried to associate these classical theories with laser-assisted oxidation. For example, for a metal like nickel, Nanai et al. [155] have shown that Cabrera-Mott is valid for oxide layer thickness ranging from 0 to 10 nm and that the Wagner theory is relevant for 100 nm to 1000 nm thick oxide layers.

Cabrera-Mott theory is usually applied at lower temperatures for metallic surfaces and for thin oxide

films, where initially the oxidation rate is very rapid but slows down after some time. It is based on the hypothesis that the electric field due to the Cabrera-Mott potential developed between the positively charged metal ions and negatively charged oxygen ions leads to the formation of oxides. Oxide growth follows a logarithmic pattern, given by [156],

$$1/X = A - Blnt, \tag{1.13}$$

Where, X is the thickness of the oxide at time t, and A and B are constants.

Xia et al. [157] have shown that for Ti surfaces, under ms pulsed laser irradiations, Cabrera-Mott theory of oxidation seems to be a match, a conclusion based on simulations where their experimental oxide layer thickness for different laser powers was in accordance with the simulation results based on Cabrera Mott theory as shown in the figure 1.17.

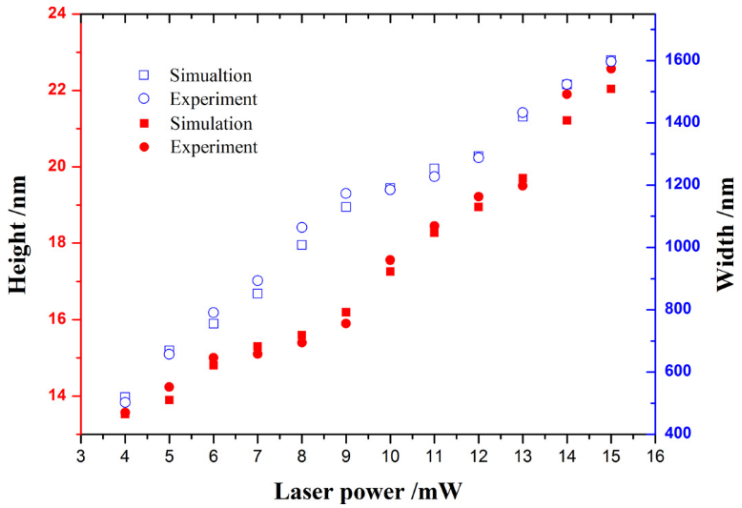

Figure 1.17: The simulation based on Cabrera–Mott theory and experimental results of the width and height of ms laser-induced oxidation on titanium. The graph shows the widths (hollow blue) and heights (solid red)of lines written by laser-induced oxidation for simulation results (square) and experiment results (circle). Adapted from [157].

.

The **Wagner's theory** is usually applied to explain the growth of thick oxide layers. It is based on ion migration due to a chemical potential gradient across the oxide layer. The oxidation rate follows a parabolic equation in this case, given by [158],

$$X = K_p t^{-1/2} \tag{1.14}$$

Where X is the oxide layer thickness at time t and K_p is the parabolic oxidation rate constant.

While Lian et al [159] have shown that the surface oxidation kinetics of polycrystalline Cr films irradiated by a Nd:YAG laser depends on the grain size. For example, they show that the Cabrera-Mott law is more apt for grain sizes smaller than 100 nm while Wagner's theory is applicable for grain sizes larger than 100 nm.

They explain this based on defect formation due to laser irradiation together with the laser-induced desorption of initially chemisorbed oxide layers [159] which could be different for different grains. But, Dostovlev et al. [160] have used an approach based on the parabolic oxidation rate to explain the oxide layer formed on LSFLs due to fs laser irradiation on chromium, where they extrapolate the parabolic oxidation constant of Cr to the high-temperature regime induced by the laser to explain several hundreds of nanometers of oxide layer thickness seen on LSFLs.

It is not yet clear whether Cabrera-Mott's or Wagner's theory is more suitable to explain laser-induced oxidation, both are based on the diffusion of ionic species in order to form an oxide layer. Hence it is important to analyse whether or not such ionic diffusion can happen within the short time scales associated with ultrafast laser irradiation. Following is the literature evidence that discussed diffusion-based oxidation mechanisms for CW and pulsed lasers.

Ursu et al [161] have proposed a **diffusion model** for CW laser-assisted oxidation on Cu surfaces. They calculate the diffusion coefficient based on parabolic oxidation resulting in copper oxide and theoretically predict the possible oxide thickness achieved for particular laser parameters. The good agreement between these predictions and the experimentally observed oxide layer thickness suggests a diffusion-based mechanism leading to the formation of copper oxide upon CW laser irradiation of Cu. Similarly, Zeng et al [162] have shown that for Ti samples under CW laser irradiation oxygen and nitrogen diffuse into the metal, and Ni is found to be under the oxygen-enriched layer as shown in figure 1.18. The diffusion coefficients of oxygen and nitrogen calculated from the classical diffusion equations are used to explain the larger diffusion length of nitrogen compared to that of oxygen. For ns laser irradiated steel samples [163], using different kinds of lasers (Nd:YAG, KrF, and XeCl lasers), it was found that the iron oxides accumulate at the top and the nitrides at the bottom after laser irradiation. But here, the thermodynamics calculations are not in agreement with the time needed for nitrogen diffusion in the case of Nd:YAG laser irradiation. The enhanced diffusion rate of nitrogen is attributed to the higher temperatures established by the laser-generated plasma and to the higher pulse repetition rate.

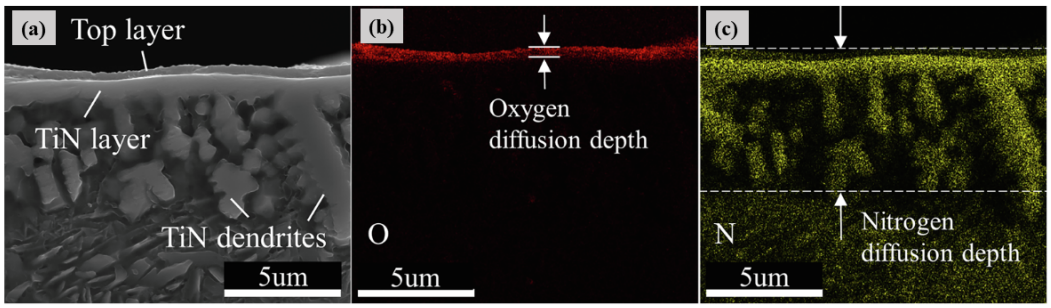

Figure 1.18: (a) cross-sectional area of laser irradiated Ti where the EDS was done, (b) elemental distribution of O as given by EDS & (c) elemental distribution of N as given by EDS, adapted from [162].

In the case of femtosecond laser pulses, the application of these classical theories is more complicated because of the very short pulse duration. Femtosecond laser irradiation involves the deposition of a large amount

of energy over a small region and involves variable temperature profiles over a very short period of time. One would therefore expect a different oxidation mechanism compared to a furnace-treated sample, and could result in different structures, compositions, and even oxidation kinetics [164]. Temperature variation could be faster than the chemical reactions taking place. This might lead one to think of the difficulties in combining existing kinetics theory with femtosecond pulsed laser irradiation. However, experimental evidence supports oxygen ion migration as a reason for fs laser-assisted oxidation. Kotsedi et al's work on chromium [165] using depth profiling combined with Rutherford back scattering spectrometry (figure 1.19) concludes that "... Cr_2O_3 formation in thin films using nanosecond and femtosecond lasers follows similar oxygen diffusion as for Cr_2O_3 chemically." This hints that Cr_2O_3 formation in thin films using nanosecond and femtosecond lasers could be similar to the classical oxidation mechanism based on diffusion resulting in Cr_2O_3.

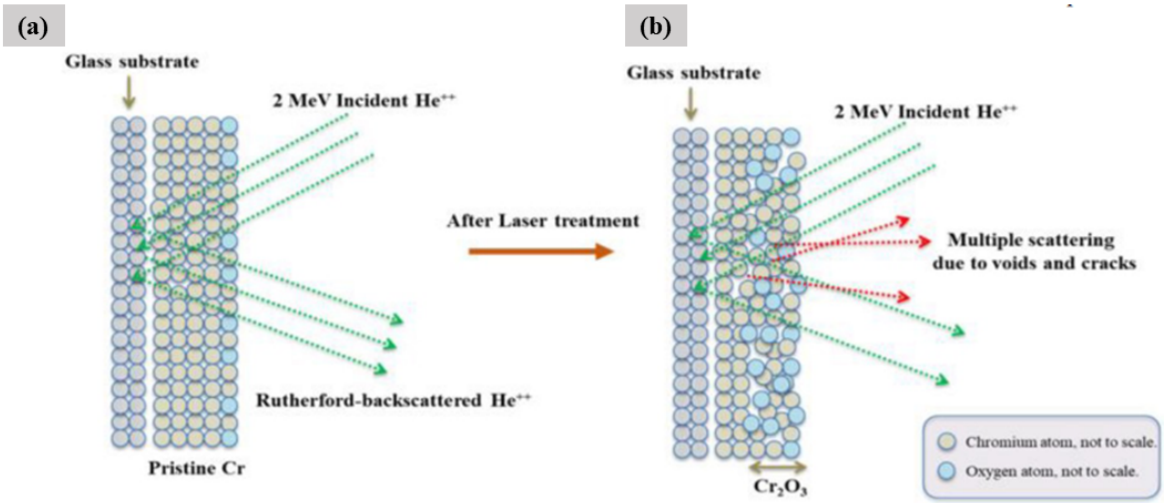

Figure 1.19: (a) and (b) represent the schematic diagram of Rutherford back-scattering spectrometry and the multiple scattering obtained from the laser irradiated sample, where the depth profiling indicated the oxygen diffusion into the sample, as adapted from [165].

A clear picture of the chemical modifications accompanying laser irradiation along with specific topographies is still lacking. This might be due to the difficulty in generalizing such a process since it depends upon a combination of various factors including laser processing environment, laser parameters, material properties, etc. Moreover, the answer to the question of whether the resulting chemistry at the surface is due to the interaction of surrounding gases with the metal during laser irradiation or due to aging is still not clear.

1.5 Motivations for this work

1.5.1 Why Surface Chemistry?

Ultrafast laser-induced nanostructures are of great interest, with new studies emerging frequently because of their vast potential for industrial applications. The topography-based studies of laser-induced periodic structures are widely available - (their types, origin, applications, formation on metals, alloys, polymers, and dielectrics, depen-

dence on laser parameters, etc.) but, the ultrafast laser-induced surface chemistry is seldom accounted for. While the understanding of laser-induced topography is the first step in realizing various applications, surface chemistry alterations accompanied by laser irradiation plays an as significant role. The goal of this thesis is to understand surface chemistry modifications accompanied by ultrafast lasers. The most common chemical changes is surface oxidation when the irradiation is carried out in ambient conditions [166, 167, 141, 168]. It should be noted that not only is the formation of nanostructures influenced by oxidation, but so is also the final physicochemical response of a laser-irradiated surface [4, 1, 153]. The laser-generated oxides can also have a significant impact on the final response of the surfaces and it is important to distinguish them from oxides accumulated during aging under ambient exposure.

1.5.2 How to study laser-induced oxidation?

From the literature review, we can formulate two major points to address regarding the femtosecond laser-assisted surface chemical alteration:

- **The role of oxidation in the formation of fs laser-induced nanostructures**
- **How to control femtosecond laser assisted oxidation?**

One of the most timely aspect to address regarding ultrafast laser-induced oxidation is its role in the formation of nanostructures, specifically the question is - Is oxidation necessary for the formation of nanostructures? Just like electrodynamics and hydrodynamics based explanations for LIPSS, the oxidation-based formation of LIPSS is a topic lacking consensus in the literature. Hence it is important to address whether oxidation is an unavoidable significant factor influencing nanostructure formation.

Another research direction is the extend to which oxidation resulting from femtosecond laser irradiation can be controlled. This can be accomplished by **understanding the oxidation mechanism during the ultrafast laser processing**. This will also help us to answer a **key question: does laser-assisted oxidation happen during or after the end of a fs-laser pulse, i.e. is oxidation taking place within the timescale associated with ultrafast laser irradiation.**

As a first step in addressing the physicochemical response based on surface chemistry, wettability studies of the surfaces are a good choice since the technique is already widely established. In addition to wettability studies, other characterization techniques will be used including SEM (scanning electron microscopy), AFM (atomic force microscopy) and TEM (transmission electron microscopy) for topography analyses, and XPS (x-ray photon spectroscopy), STEM-EELS (scanning-TEM electron energy loss spectroscopy) and STEM-EDX (scanning-TEM energy dispersive electron spectroscopy) for extracting surface chemistry.

In order to achieve these goals, we have to distinguish between laser-generated oxides and oxides accumulated over time. This can be established by performing the irradiation in ambient air, under high vacuum conditions, and under various gaseous environments - i.e. in the presence of a reactive gas like nitrogen and, a

non-reactive gas like argon. To decouple chemical from morphological effects, a set of laser parameters will be chosen to obtain the same nanostructure under all environmental conditions. This will make it easier to compare the surface chemistry solely based on the surrounding environment in which the laser irradiation is carried out.

Numerical simulations (TTM-MD) giving the spatial and temporal evolution of the thermodynamics of femtosecond laser irradiated samples will support the experimental investigations and explanation.

1.5.3 What nanostructures to study?

As discussed in previous sections, a wide variety of nanostructures is achievable with femtosecond lasers. They can be LSFLs, HSFLs, spikes, grooves, etc. Laser-induced oxidation is usually associated with each of these nanostructures. The nanostructure of choice has to be one that remains unchanged for a set of laser parameters (laser fluence and number of pulses) regardless of the environmental conditions in which the experiments are performed. Moreover, a nanostructure that can be generated at smaller fluences and a lower number of pulses is preferable since this will avoid ablation of the material surface and significant redeposition of debris which can have their own chemistry. HSFLs or high-frequency ripples fit this criteria. As will be discussed in the coming chapters, HSFLs can be generated using a constant set of laser fluence and number of pulses for all the environments in which the irradiation is performed. Generation of HSFLs will ensure negligible ablation or no ablation and hence no redeposition or plasma formation [169, 170]. HSFLs are selected because their formation does not involve significant material removal (mainly melting), allowing for a precise understanding of how irradiated surfaces become oxidized during laser processing.

1.5.4 Which material to study?

When dealing with surface oxidation, the kinetics are highly influenced by the material on which the irradiation is performed. In this thesis, metals and more specifically tungsten (W) is chosen due to the wide variety of applications of its oxides such as in catalysis [171, 172] and wettability.

Another important reason for choosing W is its high melting point at around 3673 K [173]. The classical oxidation kinetics of W gives rise to the most common tungsten oxide WO_3, a process that takes place at 600 K to 1273 K, below the melting point of W [174, 175, 176]. This means that W is in the solid state during this time and hence the complexity of phase transitions during oxidation can be avoided. The vast literature on oxidation mechanism of tungsten is another reason for choosing this material. In addition to this, tungsten forms oxides of various stochiometry and crystal structures depending on the pressure and temperature combinations [176]. This aspect introduces new interesting possibilities of extracting different oxides by controlling laser fluence, cooling rates and other laser parameters.

Tungsten

Tungsten (W) belongs to group 6 of the periodic table with atomic number 74. It is one of the metals with a very high melting point, around 3673 K, high tensile strength, and low coefficient of thermal expansion [173]. It has various applications such as filaments, microchip technology, liquid crystal displays, etc.

The most common oxide of tungsten is WO_3. In addition, it has many sub-stoichiometric phases where the x changes from 2.625 to 2.92 in WO_x, and are called the Magneli phases. They are $W_{18}O_{49}$,W_3O_8,$W_{32}O_{84}$ $W_{17}O_{47}$,W_5O_{14}, $W_{20}O_{58}$, $W_{25}O_{73}$ [177].

Oxidation Kinetics of W

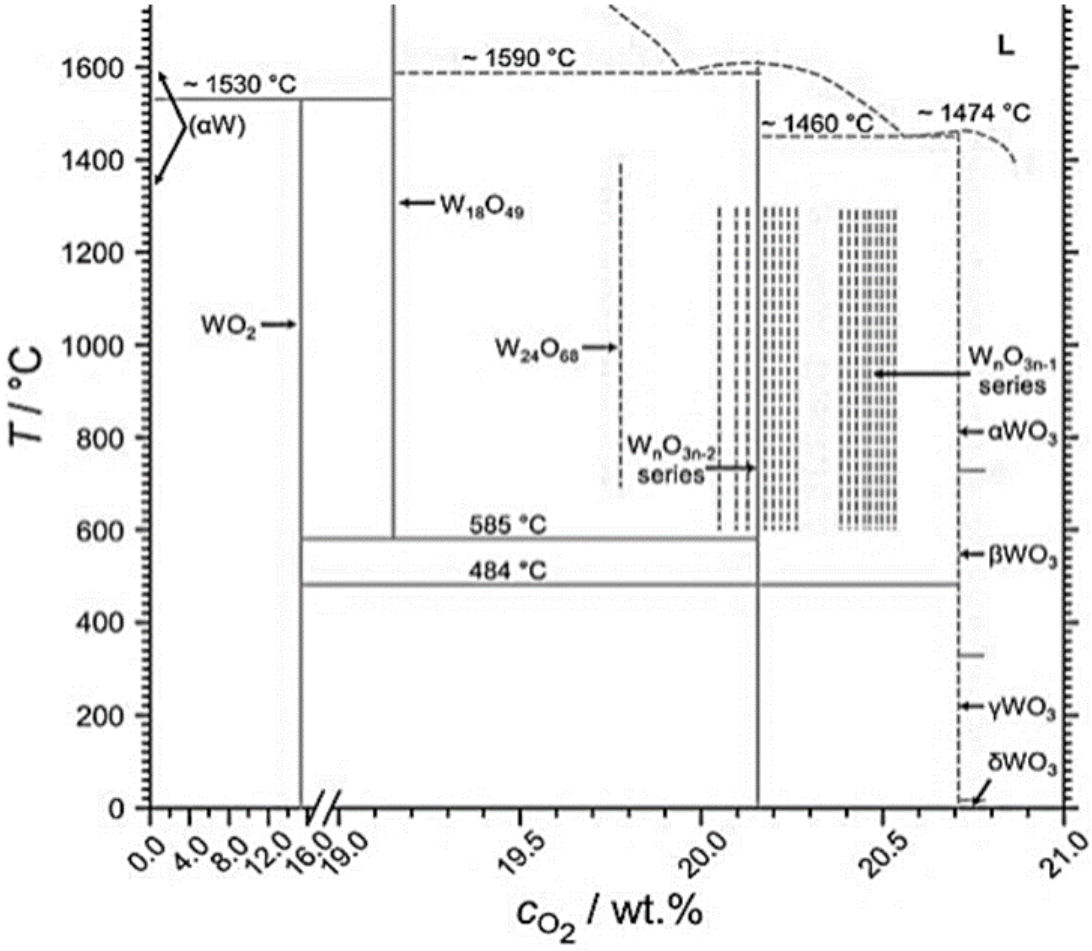

Figure 1.20: Phase diagram of tungsten oxygen system where α, β, γ, and δ represents tetragonal, orthorhombic, monoclinic and triclinic crystal structures, adapted from [176]

Like many other metals, at room temperature W reacts with atmospheric oxygen to form a native oxide scale at its surface. Metals usually follow an inverse logarithmic law for the native oxide formation [156, 178]. As temperature increases ($\sim 873K$), the kinetics follow a parabolic behavior [179]. Further, an increase in

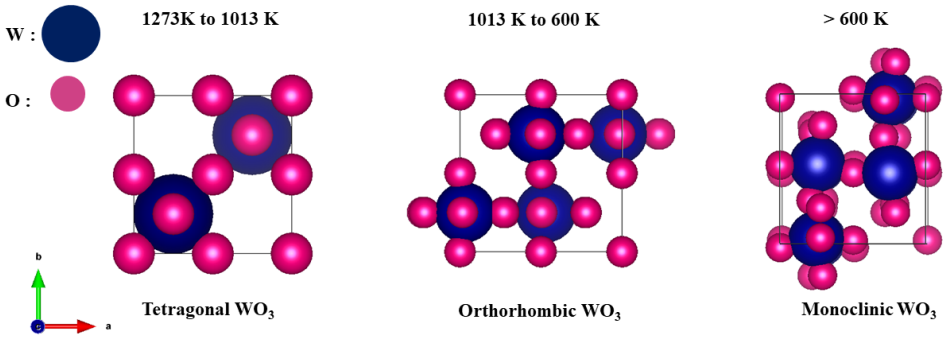

Figure 1.21: Polymorphism exhibited by WO_3, idea inspired from [174]

temperature ($873K - 1023K$) results in a porous oxide layer formed by linear oxidation kinetics [179].

On the other hand, WO_3 exhibits polymorphism during heating and cooling [174, 175, 176]. Up to 600 K monoclinic WO_3 exists (γ-WO_3). Between 600 K and 1013 K, it transforms to orthorhombic WO_3 (β-WO_3). This is shown in figure 1.20 and in figure 1.21. Above 1013 K, tetragonal WO_3 (α-WO_3) is stable. Upon cooling, the reverse order follows and these phases are converted back to γ-WO_3 [176]. As can be seen from figure 1.20 as the partial pressure of oxygen increases the stoichiometry changes from WO_2 to W_nO_{3n-2} to W_nO_{3n-1} to WO_3.

The adsorption mechanics of oxygen on the surface of tungsten are as follows (figure 1.22). If we assume three layers of oxygen adsorbed on the topmost layer of tungsten, the first layer of oxygen in contact with W will be strongly chemisorbed since it forms bonds directly with the tungsten surface. The second layer of oxygen on the top of this first layer will be under weak chemisorption and the third layer will be weakly physisorbed since it has no direct contact with tungsten [180]. The chemisorbed layer of oxygen does not get desorbed since it shares electrons with tungsten. The diffusion of oxygen ions into the bulk of tungsten is driven by the electric field due to the chemical potential developed between the metal and oxygen ions. This diffusion, determined by the diffusion coefficient (D) is limited by the coverage of oxygen on the top of the tungsten and the temperature. Initially, the first layer of oxygen then diffuses into the W surface. This causes the second layer to be under strong chemisorption and in contact with the W surface, the third layer is now the new second layer and is weakly chemisorbed. At this point, a new layer can replace the previous third layer and will be weakly physisorbed [180]. This will happen continuously as long as the oxygen layers diffuse into W and new layers of oxygen form on top

Figure 1.22: Adsorption mechanics

of it.

Pressure dependence of oxidation

The oxidation rate of tungsten is dependent on the surrounding pressure P. As the pressure decreases the rate constants also decrease. The pressure P dependence of the reaction rate is [180] [181],

$$\frac{dn}{dt} = KP^{1.1} \tag{1.15}$$

Where $\frac{dn}{dt}$ is the rate of oxidation and K is a constant. In the study by Gulbransen et al. [181] it was observed that at temperatures where tungsten oxide is volatile, the pressure had a major influence in the formation of the oxide, and low oxygen pressure usually favored the volatilization of oxide for a given temperature.

However, ultrafast laser irradiation generates very high-pressure gradients in the range of GPa and hence it is necessary to understand the behavior of tungsten oxides at these pressures as given below.

Stability of tungsten oxides at laser generated pressure gradients

Laser irradiation generates very large pressures in the range of GPa. The most common oxide of W, WO_3, is stable under these pressures [182, 183, 184, 185]. In fact, it undergoes structural phase transformations at higher pressure gradients [182]. Triclinic WO_3-I (P-1) transforms to monoclinic WO_3-II ($P2_1/c$) at 1 GPa, WO_3-II to WO_3-III ($P2_1/c$) at 27 GPa and to WO_3-IV above 37 GPa. Phases I and II are made of corner-sharing octahedra while phases III and IV are made of mixed edge or corner-sharing heptahedra. Above 30 GPa it is reported that WO_3 transforms to monoclinic WO_3-III which is stable up to 54 GPa [182]. Moreover, as evident from the figure 1.20 for different partial pressures of oxygen different stoichiometries of tungsten oxides are possible.

To conclude, we have identified from the literature review that there is a big gap in understanding the mechanism of ultrafast laser-assisted surface chemistry alterations at the surface of a material. This thesis hence is focused on filling this gap by investigating whether oxidation is necessary for the formation of HSFLs on tungsten, and to control the oxidation associated with HSFLs on tungsten by understanding the oxidation mechanism. This is done by performing laser irradiation in various gaseous conditions to generate HSFLs. Later the oxidation mechanism is established by focusing on HSFLs generated in ambient and vacuum conditions. Classical oxidation approaches based on diffusion are studied for femtosecond laser-assisted oxidation with an aim to control femtosecond laser-assisted oxidation.

* * *

Chapter 2

Experimental Methods

2.1 **Sample Preparation: Polishing Techniques**

2.2 **Ultrafast laser interaction with metals**

2.3 **Laser Techniques**

2.4 **Vacuum System**

2.5 **Determination of peak fluence : Liu or D^2 method**

2.6 **Characterisation Techniques**

"Experiment, the interpreter of nature, is a most valid mode of making inquiry."

-Francis Bacon, Novum Organum, 1620

This chapter deals with the instrumentation and techniques used for the experiments and characterizations carried out in this thesis. It starts with the different types of polishing performed (using the apparatus at École Nationale Supérieure Des Mines de Saint-Etienne) to prepare the sample surface for laser irradiation. This is followed by a description of the femtosecond laser system and the high vacuum system with a built-in sputtering apparatus. In the following section, Liu's method used to find the threshold fluence is described. Further, different characterization techniques focusing on topography and surface chemistry are proposed. Topography studies are done using different microscopy methods such as scanning electron microscopy (SEM), atomic force microscopy (AFM), and transmission electron microscopy (TEM). Surface chemical analyses are performed with methods including x-ray photoelectron spectroscopy (XPS), scanning TEM- electron dispersive spectroscopy (STEM-EDS), and STEM- electron energy loss spectroscopy (EELS). In addition, crystallography analysis using selected area diffraction (SAD) is presented. Finally, the setup used for measuring the wettability response of the laser irradiated surface is described.

2.1 Sample Preparation: Polishing Techniques

Polishing is the process of producing a smooth surface by grinding the surface or by using a chemical process. Nanostructure formation upon ultrafast laser irradiation can be influenced by the initial surface roughness. Sipe et al. [68] has proven that the surface roughness, confined to a region of height much less than the wavelength of light is responsible for the inhomogeneous energy absorption leading to the formation of nanostructures. Nakhoul et al. [60] have demonstrated this for the formation of fs laser-induced nanostructures on Ni where depending on the initial surface roughness (bumpy or spiky surfaces) the concentration and scale of nanostructures obtained were different. Hence to ensure the reproducibility of laser-generated structures and to reduce the contamination on the surface, it is important to establish a reproducible polishing technique. Poly-crystalline Tungsten (W) samples (Good-fellow SARL, Lille, France) were polished by mechanical polishing followed by electrochemical polishing to achieve the required nano-roughness needed for the formation of LIPSS (laser-induced periodic surface structures) on tungsten by a femtosecond laser of wavelength in the range of hundreds of nanometers.

Polymer Mounting

Poly-crystalline W samples of dimensions 10 $mm \times 10\ mm \times 1\ mm$ were mounted on a plastic mount. A special resin (ProntoFix, 40200108) is mixed with a hardener (in the ratio 2:1) to form a solution and is later polymerized to form the mount by keeping at 2 Bar pressure for 20 minutes. The W sample is placed on the mold and the mixture of resin and hardener is poured on the top of it so that after polymerization we get the tungsten sample to be stuck on the top of the polymer mount. These processes are shown in figure 2.1 (a) and (b). The purpose of such mounting is for the easiness of mechanical polishing. After mechanical polishing, the polymer mount was removed by grinding the mount on a polishing machine until the thickness was reduced and later cut off with a cutting machine very carefully, to ensure there were no remains of the resin that could outgas during the experiments involving high vacuum.

Mechanical Polishing

Mechanical polishing usually consists of rotating an extremely flat plate covered by a pad onto which the sample that is being polished is mounted upside down. The pressure applied to the surface, the duration of the polishing process, and the rotation speed are major factors influencing the outcome of mechanical polishing.

Here, mechanical polishing involves grinding with SiC discs using a force of 50 N and 300 rpm in steps of grit sizes P180, P320, P600, P1200, and P2500 discs. The apparatus used is shown in figure 2.1 (c). The grit size indicates the abrasive grade on the abrasive side of the sandpaper. P180, P320, P600, P1200, and P2500 discs correspond to 192 μm, 46 μm, 25.8 μm, 15.3 μm and 8.4 μm average grain size diameter of the sandpaper respectively. A $'P'$ in front of the grit size suggests that the product is graded in accordance with the Federation of European Producers of Abrasives (FEPA). This process is followed by diamond polishing with 3 μm and 1 μm particles solutions with a force of 60 N and 300 rpm. The final step is vibratory polishing with an SiO_2 solution, with nanoparticles of size 0.05 μm as shown in figure 2.1 (d). Later, to remove any SiO_2 residue the sample is

cleaned with a nonabrasive pad and hot water (figure 2.1 (e)). This is in addition to cleaning the samples in an ultrasonic bath between each step to yield better polishing results and avoid any accumulation of contaminants. An overview of the whole mechanical polishing process is given in table 2.1.

Type & size	Duration (minutes)	Speed (rpm)	Pressure (N)
SiC grits			
P180	40	300	50
P320	6	300	50
P600	6	300	50
P1200	6	300	50
P2500	5	300	50
Diamond polishing			
3 μ m	8	300	60
1 μ m	8	300	60
Vibratory polishing			
0.05 μ m	420	-	-

Table 2.1: Overview of the mechanical polishing parameters used

Electrochemical Polishing

Electrochemical or electrolytic polishing uses an electric current to dissolve a thin layer of metal ions into the electrolyte solution. This kind of polishing will improve the surface finish of the metal resulting in a smoother and reflective surface. The instrumentation consists of an electrolytic cell, in which the metal to be polished will act as the anode and an appropriate conductor (stainless steel) will act as the cathode. When an electric current passes through the electrolyte, in which the anode and cathode are present, the metal ions will be attracted to the cathode or stay in the solution. The apparatus that we use here is a Lectro-Pol5 machine by Struers company. The polishing parameters are the polishing voltage, polishing time, and the flow rate of the electrolyte. These parameters are determined depending on the finish we need and the metal that needs polishing.

W samples after mechanical polishing are unmounted from the resin, by cutting into the resin, for electrochemical polishing. Using a solution of NaOH and water (20 g of NaOH in 1000 ml of water) electrochemical polishing is done at 20 V for 20 seconds. This voltage and time is unique to this tungsten sample obtained after the specific mechanical polishing procedure explained above, so as to generate near to mirror-like finish on the samples. The setup used is given in figure 2.1 (f). This step produces an almost mirror-like finish (bright, shiny, reflective surfaces) for W samples. After electrochemical polishing, we were able to obtain W surfaces with an average roughness (Ra) smaller than 6 nm as shown in figure 2.2 (d) as measured by AFM. SEM (figure 2.2 (a) and (b)) and AFM (figure 2.2 (c) and (d)) images after mechanical and electrochemical polishing show how important is electrochemical polishing in producing a smooth W surface. In addition, since this is a study of surface chemistry we have ensured that the W surface is not contaminated by any of the polishing chemicals by performing an SEM-EDX spectra analysis as shown in figure 2.2 (e) and (f).

All polishing required for the experiments was done at Ecole des Mines de Saint-Étienne with the help of Dr.Anthony Nakhoul.

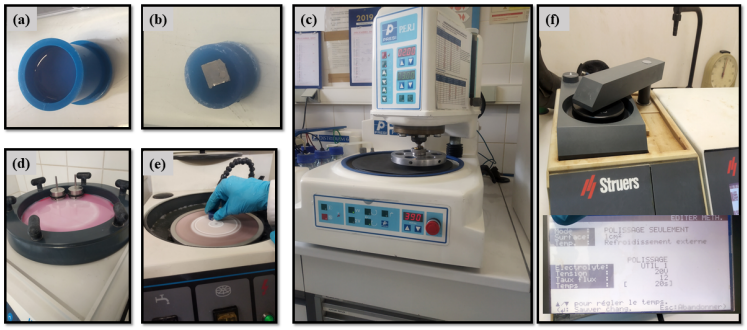

Figure 2.1: (a)Plastic mount preparation (b) W mounted on the polymer mount (c) SiC grinding apparatus (d) Vibratory polishing (e) Hot water cleaning (f) Electrochemical polishing.

2.2 Laser Techniques

2.2.1 Femtosecond Laser System

A Femtosecond laser system generates ultrashort optical pulses on the order of 10^{-15} seconds. For this thesis work, we are using a Ti: Sapphire laser equipped with Ti: sapphire crystal. The whole system consists of a pump laser, an oscillator, and an amplifier.

Amplifier pumping is achieved by a Q-switched, diode-pumped, solid-state nanosecond laser that is an Nd:YAG laser. Using an LBO (Lithium Borate) crystal it produces 20 mJ pulses with wavelength, $\lambda = 532nm$ and 1 kHz repetition rate.

The oscillator is a mode-locked Ti: Sapphire laser (Mantis, Coherent) that generates femtosecond pulses of more than 300 mW of average power at the center wavelength of 800 nm and frequency of 80 MHz with a bandwidth of more than 70 nm, which can be compressed to less than 20 fs. Mode locking produces ultrashort pulses by producing constructive interference between different modes inside the resonant cavity by inducing a fixed phase relationship between these longitudinal modes. It is usually used for seeding short pulse amplifier to generate tunable high energy.

The amplifier consists of a stretcher, regenerative amplifier, and a compressor. As the name suggests, the stretcher consists of a grating that will stretch out the pulse in time. In the regenerative amplifier, this pulse will be amplified and the compressor which consists of another grating will compress the pulse to the ultrashort time domain. In other words, to amplify the laser pulse without damaging the active medium Chirped Pulse Amplification (CPA) is employed [24]. This is a concept based on the principle of frequency drift amplification as developed by the 2018 Nobel prize winners Gerard Mourou and Donna Strickland. In this technique a pair of gratings are used, where initially the first pair act as a stretcher, stretching the pulse duration to the picosecond regime. The compressor gratings then compress the pulses back into short pulses. The given figure 2.3 depicts how this happens in the Coherent LEGEND laser.

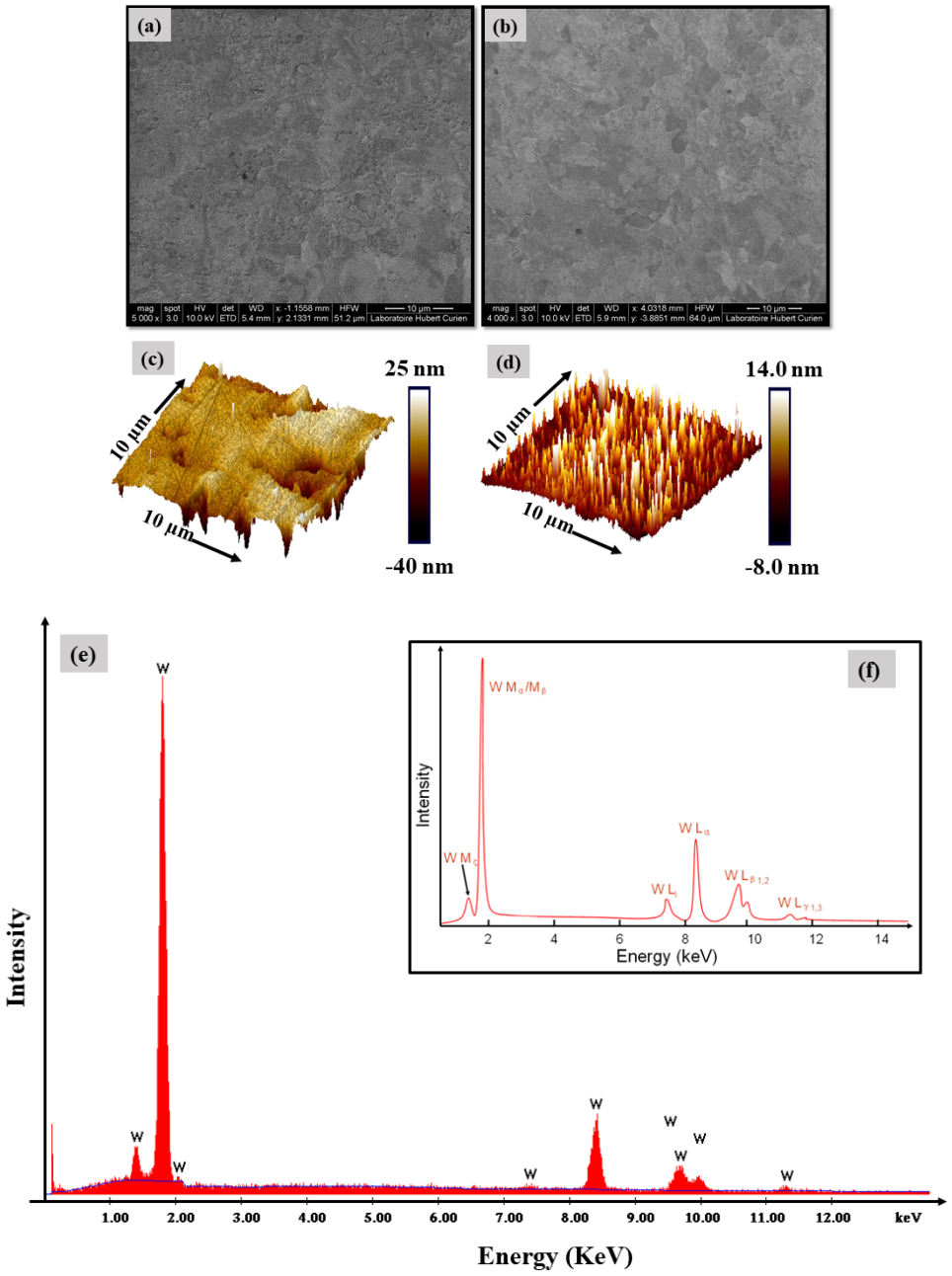

Figure 2.2: (a) SEM image after mechanical polishing (b) SEM image after electrochemical polishing (c) AFM profile after mechanical polishing (d)AFM profile after electrochemical polishing (e) SEM-EDX spectra obtained after electrochemical polishing which can be compared with full standard EDX spectra of tungsten material in (f), Reprinted from [186].

The laser beam trajectory used in this experiment is given in figure 2.4 (a). The femtosecond output from the Coherent laser is directed to a converging lens with the help of mirrors and then focused onto the sample kept inside a vacuum chamber.

While at uOttawa, the femtosecond laser was a linearly polarized Yb: KGW laser (PHAROS, Light Conversion, Inc) with $\lambda = 1030\ nm$, 1 KHz repetition rate, and 300 fs in pulse duration. The large-area laser

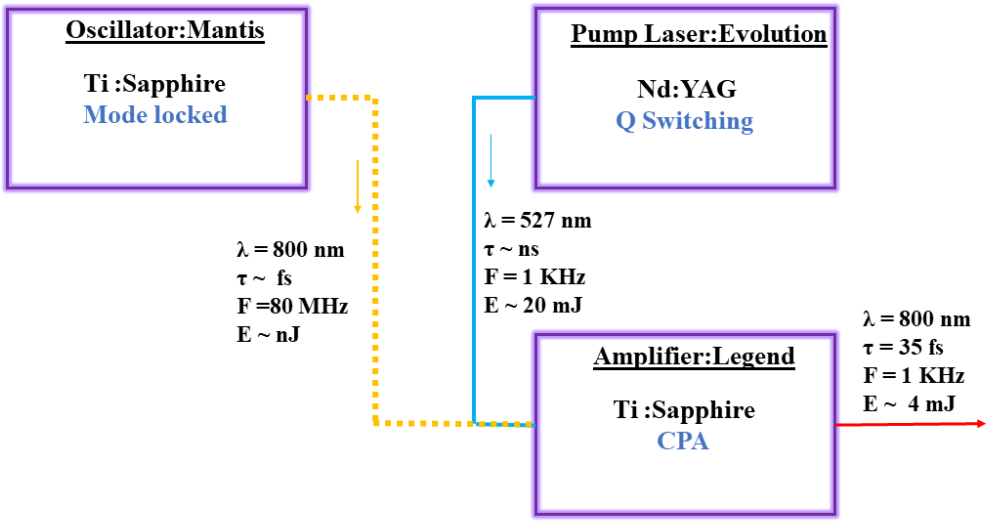

Figure 2.3: Schematics of the generation of femtosecond pulses.

irradiations were performed by using a galvanometric scanner (AEROTECH AGV-10 HPO) mounted on a positioning lift stage as shown in figure 2.4 (b).

2.3 Vacuum System

For most experiments, the vacuum chamber used is similar to that used for Pulse Laser Deposition (PLD). This ultrahigh vacuum set-up can go down to 10^{-8} mbars of pressure and is equipped with an in-situ sputtering apparatus and an external heating mechanism. Dry pumping using a turbo pump along with the heating of the chamber and nitrogen venting ensures minimum contamination inside the vacuum chamber. The setup consists of two pumps: a primary pump, which takes the pressure down to 10^{-2} mbars, and a secondary pump (a turbo pump, VINCI Technologies, Nanterre, France) which starts after this pressure is achieved (after closing primary pump) and can go down to 10^{-8} mbars.

The sputtering setup relies on a potential difference between the vacuum chamber which is grounded and steel (the substrate holder) which is at a negative potential generated by DC current. This causes the generation of positive ions of a gas (usually Argon) filling the chamber. These ions get accelerated to the cathode (substrate holder) and sputter off the target surface. This is shown in figure 2.4 (c).

It is possible to fill the chamber with different types of gases like nitrogen, argon, and even air by controlling the pressure using the knobs attached to the valves and the pressure gauges (Leybold vakuum, ConvecTorr). Primary vacuum, 10^{-2} mbars, was achieved before introducing the gases (to be at a pressure ~ 10 $mbars$). To avoid any change in the fluence delivered by the laser, all irradiations in different environmental conditions were performed by keeping the sample inside a vacuum chamber.

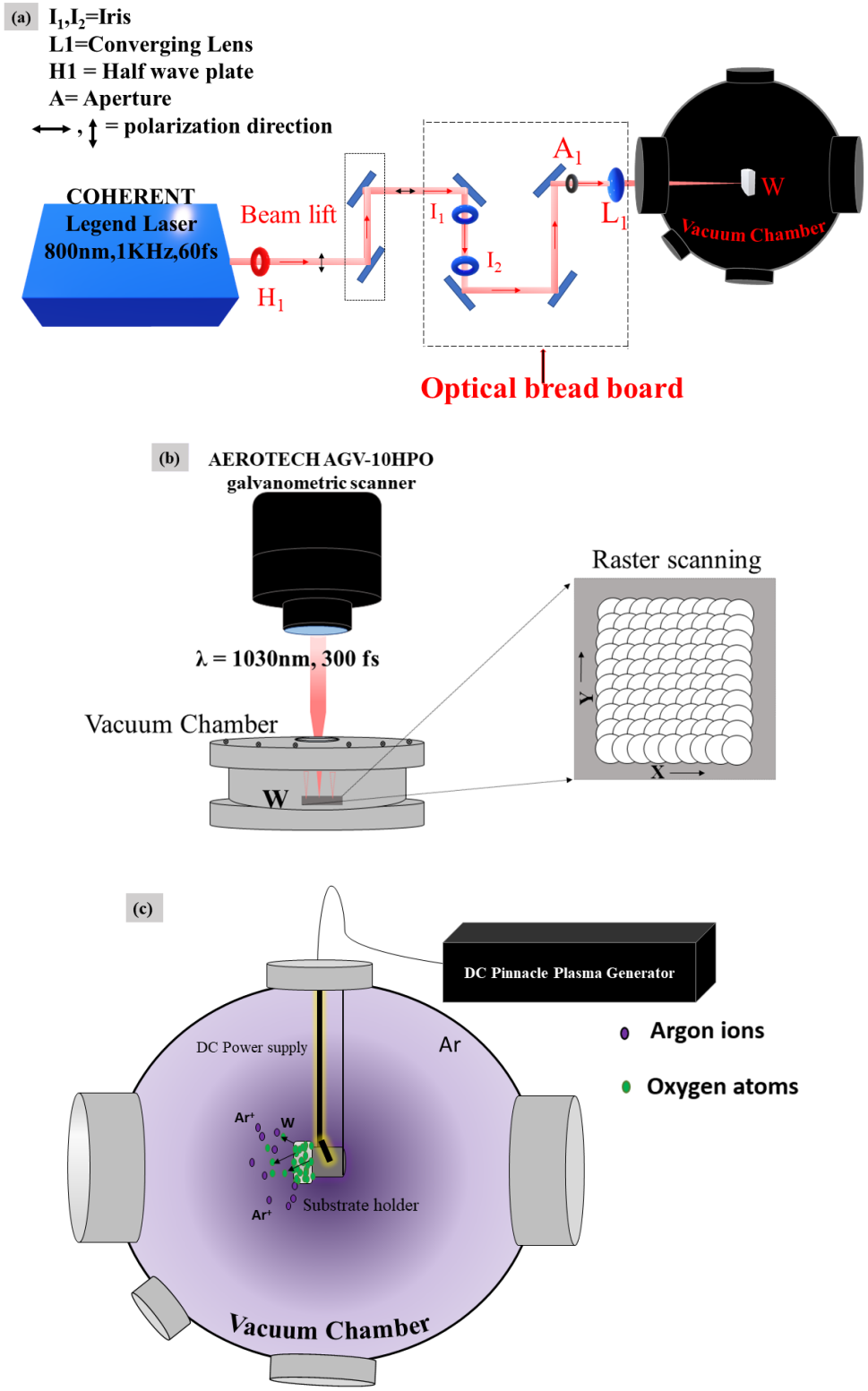

Figure 2.4: (a), Laser beam trajectory used at labHC: laser path focused with a converging lens to the target inside a vacuum chamber. (b), Laser beam trajectory used at uOttawa: raster scanning was achieved for a sample kept inside the vacuum chamber by using a galvanometric scanner. (c), The vacuum system with the in-built sputtering apparatus.

2.4 Determination of peak fluence : Liu or D^2 method

Fluence is the energy per pulse (E) per unit area expressed in J/cm^2. Femtosecond lasers usually have a non-uniform Gaussian distribution of energy as shown in figure 2.5 (a). So the average energy of the pulse is not the same everywhere. Hence we need a method for relating the energy of the pulse and the area of the ablated surface which is given by Liu [187].

For a Gaussian beam, the spatial fluence profile is given by,

$$F(r) = F_p \; e^{-2r^2/\omega_0^2} \tag{2.1}$$

where, F(r) is the local fluence at radial position r, F_p is the peak fluence, ω_o is the radial Gaussian beam waist at $(\frac{1}{e})^2$ of the peak value.

Liu's method, defines the ablation fluence threshold, F_{th}, as the local fluence corresponding to the border of the laser-induced crater, with a radius R. Hence, we can write,

$$F_{th} = F_p \; e^{-2R^2/\omega_0^2} \tag{2.2}$$

Taking the logarithm of this equation we can write,

$$R^2 = \frac{\omega_0^2}{2} \; ln\frac{F_p}{F_{th}} \tag{2.3}$$

But experimentally we measure not the peak fluence but the integrated pulse energy, E. If F_p is the peak fluence in J/cm^2, E is the energy deposited on the surface (in joules) and EBA is the effective beam area of impact, then,

$$E = \iint_S F(x,y) \; ds = F_p \; . \; EBA \tag{2.4}$$

For a Gaussian beam, by solving for the above equation one can get,

$$EBA = \frac{\pi\omega_0^2}{2} \tag{2.5}$$

Giving us,

$$F_p = \frac{2E}{\pi\omega_0^2} \tag{2.6}$$

If E_{th} is the ablation threshold energy, that is the minimum energy of the laser pulse to produce ablation then,

$$F_{th} = \frac{2E_{th}}{\pi\omega_0^2} \tag{2.7}$$

For an ablated area πR^2, by substituting equations 2.6 and 2.7 in equation 2.3 we can write,

$$R^2 = \frac{\omega_0^2}{2}\, ln\frac{E}{E_{th}} \tag{2.8}$$

This is the main equation of the Liu's method. When we plot a graph with ln(E) in the x-axis and R^2 in the y-axis we get a straight line. The Gaussian beam waist (ω_0) is obtained from the slope of this line. The threshold energy and hence the threshold fluence can be obtained from the x-axis intercept. This method is also called D^2 method since we can replace R^2 with the diameter of the crater D^2 and get the following equation,

$$D^2 = 2\ \omega_0^2\ ln\frac{E}{E_{th}} \tag{2.9}$$

If D^2 and ln(E) vary linearly with slope 's'. Hence, ω_0 can be written as,

$$\omega_0 = \sqrt{s/2} \tag{2.10}$$

If 's' is the slope and 'a' is the x-intercept for the straight line related by $D^2 = f(ln(E))$ given by,

$$s \times ln(E_{th}) + b = 0 \tag{2.11}$$

we get

$$E_{th} = exp(-a/s) \tag{2.12}$$

For our experiments, the peak ablation fluence is found by irradiating the tungsten surface at different energies, E, for the same number of pulses. Later the surface area of the impacts is measured by an optical microscope with the visible circle of damage due to the laser as the reference. Then the square of the surface area (SA^2) of laser impacts versus the energy is plotted and the data was fitted for a straight line as shown in figure (2.5) (b). As an example, for tungsten, the peak ablation threshold fluence corresponding to 25 pulses (N=25), which was the number of pulses used mostly for getting the main results, was found to be, $F_p = 0.24\ J/cm^2$.

2.5 Characterisation Techniques

A combination of various characterization techniques is used for obtaining information on the topographical, surface chemical, and crystallographic modifications accompanied by laser irradiations. The topographical changes are analyzed with scanning electron microscopy (SEM), atomic force microscopy (AFM), and Transmission electron microscopy (TEM). Electron microscopes like SEM and TEM use an electron beam as probes which produces a broad range of signal electrons after interacting with the material as shown in figure 2.6 [188]. The high resolution of an electron microscope comes from the short wavelengths associated with high energy electrons. Surface chemical variations are examined with the help of surface-sensitive characterization methods like X-ray photo-electron spectroscopy (XPS), Scanning TEM (STEM) energy dispersive X-ray spectroscopy (EDX), and STEM-electron energy loss spectroscopy (EELS). The surface chemical characterization techniques used here have an interaction depths of only tens of nanometers. In addition, TEM has a technique called selected area diffraction (SAD) that provides

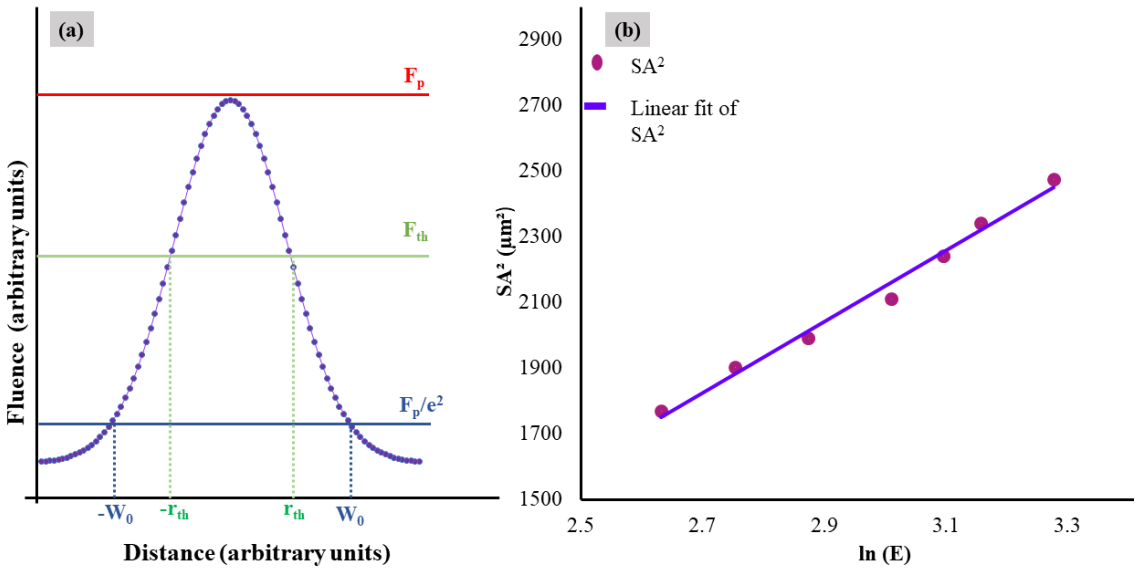

Figure 2.5: (a) Radial distribution of fluence for a Gaussian beam. (b) Linear fit obtained on laser-ablated areas on a Tungsten sample at the focal plane corresponding to different energies to determine the peak ablation threshold.

crystallographic information on the material. Finally, the physicochemical response of the laser-textured surface was characterized with a home-built Contact Angle (CA) measurement set up to analyze the wetting behavior of the laser-textured surface.

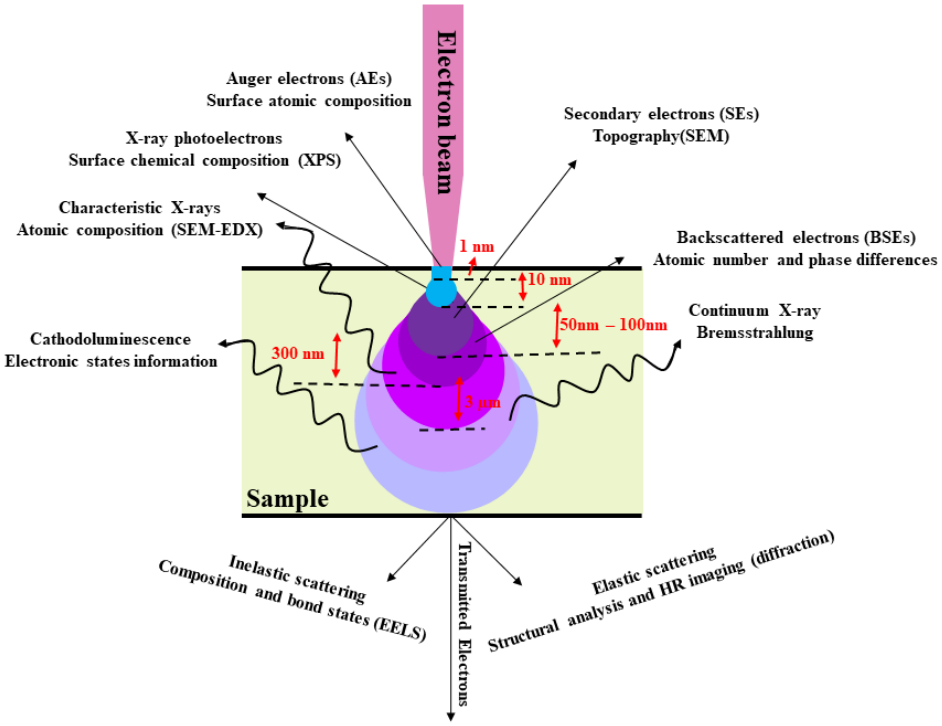

Figure 2.6: Different signals generated as a result of electron-matter interaction, inspired from [189].

2.5.1 Topography Characterisations

SEM Analysis

SEM is one of the most widely used types of electron microscopes. It examines the microscopic surface structures by scanning the surface of materials using a focused electron beam. The signal electrons collected by a detector is then amplified and an image is generated. As the electron beam strikes the surface, part of the signal electrons are produced by elastic scattering and are called back-scattered electrons (BSEs) and used to achieve compositional contrast while other electron signals are produced by inelastic scattering called secondary electrons (SEs) and are useful for giving topographical contrast. The difference in electron signal intensities obtained from the sample surface forms the SEM images with a spatial resolution as good as 1 nm [190].

The SEM instrumentation used to image most of the surfaces in this project is an FEI Novanano SEM 200, allowing a lateral resolution of 1 nm. The detector used is the Through lens detector (TLD) that allows the detection of SEs to obtain images with ultra-high resolution and works in high vacuum conditions. Some of the SEM analysis was performed at the Centre for Research in Photonics (CRPuO), University of Ottawa (UOttawa), and the instrument used there is a Zeiss Gemini SEM 500 field emission microscope. For both the instruments the images were obtained with a voltage within the range 10 kV to 20 kV for a working distance around 5 mm. Since the SEM apparatus only gives us a 2-D images and no information on roughness or the amplitude of the laser-generated surfaces, AFM was used to obtain more detailed topographical information.

AFM Analysis

AFM uses near-field forces between atoms of the probe tip and the surface to generate surface topography information. The sensor of an AFM is a cantilever onto which a tip is mounted. The force between the tip and sample generates elastic bending of the cantilever and this deflection is converted to topographical information. It has static and dynamic operational modes. In static mode which are usually contact mode, the cantilever deflects statically and the feedback loop maintains this set value of deflection during scanning. In dynamic mode, which could be contact or non-contact or intermittent contact modes, the cantilever oscillates at a fixed frequency and the feedback loop tries to maintain a set value of the amplitude of oscillation during scanning [191]. Generally, AFM has a lateral resolution of approximately 30 nm and a vertical resolution of 0.1 nm [192].

In our experiments, we use BRUKER ICON AFM apparatus, which works in the intermittent contact mode or the tapping mode both at LabHC and uOttawa. Mappings were obtained with Scan Assist in Air mode that were able to generate a resolution of 2 nm with 1 kHz scan frequency. The tip of the cantilever used for the measurements in this mode is made of silicon nitride. In this mode, the cantilever oscillates and the tip touches the surface lightly to avoid surface damage. This slight contact reduces the cantilever oscillation. This change in oscillation is used to identify the surface features. The radius of the tip was around 10 nm to measure the few nanometers of amplitude and height of some nanostructures generated. The measured roughness given in the thesis is the average roughness (Ra) measured over the area.

While SEM and AFM are good indicators of topography analysis, TEM analysis will help us to reaffirm the topography data in addition to providing sub-topography information.

TEM analysis

TEM, like SEM, is also an electron microscope, where the signal electrons are transmitted through the sample. Here the electron beam illuminates the area of analysis rather than hitting it in a small spot area like in SEM. The samples must be so thin that they should be transparent to the incoming electrons. This is achieved by preparing lamellae. A lamella with a thickness smaller than 100 nm and hence transparent to the electron beam is obtained by ion milling. Initially, the sample undergoes electron beam-induced deposition (EBID) of a platinum layer as thick as 300 nm followed by ion beam-induced deposition (IBID) of a carbon layer with a thickness between 2 μm and 3 μm as shown in figure 2.7 (a). Finally, this part of the sample (approximately 15 $\mu m \times 25$ μm in dimensions) is lifted out by ion milling and is placed on a Cu grid (figure 2.7 (b) and (c)). Such a lamella is again thinned using the ion beam to attain a thickness as small than 100 nm for a length of approximately 3 μm at the center of the lamella as shown in figure 2.7 (e) and (f).

STEM is another mode in TEM where the electron beam scans the surface like that in SEM. It consists of a source, condenser lens, specimen stage, objective lens, and a projector lens just like in any light microscope, except that it has an electron beam as the light source and an electromagnetic lens for guiding the electron beam to the sample. The scattered electrons are then projected onto a fluorescent screen coupled with a CCD camera. The mechanisms of the generation of images by scattered electrons are mass-density contrast, diffraction contrast, and phase contrast. Mass density contrast results from the deflection of electrons due to the interaction between electrons and an atomic nucleus. Diffraction contrast is the primary mechanism of image formation in crystalline materials. Phase contrast is often referred to as high-resolution TEM (HRTEM) and utilizes the phase difference in electron waves to generate contrast [191]. Using HRTEM imaging, it is possible to reach a spatial resolution in the range of 0.05 nm [193].

In TEM/STEM the primary detector called the bright field (BF) detector collects the forward scattered electrons on the axis. The annular dark-field (ADF) detector collects the scattered electrons in small angles. The high angular annular dark field (HAADF) detector collects the electrons scattered at high angles. In our experiments, we used a JEOL NEOARM instrument (with HAADF image resolution up to 1 to 2 Angstroms) for TEM with an electron acceleration voltage of 200 kV for various detectors. This instrument is equipped with STEM-EELS and STEM-EDX techniques which will be discussed in the next sections.

The FIB extraction in addition to TEM and STEM techniques were done with the help of S. Reynaud.

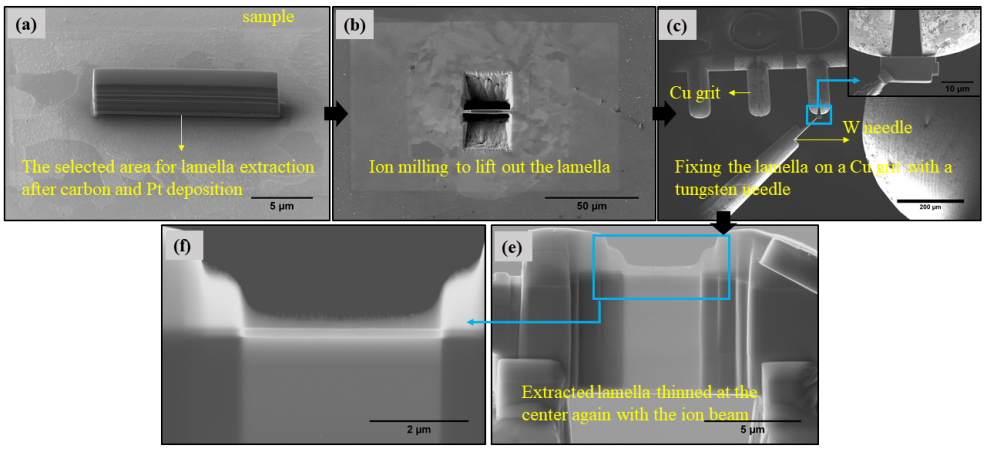

Figure 2.7: Different stages involved in ion milling

2.5.2 Chemical Characterisations

XPS Analysis

This technique uses electrons emitted using photon energy for elemental analysis. The X-ray photons cause the photo-emission of electrons from the atoms whose binding energy depends on both the atom's nature and its chemical bond. Basically, an X-ray photon with sufficient energy interacts with the specimen surface and knocks out an inner shell electron. This electron is called an X-ray photo-electron. If we assume such a photo-electron escaped from the K shell of an atom with kinetic energy E_k we can calculate the binding energy (BE) [191],

$$E_B = h\nu - E_K - \phi \tag{2.13}$$

ϕ represents the energy required for an electron to escape from the surface, h is Plank's constant, and ν is the frequency.

The XPS spectra are the plot of binding energy against the intensity of photo-electrons. The peak positions of elements in XPS spectra are sensitive to their chemical status. This is called the chemical shift in which the position of the peak is shifted to the side of greater BE for a more electronegative atom. This will also result in an increase in the magnitude of the chemical shift as the oxidation state increases for a metal.

For our purposes, we use a Kratos Axis Nova spectrometer (with an energy resolution of < 0.48 eV, given by the FWHM of Ag 3d) equipped with an Al X-ray source at Queen's University Canada, with energy 1486.69 eV and operates in ultrahigh vacuum, 10^{-9} torr, done by Dr. Gabriele Schatte. The analyzed area is about 55 $\mu m^2 \times 55\ \mu m^2$. The spectra measured with ESCApe software are analyzed using the CasaXPS software.

STEM-EDS and STEM-EELS Analysis

We can analyze the surface chemical composition of a material using the EDX and EELS techniques. EDX/EDS is a type of X-ray spectroscopy that enables elemental analysis while examining the micro-structure of materials by using the characteristic X-rays emitted by the surface to identify chemical elements when an electron beam is incident on it. When a high-energy particle strikes an electron in the inner shell of an atom, the energy of the particle can be high enough to knock an electron out and hence the atom becomes ionized. This excited atom then goes back to its normal state after an outer shell electron refills the inner shell hole by the emission of an X-ray photon and this is called a characteristic X-ray. EDS spectra are a plot of the intensity of this characteristic X-ray against the X-ray energy range. Both qualitative and quantitative analysis is theoretically possible with STEM-EDX. But for an accurate quantitative analysis, it is necessary to analyze separate standard samples containing the elements under the same apparatus set-up conditions.

In the case of EELS, a beam of electrons with a known range of kinetic energy incident on the specimen surface generates signal electrons produced by inelastic scattering. The energy distribution of all inelastically scattered electrons provides information about the local environment of the atomic electrons which can be related to the physical and chemical properties of the specimen. A typical EELS spectra consist of a plot of the range of energy loss against the intensity of signal electrons.

In this thesis, we used a JEOL NEOARM instrumentation where a color mapping of chemical composition using both these techniques are also possible, with the EDX analysis software and the gatan software for EELS analysis. EELS and EDS analysis was done with a single pixel dimension of 0.25 nm $\times$ 0.25 nm for a total image of 512 $\times$ 512 pixel count with an exposure time of 2 $\times$ 10^{-4} seconds for a single pixel. This gives the total acquisition time of around 15 minutes to 20 minutes for a single image.

2.5.3 Crystallography Characterisation

SAD Analysis

Since the lamallae used in the STEM/TEM analysis is transparent to the electrons accelerated at very high voltages, some of the electrons will be diffracted by the crystal lattice (will act as a diffraction grating) at particular angles while others will be transmitted through it without any diffraction. The transmitted beams will intersect at the optical axis and the diffracted beams will form diffraction pattern on the back-focal plane of the objective lens. This is recorded by the camera in the TEM. This pattern is useful in analyzing the crystal structure of the specimen. This is because the diffracted beams intersect at certain distance from the optic axis corresponding to the inter-planar distance of the planes diffracting the beams. Constructive interference of these diffracted electron beam generates an intensity spot on the screen from a particular lattice plane (hkl). This is called a SAD pattern composed of several such bright spots. The formation mechanism of the diffraction pattern in TEM is given in figure 2.8. SAD is called 'selected area diffraction' because it is possible to select a particular area of the sample to be analysed from which the diffraction pattern can be acquired. This is done by using selected area apertures

of various sizes located below the sample.

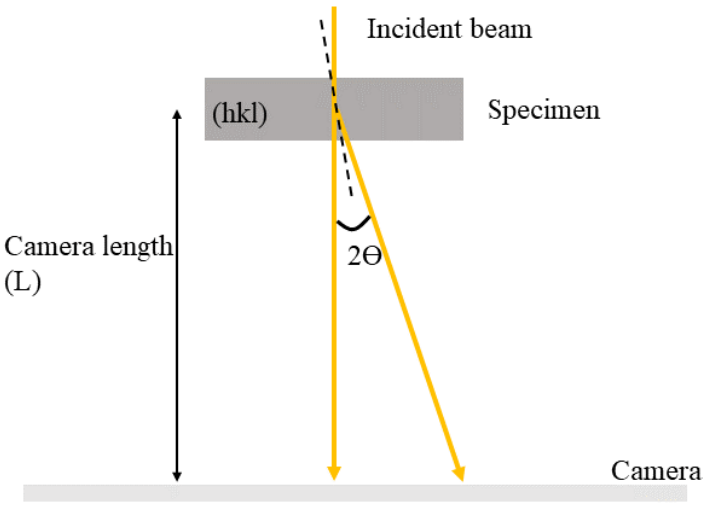

Figure 2.8: Formation of the diffraction pattern in TEM, adapted from [191].

Bragg's law for small angles is given by,

$$\lambda = 2d\theta \tag{2.14}$$

Where λ is the wavelength of the incoming wave, d is the crystallographic spacing and θ is the angle of incidence.

From the figure 2.8 the geometric relationship among *theta*, R and L is given by [191],

$$\lambda L = Rd \tag{2.15}$$

where L is the distance between the crystal and the camera of the TEM. Equation 2.15 is the basic equation for electron diffraction in the TEM. So it is possible to find the crystallographic plane spacing by measuring R.

In practice, initially we can obtain the diffraction pattern similar to the SAD pattern with the FFT of the diffraction pattern if the imaging is done on the zone axis, which is how the analysis were performed in this thesis. Then we have to index the pattern to know the crystal planes and crystal structure, which was done using the Dif-Wshp23 software (developed by T. Epicier of INSA Lyon, [194]).

2.5.4 Physico-chemical Characterisation

Wettability Analysis

To analyze the physicochemical behavior of the laser-irradiated surface, wettability measurements were carried out by measuring the water contact angle (WCA) of the W surfaces. Different cases of wettability of a solid surface are hydrophobicity and hydrophilicity based on the contact between the solid-liquid interface. Contact Angle (CA) determines the degree of wetting of a surface by a liquid. The contact angle is defined as the angle

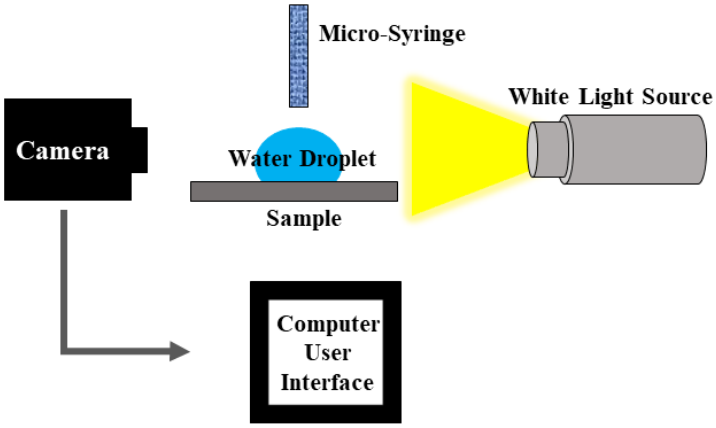

Figure 2.9: Schematic illustration for set up used for measuring the WCA of the sample.

formed by the intersection of the liquid-solid interface and the liquid-vapor interface (geometrically acquired by applying a tangent line from the contact point along the liquid-vapor interface in the droplet profile). Low CA ($<90^0$) indicates hydrophilicity and high CA ($>90^0$), hydrophobicity. Further, if the CA is nearly 0^0 it is termed as superhydrophilic and for CA$>150^0$, superhydrophobic [195].

For our experiments, we measure the static contact angle (the contact angle in which the contact area between the liquid and the solid does not change during the measurements) using a sessile drop technique after depositing 1 μl of deionized water from a computer-controlled micro-syringe on the sample surface, schematically illustrated in figure 2.9. The CCD camera acquires the image of the droplet and is coupled to the computer where the video/image capturing can be done by the user to measure the WCA. The WCA can later be extracted with the 'contact angle' plugin in the Image J software [196]. This WCA can be used as a good indicator for changes in the surface chemistry of laser-fabricated surfaces.

In conclusion, these are the state-of-the-art instrumentation and setups that were utilized at Hubert Curien Laboratory, France, and the University of Ottawa, Canada. All these advanced characterization techniques along with the experimental setups were crucial for this work to yield important results and to reach significant conclusions regarding the topography, sub-topography, surface chemical, and physio-chemical aspects of the laser-irradiated surface.

* * *

Chapter 3

Oxidation - a precondition for LIPSS formation?

"The light-induced formation of arranged, assembled, and self-organized structures on solid surfaces has a steady stream of deepened and extended research activity due to the ever-growing technological importance of on-demand tailored nanomaterials and surface functionalization"

- Razvan Stoian & Jorn Bonse, Chapter 5, 'Ultrafast Laser Nanostructuring : The Pursuit of Extreme Scales, 2023'

As seen from chapter one, one of the important questions to address will be - Is oxidation a precondition for LIPSS formation? This chapter aims to answer this question. Before understanding the effect of oxidation on nanostructure formation, it is important to know what kind of topographies can be achieved on Tungsten surfaces under femtosecond laser irradiation. Hence, this chapter starts with the various types of laser-induced nanostructures (LSFLs, HSFLs, and nano bumps) that can be generated on W. These nanostructures are observed for particular combinations of laser fluence and number of laser pulses. In addition, different nanostructures generated under different gaseous conditions are also presented. This is followed by a study of the influence of oxidation (laser-generated and native oxide layer) on nanostructure formation. Finally, subsurface void formation observed using STEM and explained by TTM-MD simulations help us propose a mechanism for HSFL formation on W based on a hydro-dynamical approach rather than an oxidation-based model.

3.1 Types of Nanostructures

When a laser interacts with the tungsten surface, different types of topographical modifications can be achieved depending on the laser parameters used. In this work, we obtained LSFLs, HSFLs, and nano-bumps for laser pulses of 800 nm wavelength, 1 KHz pulse repetition rate, and set to 60 fs pulse duration. Below is a general overview of the common type of nanostructures that will be encountered in this chapter.

Low Spatial Frequency LIPSS (LSFLs)

LSFLs are Low Spatial Frequency LIPSS and in the following experiments, they have a period, $\Lambda = 500\,nm - 700\,nm$ close to the laser wavelength ($\lambda = 800\ nm$) and oriented perpendicular to the laser beam polarization for all peak fluence (F_p) and number of pulses (N) combinations. They have an amplitude that varies between 150 nm and 200 nm measured from AFM profiles.

High Spatial Frequency LIPPS (HSFLs)

HSFLs are High Spatial Frequency LIPSS and they have a period much smaller than λ. HSFLs were observed in three different situations. One type of HSFL has an orientation perpendicular to the laser polarisation, the other parallel to the laser polarization, and finally, HSFLs covering the top of the LSFLs are also observed. In all cases, they are seen to have a period between 50 nm to 150 nm and sub-20 nm amplitudes.

Nano-bumps

These are bump-like structures observed for a combination of a large number of pulses and small fluences. They have an average height of 50 nm and an average width of 100 nm.

3.2 Generation of nanostructures on Tungsten

The three main types of nanostructures described above were observed on femtosecond laser irradiated W using the following conditions: (1) by using the non-uniform fluence distribution from the Gaussian laser beam, (2) by fixing the peak fluence (F_p) and varying number of pulses (N), (3) by varying the F_p and fixing N.

3.2.1 Gaussian distribution of fluence and nanostructure evolution

Gaussian beams have a unique radial fluence distribution where the maximum fluence at the center decreases towards the periphery of the beam. **When such a beam interacts with W surfaces, a circular laser spot is created within which HSFLs, LSFLs, and even some nano-bumps are formed depending on the fluence deposition at the surface**. For $Fp = 0.52\ J/cm^2$ and N=200 the evolution of topography modification from the periphery to the center and hence when going from a smaller to a higher fluence, nano-bumps, 'intermediate' region (a stage between nano-bumps and HSFLs), HSFLs, and finally, LSFLs are observed respectively as

shown in figure 3.1 (a) & (b).

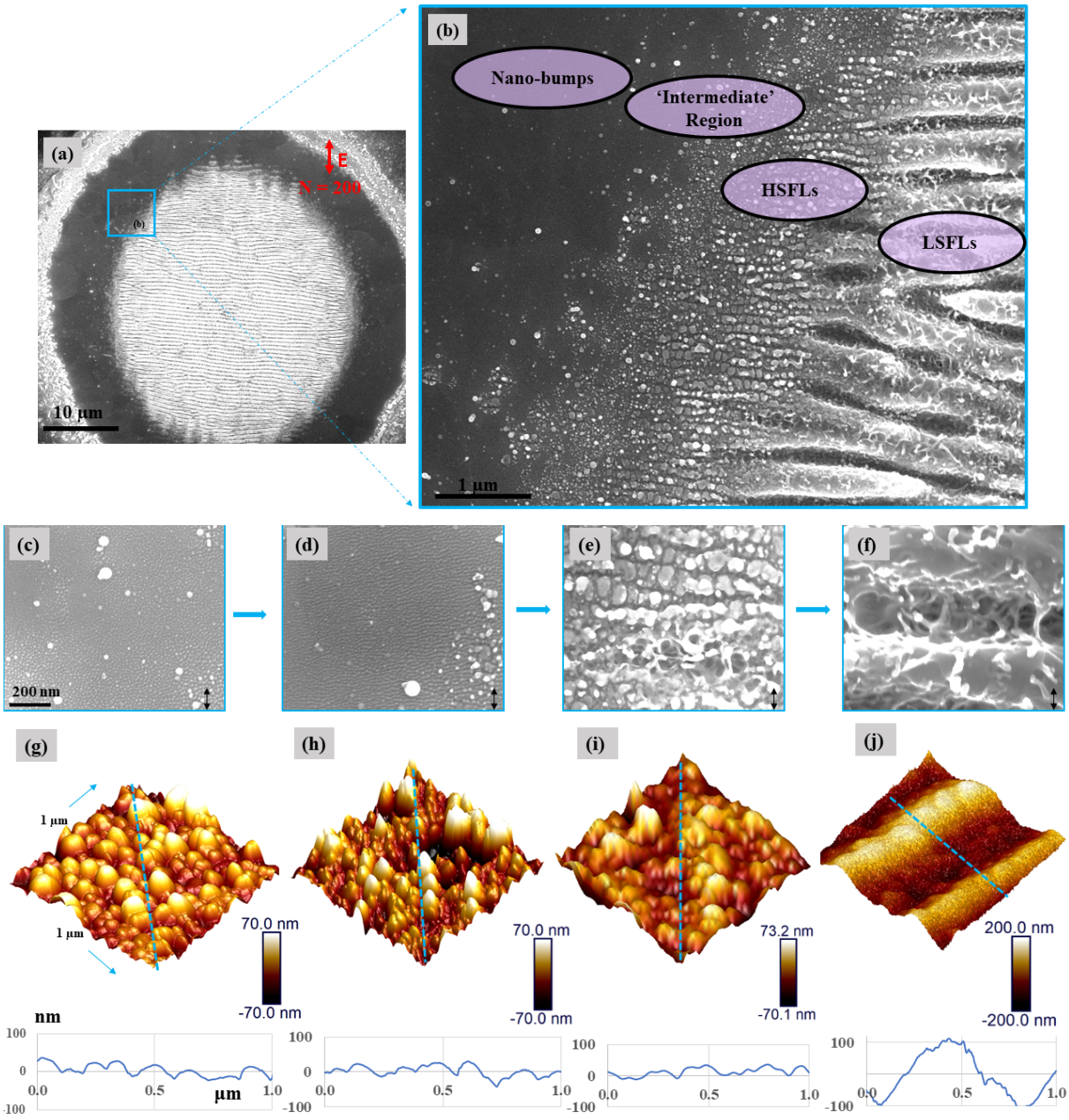

Figure 3.1: (a) & (b) Evolution of nanostructures with the Gaussian distribution of fluence for $Fp = 0.52\ J/cm^2$ and N=200.(c), (d), (e), (f): SEM images of nano-bumps, intermediate region or oriented nano bumps, HSFLs, and LSFLs respectively. (g), (h), (i), (j): AFM images of nano-bumps, intermediate or oriented nano-bumps region, HSFLs, and LSFLs respectively along with their height profile.

When we plot this Gaussian distribution of fluence at $Fp = 0.52\ J/cm^2$ and N= 200 (given in figure 3.2 (a)), it is evident that the formation of LSFLs takes place above 0.26 J/cm^2, that they are perpendicular to the polarization and with a period of approximately 600 nm and an amplitude of approximately 200 nm. HSFLs are observed between 0.23 J/cm^2 and 0.26 J/cm^2, perpendicular to the direction of polarisation, and have an amplitude of 50 nm. Above 0.19 J/cm^2 there is an intermediate region between nano-bumps and HSFLs. They are 'intermediate' since, from the top view SEM image, they appear to be periodic and are oriented like HSFLs

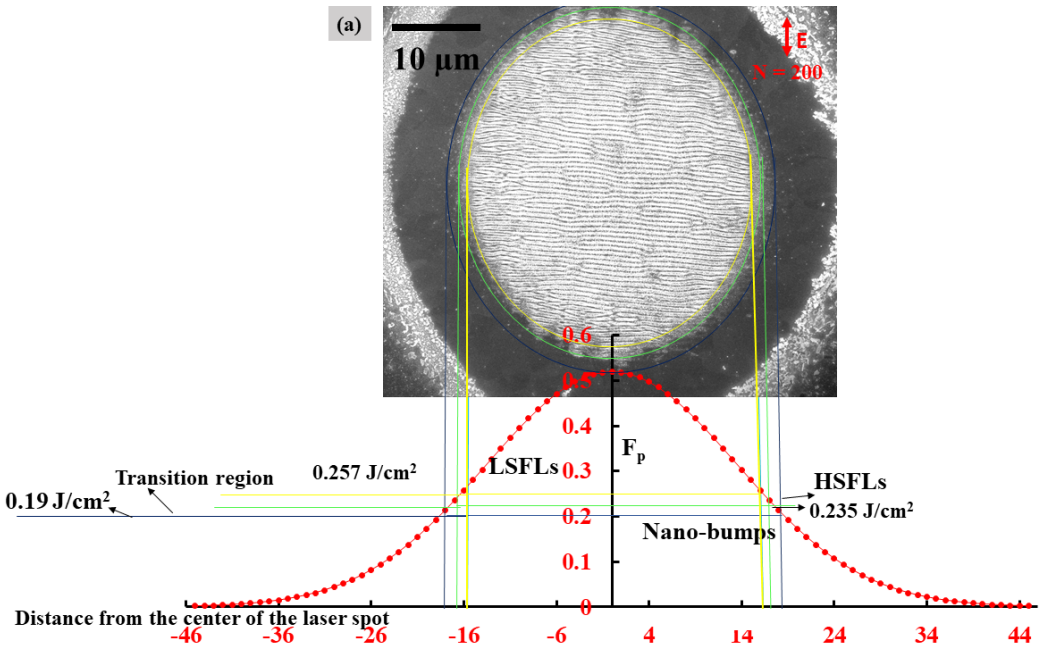

Figure 3.2: (a) Gaussian distribution of fluence and nanostructure evolution for $Fp = 0.52\ J/cm^2$ and N=200.

but AFM images show nano-bumps with a spiky appearance as shown in figure 3.1 (h) and (i) respectively. Below 0.19 J/cm^2 nano-bumps are formed. These bumps have a height of 20 nm and a width of 150 nm. The high resolution (HR) SEM images for each of these regions are shown in figure 3.1 (c)-(f).

As the fluence increases the nano-bumps orient themselves perpendicular to the laser polarization and join together to form HSFLs and LSFLs. 3-D AFM images (figure 3.1 (g)-(j)), show independent bump-like structures on the surface for the first two cases (nano-bumps and intermediate region), compared to the more oriented, bump-free situation for HSFLs and LSFLs.

3.2.2 Changing fluence (F_p) and nanostructure evolution

The change in surface topography was studied by changing the peak fluence F_p and fixing the number of pulses at N = 200. The results are shown in figure 3.3. At higher fluences (0.56 J/cm^2 and 0.35 J/cm^2) LSFLs are oriented perpendicular to the laser polarization. As the fluence increases, LSFL with a larger period ($\Lambda = 700\ nm$) are present and that period decreases ($\Lambda = 500\ nm$). Below that fluence (0.26 J/cm^2) a mix of HSFLs and LSFLs is observed, with HSFLs on top of LSFLs. LSFLs and HSFLs were seen to be perpendicular to the laser polarization. At lower fluences ($< 0.22\ J/cm^2$) nano-bumps were observed. It is interesting to see that these nano-bumps are arranged in an LSFL-like array as shown in figure 3.3 (a).

3.2.3 Changing N and nanostrucutre evolution

Experiments were performed by fixing the fluence at $F_p = 0.52\ J/cm^2$ and changing N (N=5, 25, 55, 100). The results are shown in figure 3.4. At N=5 we see HSFLs parallel to the direction of polarisation with a period (Λ) of approximately 140 nm. As the number of pulses increases we see the period increasing with orientation

perpendicular to the polarization. As N increases further, the period increases again with the formation of LSFLs. **We infer from these results that nano bumps might be specific to small fluences and larger numbers of pulses since we do not see such structures at higher fluence and by varying the number of pulses.**

To conclude, an overview of different nanostructures obtained for various combinations of F_p and N is shown in figure 3.5. These nanostructures are a result of laser machining under ambient conditions. LSFLs, HSFLs, and nanobumps were obtained for fs laser irradiation in ambient conditions. Since our motive is to study the surface chemistry of nanostructures obtained for various gaseous conditions, we must explore whether these nanostructures are changing when machining under different laser processing environments.

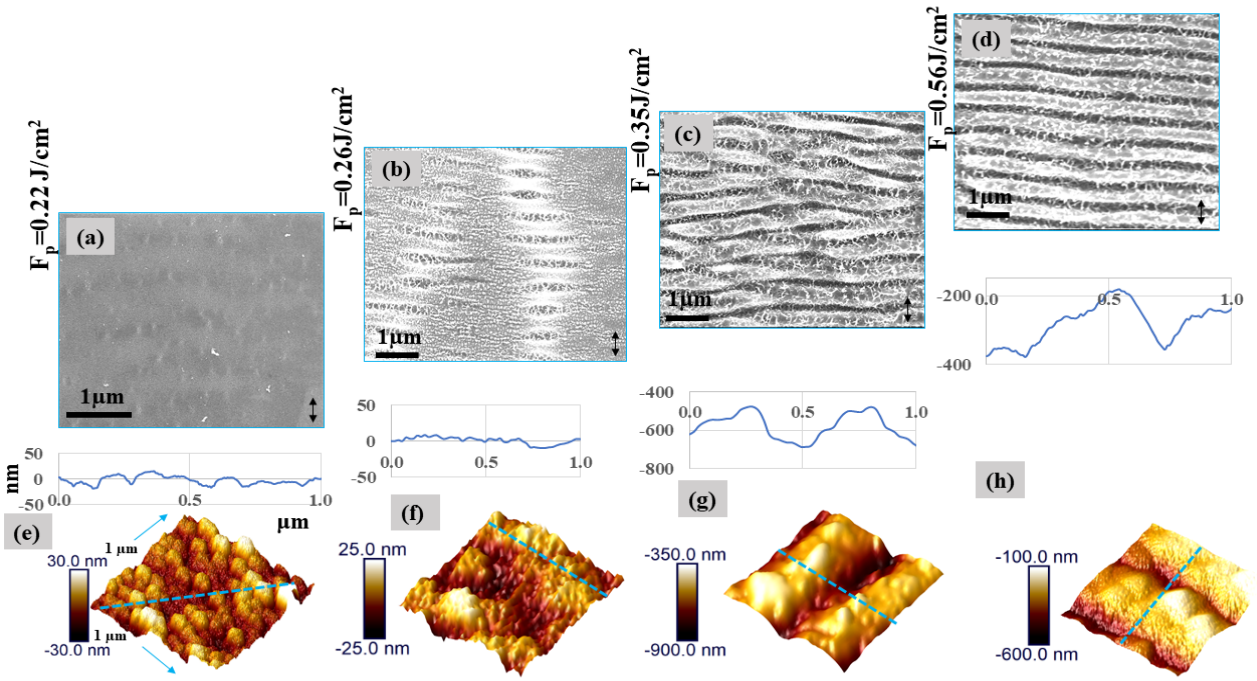

Figure 3.3: Evolution of nanostructures by increasing F_p and fixing N=200. (a) to (d): SEM images of nano-bumps (a), LSFLs covered in HSFLs (b), and LSFLs (c and d). (e) to (h): AFM images of nano-bumps (e), LSFLs covered in HSFLs (f), and LSFLs (g and h) along with their height profile taken along the blue line.

3.3 Nanostructures under different laser processing environments

Laser irradiations were performed in different gaseous conditions, specifically in **argon, nitrogen, and air at the same pressure i.e., at 10 mbar**. The primary pump was first used to go down to 10^{-2} $mbar$ and then gases were introduced in the chamber until a pressure of 10 mbars was reached. **The irradiations were repeated for ambient and high vacuum (10^{-7} $mbar$) environments**. Similar to previous sections, the evolution of nanostructures in the various laser texturing environments with respect to the Gaussian fluence distribution and for different combinations of peak fluence (F_p) and number of pulses (N) is given in the following sections.

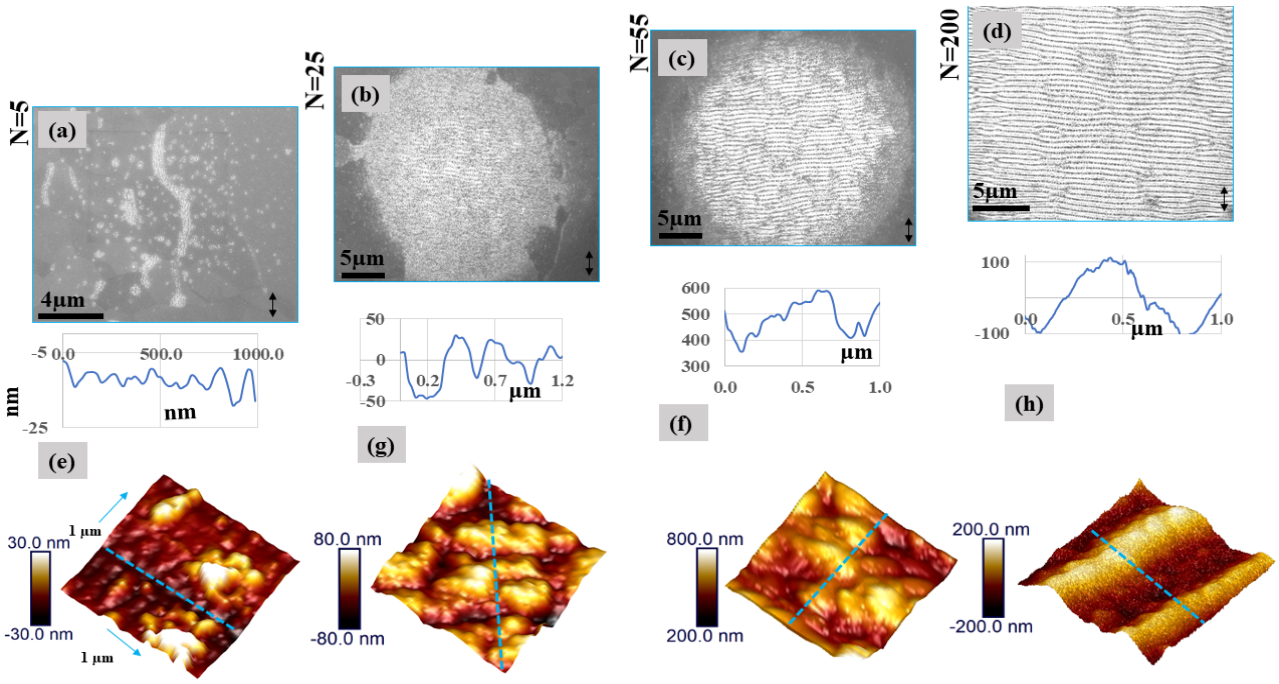

Figure 3.4: Evolution of nanostructures by fixing $F_p = 0.52\ J/cm^2$ and changing N. (a) to (d): SEM images of nano-bumps (a), LSFLs covered in HSFLs (b), and LSFLs (c and d). (e) to (h): AFM images of nano-bumps (e), LSFLs covered in HSFLs (f), and LSFLs (g and h) along with their height profile taken along the blue line.

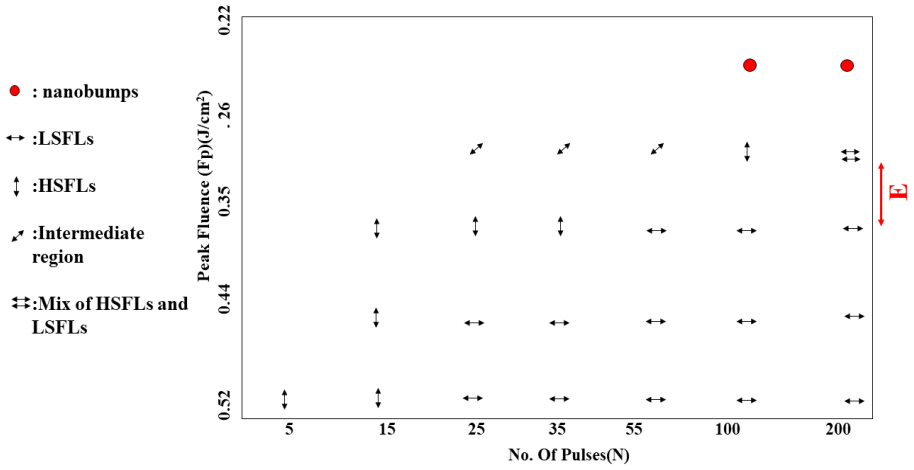

Figure 3.5: An overview of different structures formed for various combinations of F_p and N

3.3.1 Nanostructure Evolution-Gaussian Distribution of Fluence

Figure 3.6 a-e shows the evolution of nanostructures (SEM images) as a function of fluence along the Gaussian laser pulse for W samples irradiated in various environments, namely ambient, air 10 mbar, nitrogen 10 mbar, argon 10 mbar and vacuum 10^{-7} mbar at constant $Fp = 1.04\ J/cm^2$ and N=100. For ambient laser texturing, we see the evolution from nano bumps to HSFLs (perpendicular to the laser polarisation) to LSFLs (perpendicular to the laser polarization) going from the periphery to the center of the laser spot. For air 10 mbar, nitrogen 10 mbar, and argon 10 mbar we see the evolution from nano bumps to HSFLs (parallel to polarization) to LSFLs (perpendicular

to polarization) going from the periphery to the center of the laser spot. **Interestingly, for vacuum 10^{-7} mbar, we do not see nano bumps but instead HSFLs (parallel to polarization) and LSFLs (perpendicular to polarization)**.

3.3.2 Nanostructure Evolution-Combinations of fluence (F_p) and number of pulses (N)

The effect of laser peak fluence and the number of laser pulses on nanostructure formation is presented next. As shown in figure 3.7, ambient irradiation is similar to the observations and discussions in sections 3.2.2 and 3.2.3. As fluence increases nanostructures evolve from nano bumps to HSFLs to LSFLs. At the same 10 mbar pressure but for different gaseous conditions (in air, nitrogen, and argon) similar nanostructures are observed but with nano bumps appearing at lower fluence, and as the fluence increases HSFLs and LSFLs (with an ablated region with micro-roughness between HSFLs and LSFLs). As the number of pulses increases HSFLs transform to LSFLs as was the case in ambient conditions. **No nano bumps are formed for vacuum conditions**. This is shown in figure 3.7 (e) & 3.10 (e).

3.3.3 The interesting case of nano bumps: A small detour

It is evident from the experiments that nano bumps are ultrafast laser-induced nanostructures usually seen for a combination of a larger number of pulses and small peak fluences. They are formed under various gaseous environments, but not in vacuum conditions. In fact, nano bump on tungsten is not new, as it was observed for nanosecond laser irradiation on single crystalline tungsten at different wavelengths, 1064 nm and 532 nm, under inert gas atmosphere [197, 198]. They seem to be more uniform in height and period throughout the laser irradiated spot. Their reported height and diameter are 300 nm and 700 nm respectively as shown in figure 3.8 (d). Whereas the nano bumps we observe here by femtosecond laser irradiation have an average height and diameter of 20 nm and 50 nm respectively (figure 3.8 (a), (b), (c) and (e)). **But the major difference here, in addition to the fact that we used femtosecond laser, is that the literature only suggests the formation of nano bumps on the borders of laser irradiation whereas, our experiments show the nano bumps formation not only on the border together with LSFLs at the center of the spot but also at the center when irradiated with lower fluence**.

Several studies support the formation of nano bumps based on jet formation and droplet ejection mechanism induced by laser irradiation. In gold, it is formulated based on the collapse of laser-generated molten material similar to the collapse of cavitation bubbles at a liquid-air interface [199]. Generally, at lower fluences, nano bumps are attributed to laser-induced melting and resolidification. The laser-induced molten part detaches itself from the surface due to the compressive stresses coming from the thermal expansion induced by the laser. The rapid resolidification of this detached layer causes the nano bump formation [200]. However, in this literature [200], machining under 5 mbar pressure appears to have no effect on the nano bumps. But in our experiments, we observe no nano bumps for vacuum (10^{-7} mbar). This is an interesting aspect for further study. Moreover,

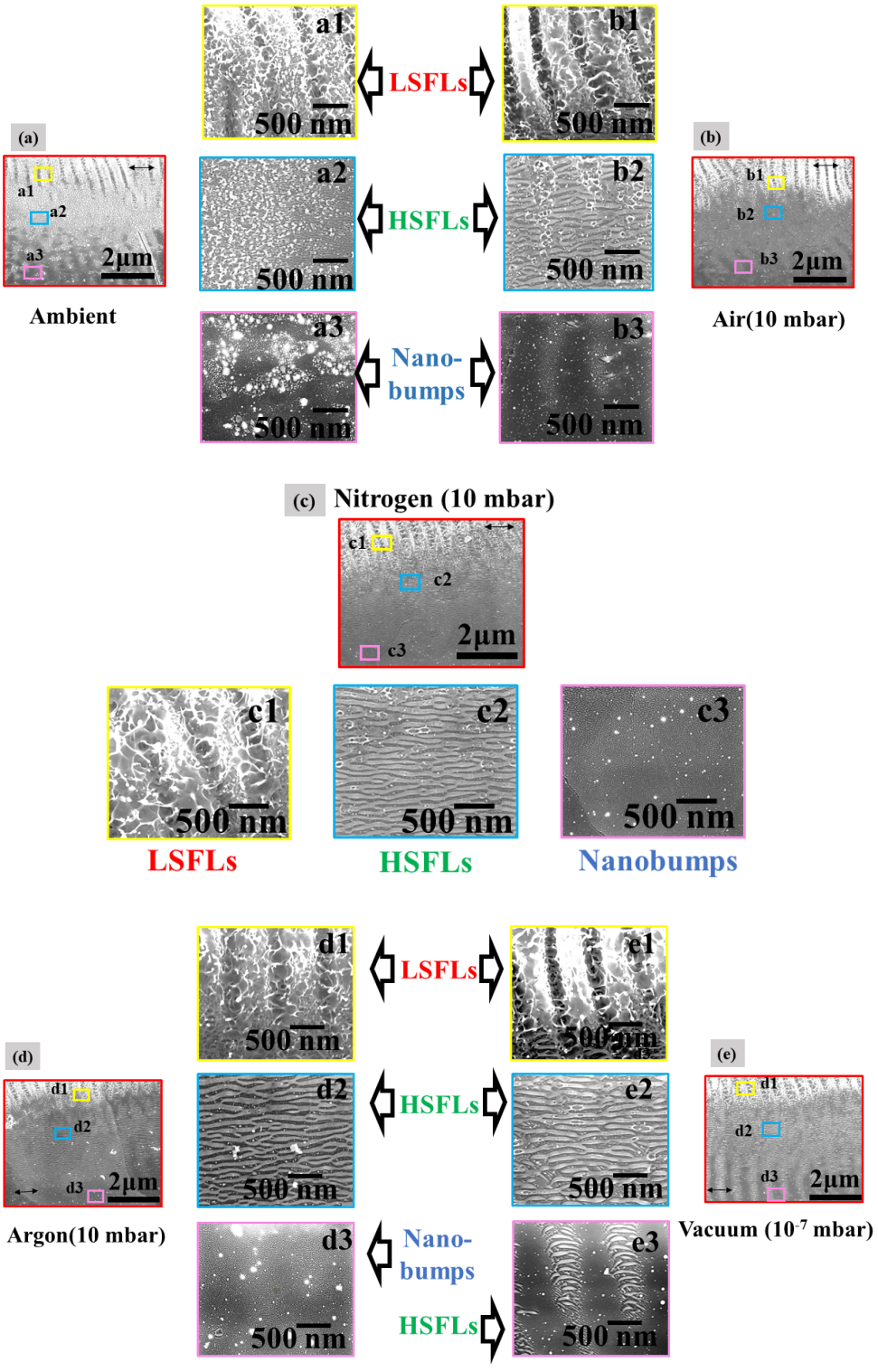

Figure 3.6: Nanostructures evolution of Gaussian fluence distribution for $Fp = 1.04\ J/cm^2$ and N = 100. (a) to (e): SEM images of nanostructures generated in ambient (a), air 10 mbar (b), nitrogen 10 mbar (c), argon 10 mbar (d) and vacuum $10^{-7} mbar$ (e) with zoomed-in images of LSFLs (a1,b1,c1,d1,e1), HSFLs (a2,b2,c2,d2,e2) and nano bumps (a3,b3,c3,e3) for each case.

nanopeaks of high aspect ratio and sub-100 nm periodicity were recently reported by Nakhoul et al. [201] on nickel

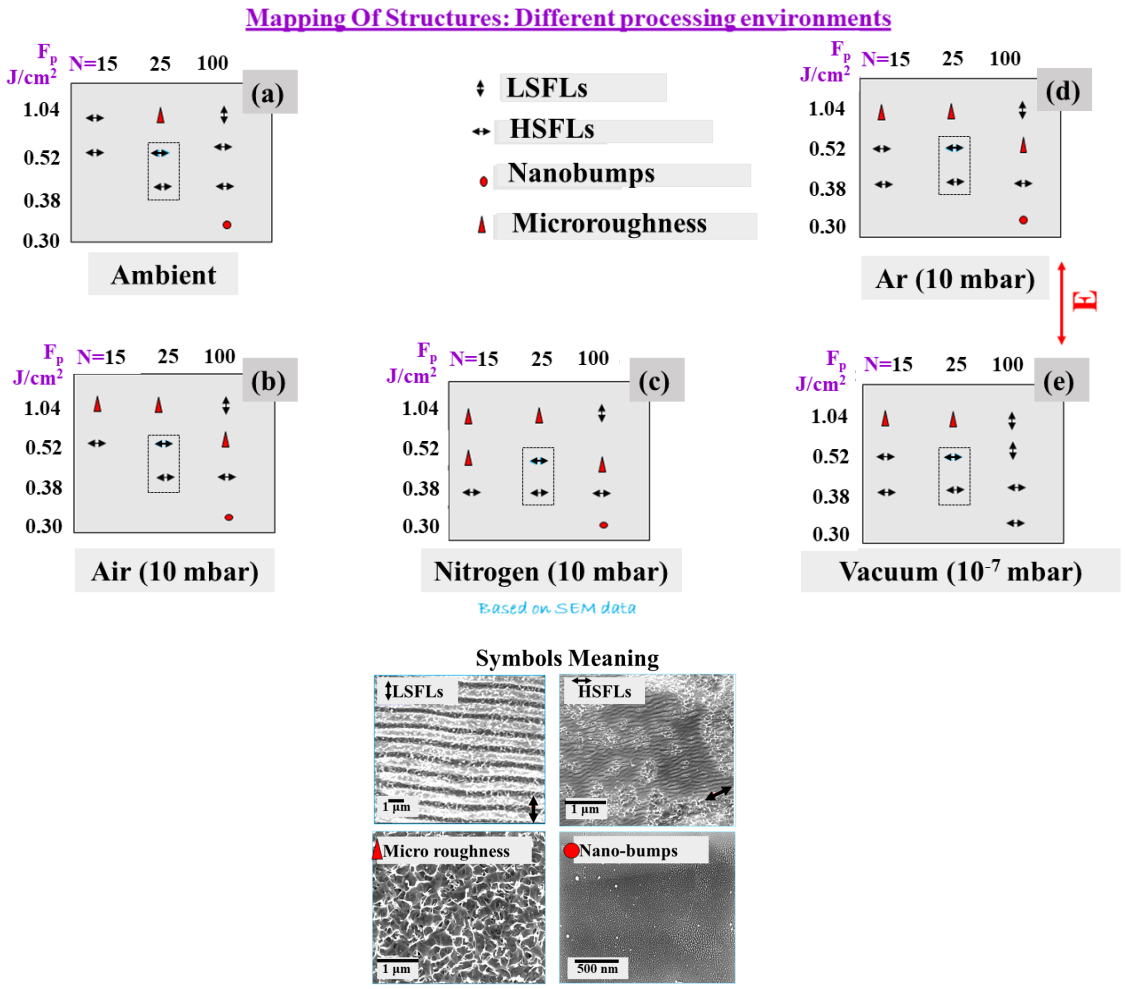

Figure 3.7: Nanostructures mapping for different Fp and N, based on SEM images for ambient (a), air 10 mbar (b), nitrogen 10 mbar (c), argon 10 mbar (d) and vacuum $10^{-7} mbar$ (e).

upon femtosecond laser irradiations. But this is due to the utilization of cross-polarised ultrafast laser irradiation resulting in the interplay between light coupling and hydrodynamic flow leading to their formation.

3.4 Oxidation: a precondition for nanostructure formation?

As discussed in the previous chapter, recent surface chemistry studies, especially laser-induced oxidation, have proposed that oxidation is a necessary condition for nanostructure formation. Here, we challenge this proposal by carrying out controlled laser irradiation experiments under various gaseous conditions.

If oxidation is to play a role in nanostructure formation, the sources of oxygen during laser irradiation need to be investigated. Oxygen can be incorporated from either one of the following sources (or both) during laser irradiation: (i) the native oxide layer, i.e., the adsorbed oxygen layer on the surface of materials here on tungsten (W) usually with a thickness of about 3 nm; (ii) the ambient air, which one might think is a major contributor.

Irradiations were also carried out in the presence of a reactive gas like nitrogen, inert gas like argon, and

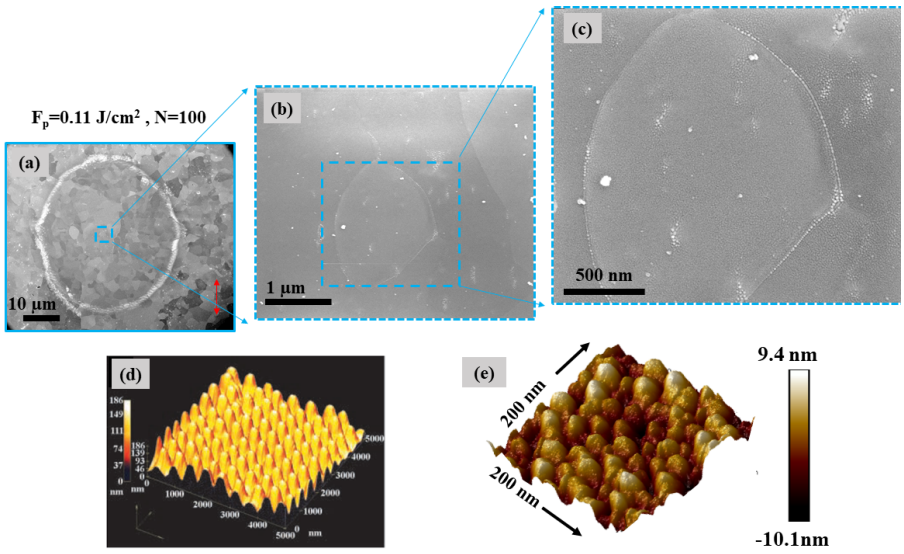

Figure 3.8: (a), (b) and (c): SEM images of nano bumps formed by laser irradiation in ambient conditions.(d) nano bumps formed on W by ns laser irradiation (Reprinted from "Self-assembled coherent array of ultra-fine particles on single-crystal tungsten substrate using SHG Nd: YAG laser" by Kawakami et al., 2000, Appl. Phys. A. Copyright (2000) by Appl. Phys. A. (2000) (e)AFM profile of nano bumps corresponding to the SEM images.

also in air at the same pressure (10 mbar). Irradiations were also performed in ambient conditions for comparison purposes. To avoid exposure to ambient oxygen, laser irradiation is performed in high vacuum conditions (10^{-7} $mbar$). While these experiments do eliminate the possibility of surrounding oxygen exposure, we still have to eliminate the native oxides on the surface. This is achieved with an in-situ sputtering apparatus, consisting of a plasma generator that produces a current = 0.25 A, frequency = 120 kHz, power = 16 W, and voltage = 26 V, to achieve the potential difference to create the plasma from argon gas at 10^{-2} $mbar$. After the sample is loaded in the vacuum chamber, it is sputtered with argon ions which will clean the W surface of any native oxide layer. The sample is sputtered for a time period of 3 minutes to ensure the elimination of the native oxide layer. The experiments are repeated in all five laser irradiation environment conditions. **This procedure ensures that no oxygen is present in the chamber prior to laser irradiation, neither from the native oxide layer nor from the ambient oxygen**.

The first experiments looked at whether oxidation takes place during ultrafast laser irradiation of W in the ambient environment. SEM-EDX analyses (figure 3.9) show that the weight percent of oxygen increases with an increase in fluence and the number of pulses. To decouple surface chemistry from surface morphology, the same surface morphology is used for all laser irradiation environments. **HSFLs is the nanostructure of choice since ultrafast laser irradiations in various gaseous conditions generated very similar HSFLs using the same set of laser parameters ($F_p = 0.35$ J/cm^2, and N=25) as shown in figure 3.10**. A laser wavelength $\lambda = 800$ nm, a repetition rate of 1 kHz, and a pulse duration of 60 fs were used for these experiments.

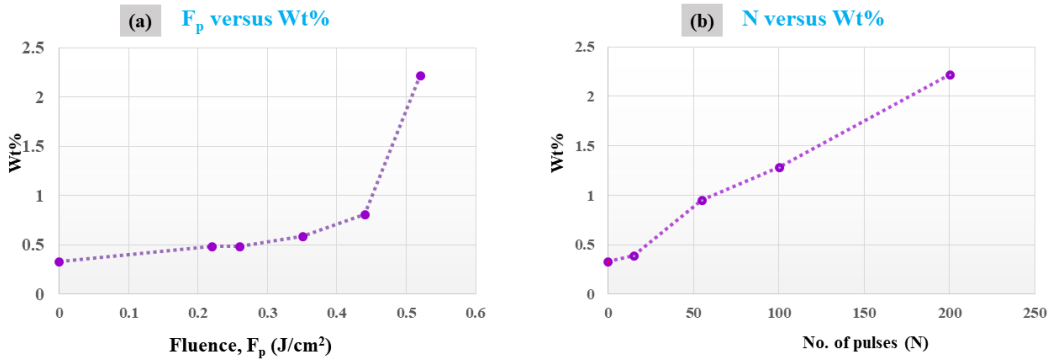

Figure 3.9: Variation of weight percentage (Wt %) of Oxygen (obtained with SEM-EDX) with peak fluence (F_p) (a) and number of pulses (N) (b).

3.4.1 HSFLs without sputtering

The HSFLs generated without sputtering are parallel to the direction of polarisation and have sub-100 nm periodicity and sub-20 nm amplitude as shown by the SEM and AFM profiles ($1\ \mu m \times 1 \mu m$ **area) in figure 3.10**. The obtained HSFL period (Λ) is 81 $\pm$ 2 nm, 92 $\pm$ 3 nm, 109 $\pm$ 3 nm, 95 $\pm$ 3 nm, and 123 $\pm$ 2 nm for ambient, air (10 mbar), N (10 mbar), Ar (10 mbar), and vacuum (10^{-7} *mbar*), respectively. This indicates that irrespective of the surrounding gas, HSFLs can be produced. This result suggests that **interaction with ambient oxygen is not necessary for HSFLs formation on W.**

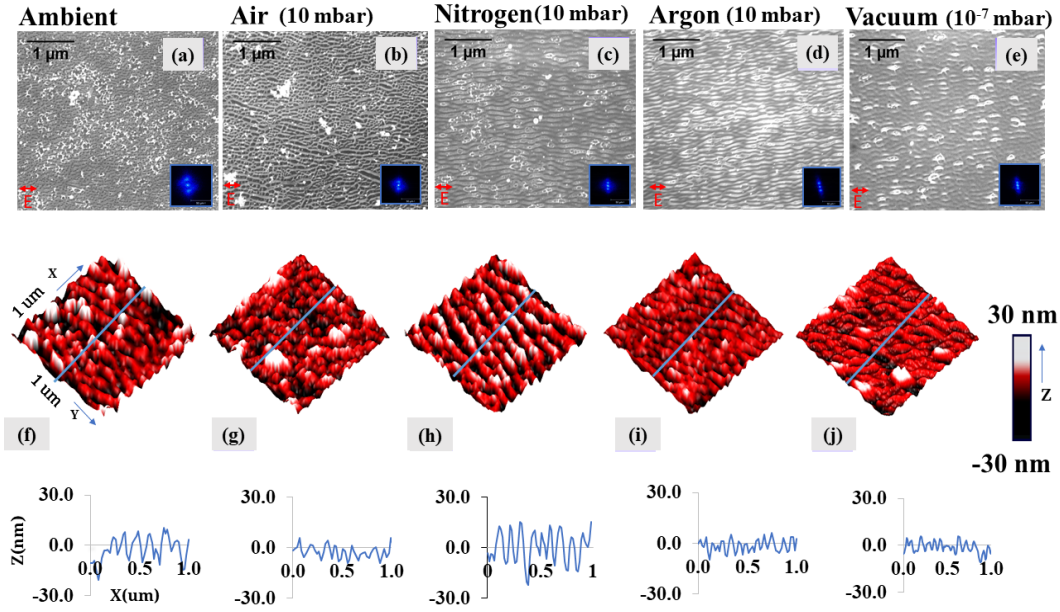

Figure 3.10: HSFLs generated at different laser irradiation environments without sputtering (a) to (e): SEM images with respective FFT images of HSFLs generated in ambient (a), air 10 mbar (b), nitrogen 10 mbar (c), argon 10 mbar (d) and vacuum 10^{-7} *mbar* AFM images and corresponding height profiles (corresponding to blue lines) of HSFLs generated in ambient (f), air 10 mbar (g), nitrogen 10 mbar (h), argon 10 mbar (i) and vacuum 10^{-7} *mbar* (j).

3.4.2 HSFLs with sputtering

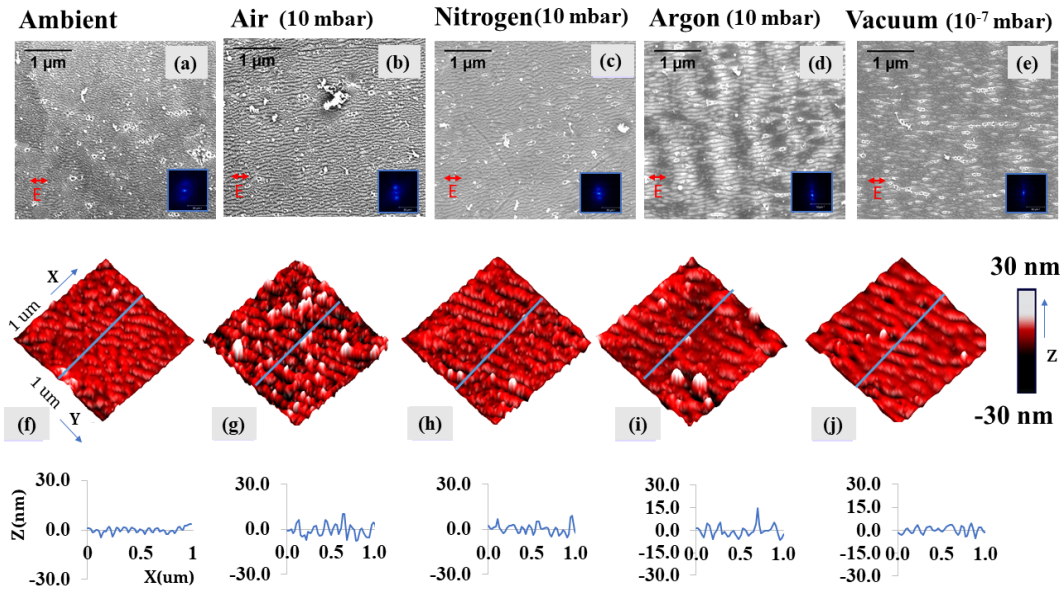

Figure 3.11: HSFLs generated at different laser irradiation environments with sputtering (a) to (e): SEM images with respective FFT images of HSFLs generated in ambient (a), air 10 mbar (b), nitrogen 10 mbar (c), argon 10 mbar (d) and vacuum $10^{-7}mbar$ AFM images ($1\mu m \times 1\mu m$ area) and corresponding height profiles (of the regions marked in the blue line in AFM images) of HSFLs generated in ambient (f), air 10 mbar (g), nitrogen 10 mbar (h), argon 10 mbar (i) and vacuum $10^{-7}mbar$ (j).

The HSFLs generated with sputtering are parallel to the direction of polarisation and have sub-100 nm periodicity and sub-20 nm amplitude as shown by the SEM and AFM profiles in figure 3.11. The HSFL period (Λ) is 51±4 nm, 72±5 nm, 79±3 nm, 88±4 nm, 152±5 nm for ambient, air (10 mbar), N (10 mbar), Ar (10 mbar), and vacuum (10^{-7} $mbar$), respectively. This indicates that irrespective of the surrounding gases and in the absence of a native oxide layer and no interaction from ambient oxygen, HSFLs can also be produced. One can conclude that **interaction with ambient oxygen and native oxide is not a precondition for HSFLs formation on W.** If ultrafast laser-induced HSFLs on W do not have an oxidation-based origin, another process is responsible as discussed below.

3.5 Influence of pressure: Hydrodynamic origin of HSFLs

The variation in the HSFLs period and amplitude with different processing atmospheres, with and without sputtering, is shown in figure 3.12. **The generally observed trend, with and without sputtering, is that the HSFLs period increases as the pressure decreases**. As the ambient air was controlled to a pressure of 10 mbar (i.e., the condition of 10 mbar of air), the period increased compared with that of atmospheric pressure, and it further continued to increase as the pressure was reduced to as low as 10^{-7} $mbar$ (under vacuum). **The decrease in ambient pressure can affect the hydro-dynamical aspects of laser-matter interaction by influencing the surface tension of the molten liquid, thus leading to an increase in the period, as observed experimentally**. Rather than originating from SEWs (Scattered Electromagnetic Waves) in the laser-induced oxide

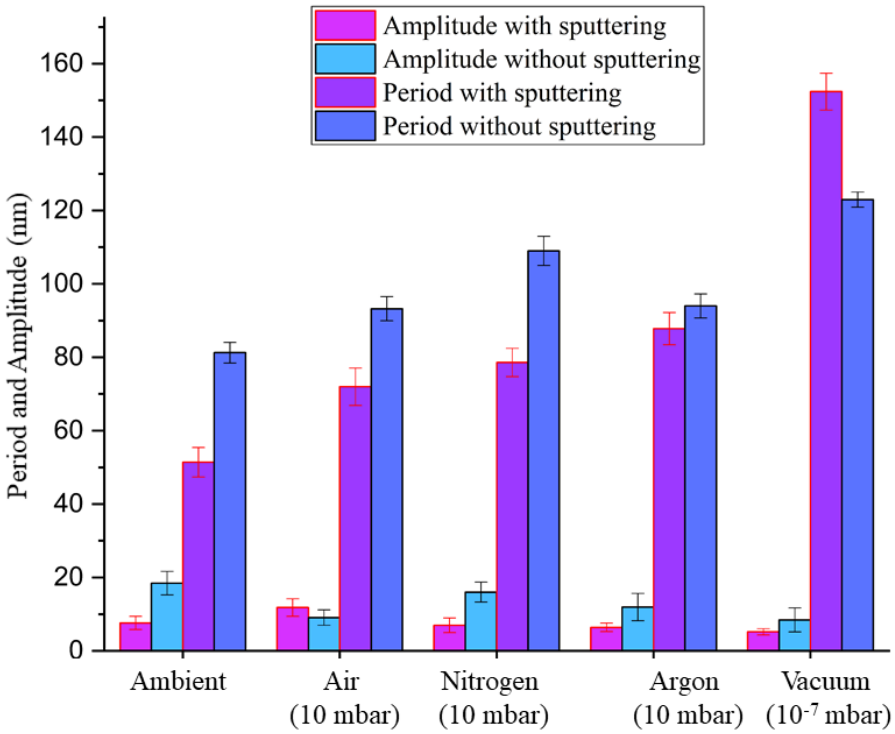

Figure 3.12: Variation in the period and amplitude of the HSFLs formed under different processing environments with the error bars showing the variation of the period and amplitude over 6 areas for each of the samples.

layer, we propose that HSFLs are formed by molten material reorganization, driven by surface-tension-dependent transverse Marangoni gradient process [95]. The observed periodicity of the HSFLs (Λ) is related to the Marangoni instability as [202, 187],

$$\Lambda = 2\pi L/\sqrt{(M_a/8)} \tag{3.1}$$

where L is the liquid layer thickness, and M_a is a dimensionless quantity called the Marangoni number, as given by [202, 187],

$$M_a = -\frac{d\gamma}{dT}\frac{L\Delta T}{\mu D}, \tag{3.2}$$

where $\frac{d\gamma}{dT}$ is the temperature-dependent surface tension gradient, ΔT is the temperature difference, μ is the viscosity, and D is the thermal diffusivity. The dependence of the surface tension gradient on pressure (P) is given by [203],

$$\frac{d\gamma}{dT} \propto -P \tag{3.3}$$

From these equations, **we obtain the HSFL period,**

$$\Lambda \propto P^{-1/2} \tag{3.4}$$

This equation agrees with our experimental observations where smaller HSFL periods are observed at higher pressures and supports a molten material reorganization process.

The small HSFL period of approximately $\Lambda \sim \lambda/8$ can also be correlated to the confinement of the light absorption, as Marangoni instability provides $\Lambda \propto \sqrt{L}$, where L is the liquid layer depth. Assuming that at this low fluence and high electron–phonon coupling strength, the electron thermal energy diffusion is weak, the energy confinement can roughly be estimated by the optical penetration depth for tungsten at 800 nm. This is given by,

$$\lambda/4\pi k = 25\ nm, \tag{3.5}$$

where k = 2.9 is the extinction coefficient for photo-excited W [204]. For this small penetration depth, a small liquid layer, and thus a small HSFL period, is expected.

The sputtering prior to laser irradiation induces small changes in the structures' periodicity, as shown in figure 3.10 and figure 3.11. This may be due to the change in roughness on the tungsten target induced by the sputtering process. It is known that the initial roughness can highly influence laser coupling and hence the resulting topography [205]. In particular, the concentration of nano reliefs such as bumps and cavities resulting from the sputtering process affects the final period. It is expected that the introduction of additional scattering inhomogeneities on the surface with an average distance lower than the initial roughness would result in a higher concentration of scattering centers. This favors dipole–dipole coupling for nonradioactive fields, reducing the pattern period [204]. Topographical features in the SEM (figure 3.10 and figure 3.11), for different gaseous atmospheres, are different arising from the polycrystallinity of the samples. Because of the variation in energy absorption, phase transition, and lattice defects storage for different crystal orientations, their interaction with the laser beam can be different [206]. Because of the lower fluence used for the generation of HSFLs, these changes can be more intense.

All observations in this work signal that the formation of HSFLs for a given fluence and number of pulses under different laser processing atmospheres is mostly independent of any supply of oxygen. **These results strongly suggest that HSFLs are more likely to be explained by theories based on electromagnetics coupling with hydro-dynamical concepts of laser-matter rather than the propagation modes implying oxidation models**. More specifically, inhomogeneous subsurface energy absorption arising from the local non-radiative electromagnetic response can trigger nano-convective instabilities. These thermoconvective instabilities mediated by temperature-gradient-dependent flow of capillary waves and their further solidification-producing nanostructures [202, 187, 207] can explain the HSFL formation observed in the absence of oxygen and the decrease in HSFLs period with ambient pressure.

Now, in order to better understand the surface chemistry of various HSFLs we performed cross-sectional TEM images which revealed the formation of subsurface cavities, as detailed below. Even though sub-surface cavitation is not our main topic of interest of this thesis, we decided to explore it in more detail since it will provide precise answers on the formation mechanism of HSFLs giving more clarity on the influence of pressure and surface tension.

3.6 Subsurface cavitation

3.6.1 Subsurface Topography

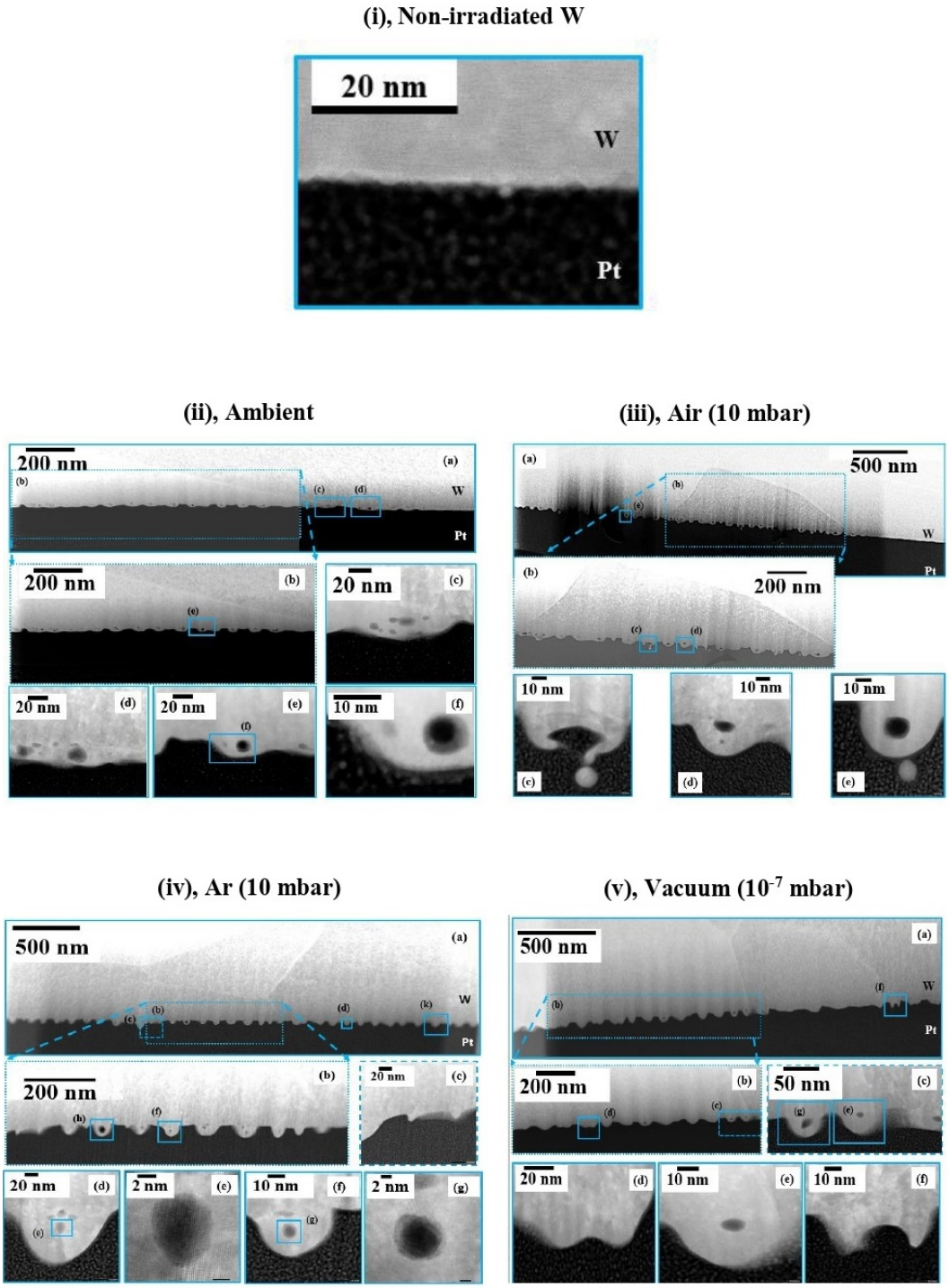

Figure 3.13: STEM cross-sectional images of, (i) non-irradiated tungsten, ((ii), a to f) HSFLs obtained at ambient (with sputtering), ((iii), a to e) HSFLs obtained at air 10 mbar with different views on the subsurface voids without sputtering, ((iv), a to g) HSFLs obtained at Ar 10 mbar with different views on the subsurface voids without sputtering, ((v), a to f) HSFLs obtained at vacuum $10^{-7} mbar$ with different views on the subsurface voids without sputtering: bursted, with voids absents and multiple voids.

Thin lamellae were prepared from regions of HSFLs generated in ambient (with sputtering), air at 10 mbar (without sputtering), argon at 10 mbar (without sputtering), vacuum at $10^{-7} mbar$ (without sputtering) and non-irradiated W, and analyzed under STEM. Analysis of these images reveals the formation of nanovoids below the crests of HSFLs in all four cases except for the non-irradiated W (figure 3.13 (i)), indicating they are a result of laser-matter interaction. The presence of these nanovoids in all these environments also confirms the hydrodynamic-based HSFL formation mechanism. Subsurface voids were seen significantly throughout the 3 μm length of the thin lamellae, even for different grain orientations. Some burst voids like in (figure 3.13 (iii) (c), figure 3.13 (v), (f) are also observed along with closed ones as seen in (figure 3.13 (ii) (d)-(f), figure 3.13 (iii) (d) & (e), figure 3.13 (iv) (d)-(g), 3.13 (v) (e), and in some crests, multiple voids (figure 3.13 (ii) (d)-(f), figure 3.13 (iii) (d), figure 3.13 (iv) (d) & (f)) can be seen. In general, voids are distributed within HSFL bumps, whether they were formed with or without sputtering, and have diameters varying from 5 nm to 15 nm.

Images in figure 3.13, depict how the distribution and size of subsurface voids vary for ambient, air at 10 mbar, argon at 10 mbar, vacuum at 10^{-7} mbar. They are as follows: for ambient HSFLs, the voids appear mostly 13 nm below the surface (measured from the center of the void) and have an average diameter of 11 nm (averaged over 7 voids with a standard deviation of 4.5 nm). In the case of air at 10 mbar pressure, the voids appear mostly 20 nm below the surface (measured from the center of the void) and have an average diameter of 11 nm (averaged over 7 voids with a standard deviation of 5.5 nm). For argon at 10 mbar pressure, the voids appear mostly 18 nm below the surface (measured from the center of the void) and have an average diameter of 8 nm (averaged over 7 voids with a standard deviation of 5.5 nm). Finally, for vacuum HSFLs, the voids appear mostly 18 nm below the surface and have an average diameter of 12 nm (averaged over 7 voids with a standard deviation of 3 nm). This is represented in Table 3.1.

Irradiation conditions	Depth	Diameter
Ambient	13 nm	11 ± 4.5 nm
Air (10 mbar)	20 nm	11 ± 5.5 nm
Argon (10 mbar)	18 nm	8 ± 5.5 nm
Vacuum (10^{-7} mbar)	18 nm	12 ± 3 nm

Table 3.1: Tabular representation of the depth at which the cavitations are seen along with the diameter of the cavities

Furthermore, we see that the number of voids for the same length of lamellae (over 800 nm) is smaller for vacuum conditions compared to lamellae obtained for other conditions. We observe evolution of void distribution density over 800 nm length of the lamellae with above 20 for ambient (figure 3.13 (ii) (b)), between 15 and 20 for air 10 mbar (figure 3.13 (iii) (b)), around 15 for Ar 10 mbar (figure 3.13 (iv) (b)) and 3 for vacuum lamellae (v) (figure 3.13 (b)). This could also arise from the slight difference in the period as the pressure changes as we already discussed in figure 3.12. Another possibility is that the surface topography generated by laser irradiation is highly specific to crystal orientation [206], and hence influencing the sub-surface behavior.

In order to better understand the surface chemistry resulting from laser irradiation, EDX, and EELS analysis was carried out.

3.6.2 Surface Chemistry: STEM EDX, STEM EELS

Figure 3.14 shows the STEM-EDX and STEM-EELS analyses with corresponding STEM images for HSFLs obtained with and without sputtering to analyze the surface chemistry of various HSFLs obtained in different conditions. In figure 3.14 (e), (f), (g), (h), (p), (q) & (r) a clear green boundary representing a high concentration of oxygen between the platinum protective layer and W can be observed for all cases, that is for non-irradiated W, ambient, air 10 mbar, argon 10 mbar and vacuum (cases involving with and without sputtering). The same results were obtained from STEM-EELS analyses (figure 3.14 (i)-(l), (p)-(r)). It should be noted that we do see a fine layer of oxygen on vacuum HSFLs since the lamellae were exposed to air between the time of laser irradiation and STEM-EDX/EELS analyses (figure 3.15 (h) & (l), (r) & (u)). An oxide layer is also lining the subsurface voids, but it is unclear whether this is a result of air exposure prior to TEM analysis or due to the laser irradiation process. The oxide layer for vacuum and argon conditions does not seem to be as strong as that for non-irradiated W and air 10 mbar.

In figure 3.14, even after sputtering, **we see the presence of oxide for ambient and air 10 mbar, but not a strong presence for vacuum** (the O distribution appears more like noise).

Another interesting question to address is whether the surface chemistry is grain orientation-dependent. To analyze this closely, we compared two-grain orientations for HSFLs obtained at 10 mbar, and the EELS mapping of the crests and troughs associated with HSFLs for both grains are shown in figure 3.15. We see that **the surface chemistry seems to be the same for both grain orientations**.

Even though we were not able to obtain more interesting results based on surface chemistry using these techniques, the analysis on sub-surface voids as seen below re-affirms our hypothesis on a hydrodynamics-based origin of HSFLs rather than an oxidation-based model as can be seen from the following section.

3.6.3 Formation of Subsurface Voids

The observation of subsurface voids on metals was reported earlier, but not associated with HSFLs on W. There have been reports of subsurface voids of a few hundred nm in size as observed by STEM cross-sectional images of laser irradiated Al target (under vacuum) giving rise to micro bumps [208]. Subsurface voids are seen to be associated with periodic structures in Ni [209]. These periodic structures are a result of the interference of near-field scattered waves or superposition of far-field scattered waves (nf_{ll} and $ff_{\perp}$ respectively), with an incident laser beam. STEM images of subsurface voids (tens of nm in size), associated with nf_{ll} and $ff_{\perp}$ crests were revealed in this case. In our work we are reporting sub-surface voids of a few nm in size associated with HSFLs on W, observed for four different processing conditions (ambient, air (10 mbar), Ar (10 mbar), and vacuum (10^{-7} mbar)) with the same laser parameters.

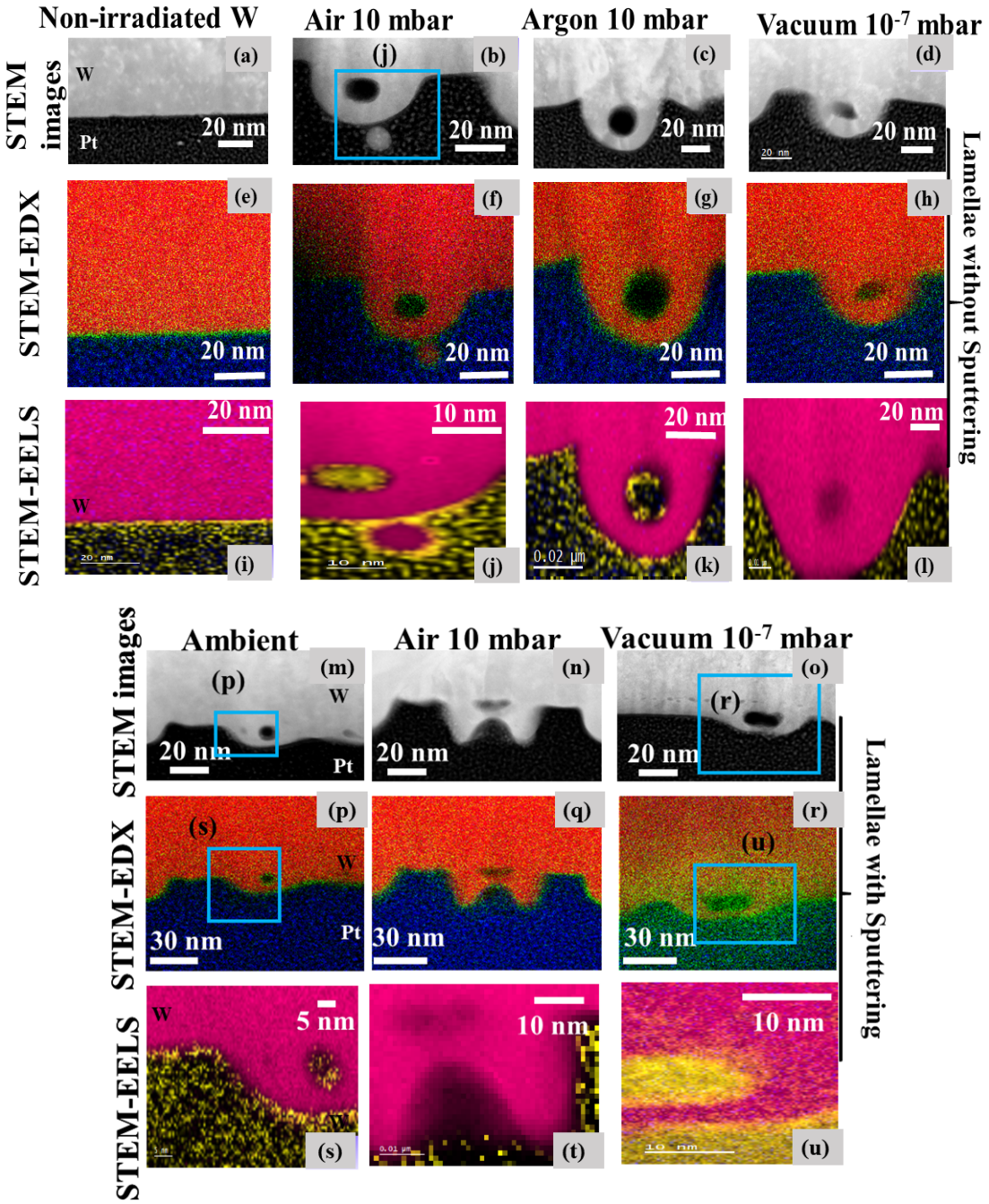

Figure 3.14: STEM images (a-d, m-n), STEM-EELS (i-l, s-u) and STEM EDX (e-h, p-r) analysis of non-irradiated W (without sputtering), air at 10 mbar pressure (with and without sputtering), argon at 10 mbar pressure (without sputtering) and vacuum HSFLs (with and without sputtering). The color code for EDX mapping is orange - W; Blue - Pt; Green - O; for EELS mapping Pink-W; Yellow - O.

While the STEM images of frozen subsurface voids in metals are limited in the literature, the mechanism behind their formation is widely studied using TTM-MD. For example, in Ag, under vacuum conditions, the surface swelling due to fs laser irradiation seen at very small fluences and without significant ablation, is attributed to subsurface cavitation as confirmed by TTM-MD simulations [46]. In the fluence regime below the spallation threshold, TTM-MD suggests that subsurface voids are the reason for surface swelling of Al irradiated in air [45].

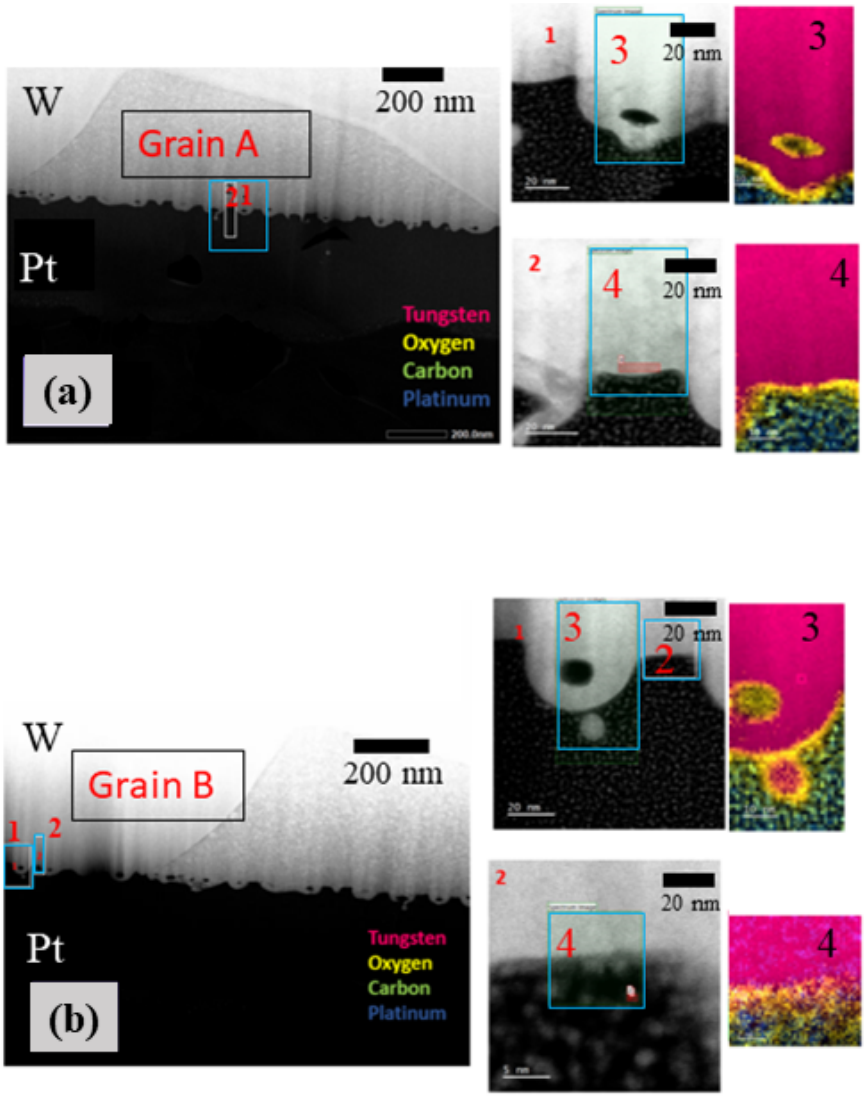

Figure 3.15: (a) and (b) correspond to STEM images of grain A and grain B of the same lamella (air 10 mbar) with regions 1 and 2 for both the images being the zoom for the crest and trough of the HSFLs. Both 3 and 4 in (a) and (b) correspond to the oxide layer formed on the top of HSFLs and it shows no major visible difference for different grains.

In all cases, the reason for subsurface void formation is the same - they are seen in the pre-spallation regime, where the rarefaction wave (resulting from material relaxation) that develops in the laser-induced melt and travels to the surface of the target causing the nucleation of the subsurface voids [202, 209, 46, 57, 210, 41]. Due to the fast cooling (10^{12} K/s for metals [211]) and solidification, these voids can be frozen under the surface of the material. The origin of these sub-surface voids is usually associated with mater reorganization theories or hydrodynamics principles. To better understand subsurface voids observed in W associated with HSFLs, TTM-MD simulations were carried out.

3.6.4 TTM-MD study on the generation of voids

The following TTM-MD simulations were performed by Dr.Djafar Iabbaden in our group to support the experimental findings.

A hybrid simulation coupling two temperature models with a Molecular dynamics simulation (TTM-MD) scheme implemented in LAMMPS [212, 213, 214, 215, 216, 217, 218, 219] was used to model ultrafast laser interaction inducing voids formation within a tungsten target (W). For this purpose, a perfect initial BCC (Body-centered cubic) W sample with dimensions $l_x \times l_y \times l_z$ of $314 \times 18.2 \times 18.2\ nm^3$ containing 6728000 atoms within a box having periodic boundary conditions on x, y, and z is shown in figure 3.16. A structural minimization of the sample was first performed using a force norm criterion of $10^{-6}\ eV/$ Å. Then, this structure was heated from 0 K to 300 K for 15 ps using the Nose-Hoover thermostat-barostat style (NPT ensemble). In the present simulations, an embedded atom method (EAM) inter-atomic potential developed in [220] and an integrating time step of 1 fs were utilized for both the sample preparation and the void formation. The TTM-MD scheme was solved on a $702 \times 1 \times 1$ electronic mesh, that was applied to the previous configuration (relaxed and thermalized) during 12 ps with W electronic properties input parameters that can be found in [212, 204, 221]. The lateral dimensions l_y and l_z were subjected to periodic boundary conditions. However, following the x-direction a free boundary condition was created since the laser is applied in the same crystallographic direction. Moreover, to avoid pressure wave reflection a non-reflecting boundary conditions (NRBC) with a damping factor γ_{damp} =2 $\times 10^{-4}\ eV$ ps Å^{-2} and dimension of L_{NRBC} = 63.3 nm following x was designed at the rear of the target. [222, 223]. The laser-mater simulations were performed by employing experimental laser operating conditions of τ = 60 fs pulse duration and peak fluence = 0.35 J/cm^2. Finally, the sample was subjected to a regular MD (Molecular Dynamics) in the micro-canonical ensemble (NVE) for 68 ps. The local atomic structure is investigated using the Polyhedral Template Matching Algorithm (PTM) [224] implemented in the OVITO software [225].

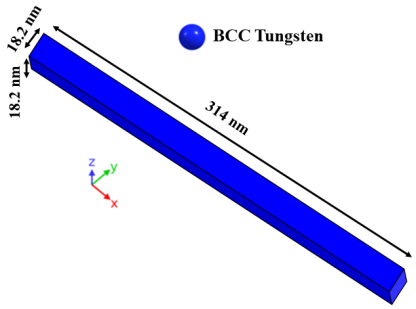

Figure 3.16: Initial sample geometry used to model ultrafast laser pulse interaction with tungsten target by employing TTM-MD simulations. In blue are BCC crystalline structures located inside the rectangular box. The rear region of the sample represents the NRBC zone.

3.6.5 Pressure map and Temperature map

The complex void formation processes in W were investigated, and the results are shown in figure 3.17 (a). Two stages of void evolution are observed. The first one is in the time range of 0-40 ps where the ephemeral apparition of voids in almost a spherical shape at t = 10 ps, grows and collapses with a bubble lifetime of 3-10 ps. Therefore, no bubbles survive inside the target. However, during the second stage from 40-80 ps, voids appear and coalesce to form larger voids. As shown at t = 80 ps, these small bubble accumulations give voids with different volumes. Additionally, they are located 25 nm under the surface.

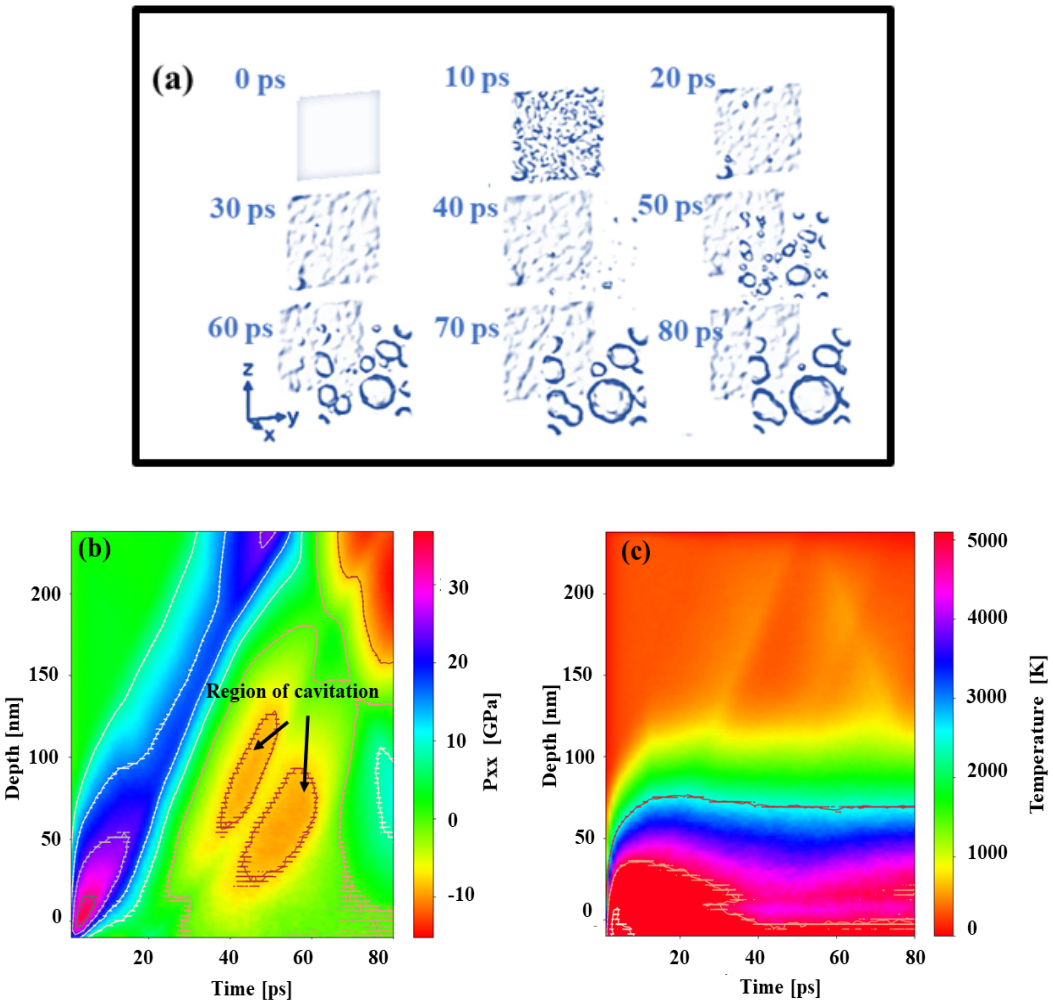

Figure 3.17: (a): Snapshots of the voids evolution at several times : 0 ps, 10 ps, 20 ps, 30 ps, 40 ps, 50 ps, 60 ps, 70 ps, and 80 ps in W target during ultrafast laser irradiation of $\tau = 60$ fs pulse duration and $F_{incident} = 0.35\ J/cm^2$ incident fluence. The surface meshing is constructed by the method as described and implemented in [226]. (b): Spatiotemporal evolution of pressure following the x-direction in the W target during the formation of the voids. (c): Spatiotemporal evolution of temperature in the target during the formation of the voids.

To understand the thermodynamics permitting the emergence of such voids within the W sample, pressure and temperature profiles were established as shown in figure 3.17 (b) and (c). The observation of Fig 3.17 (b) reveals that the target experiences a strong compressive pressure wave with a peak value of ~ 30 GPa after energy deposition at t = 1 ps and this pressure decreases until reaching a value of ~ 3 GPa at t ~ 40 ps. The results provide evidence that a rarefaction wave appears at a key time of t ~ 40 ps with a value of t ~ -10 GPa as shown in figure 3.17 (b) by arrow marks. This analysis provides strong evidence of the role of rarefaction wave in permitting the emergence and coalescence of voids in the irradiated surface region of W. Figure 3.17 (c) suggests that the surface is completely melted with a maximum value of ~ 5000 K which decreases deeper inside the material. Also, in the time range between 40-80 ps when voids appear, the contour shows that in this region the temperature decreases to a value of ~ 4000 K. This means that this cavitation process mainly takes place in the molten state. In addition, these simulations are consistent with the experimental results. Thus, the void formation

mechanism is identified as a combination of two criteria, a fast liquefaction of the surface with a rarefaction wave whereby voids are formed. **In other words, for the set of laser parameters used here, subsurface voids are formed while W is in a molten state, which confirms the hydrodynamics-based origin for HSFLs on W.** This helps us establish the origin of femtosecond laser-induced sub-surface cavitation on W associated with HSFLs based on rarefaction waves generated in the fast liquefied molten W, which was later solidified below the crests of HSFLs due to fast resolidification.

In our previous work [29], we noticed a trend of increasing HSFL period with decreasing atmospheric pressure, which can be related to the hydrodynamics-based surface tension-dependent transverse Marangoni gradient process. Therefore, the mechanism underlying the formation of HSFLs can be attributed to the interplay between sub-surface cavitation and Marangoni instability. The acoustic relaxation of the irradiated target induces hydrodynamic motion within the molten material, thereby playing a crucial role in the formation and elevation of the resulting structure [227]. In addition, it has already been established for Ni with the help of simulations coupling electromagnetics and hydrodynamics that the rarefaction wave destabilizes the laser-melted nanolayer resulting in Marangoni instability and hence the formation of HSFLs with very small periods and amplitude [202], similar to our case of sub-100 nm period and sub-20 nm amplitude HSFLs on W.

In summary, **under fs laser irradiation W undergoes melting (few tens of nanometers) and is under high compressive stresses, which is followed by a rarefaction wave, causing subsurface cavitation. This destabilizes the molten nanolayer (since this rarefaction wave is directed towards the temperature gradient) giving rise to Rayleigh-Bénard-Marangoni instability, redistributing the material from hotter regions (valleys of HSFL) to colder regions (crest of HSFL).** The orientation of the HSFLs on W, which are parallel to the direction of light polarization can be explained by the direction of the fluid flow (created by Marangoni instability) from hot spots located around subsurface voids, which usually results in an orientation parallel to the laser polarization [70]. Moreover, from the STEM images, it is evident that the formation of HSFLs as a result of Rayleigh-Bénard-Marangoni instability due to fs laser-induced rarefaction wave should be applicable for all four different laser irradiation conditions (ambient, air at 10 mbar, argon at 10 mbar and vacuum at 10^{-7} $mbar$) irrespective of the gaseous/pressure environments and hence mostly depends upon the laser irradiation parameters.

To conclude, this chapter presents the LSFLs, HSFLs, and nanobumps formed for various combinations of laser parameters and laser processing environments on the surface of tungsten by femtosecond laser irradiations. It focuses on the formation mechanisms of HSFLs on W with sub-100 nm periodicity and sub-20 nm amplitude. By using an experimental approach we are confirming the insignificance of oxidation during HSFL formation on W, with a possible hydrodynamic origin as indicated by the pressure dependence of the HSFLs period. This is then confirmed by the TTM-MD numerical method, which reveals that the subsurface cavitation as obtained by STEM images, is formed by the resolidification of laser-induced W melt, hence invalidating an oxidation-based approach and reaffirming a hydrodynamics-based thermocapillary model (Rayleigh-Bénard-Marangoni instability induced by laser-induced rarefaction wave). Even though subsurface topography and the formation mechanism of

HSFLs were not our main topic, the investigations on the original question- is oxidation a precondition for HSFL formation? lead us to dive deeper into the hydrodynamics-based formation of nanostructures and the mentioned findings. Now, our interest will be in establishing an oxidation mechanism associated with the formation of HSFLs on tungsten.

* * *

Chapter 4

Establishing Ultrafast Laser-assisted Oxidation Mechanism for HSFLs on Tungsten

"Knowing the oxidation mechanisms is crucial because this understanding provides routes to control oxidation and the final oxide quality."

-A.M. Stoneham, in Encyclopedia of Materials: Science and Technology, 2001

Although, the previous chapter concluded that laser-assisted oxidation on tungsten is not necessary for the formation of HSFLs there is a need to investigate the mechanism of this oxidation. Hence, in this fourth chapter, we explore the oxidation mechanism accompanying femtosecond laser irradiation on Tungsten and giving rise to tungsten oxides associated with HSFLs. Irradiations are carried out to obtain large-area HSFLs under ambient and vacuum conditions. Wettability measurements together with XPS analyses give new insights into the laser-generated oxides and oxides accumulated over time due to ambient exposure. The results are then used to derive an oxidation mechanism based on the diffusion of oxygen on W and pulse accumulation by extracting the exact temperature gradients and time using TTM-MD simulations.

4.1 HSFLs generated in ambient and vacuum environments

All irradiation experiments were performed on poly-crystalline tungsten samples (Good fellow, SARL) electrochemically polished down to an average roughness $Ra \sim 6\ nm$ measured with an Atomic Force Microscope (AFM). A Linearly polarized Yb: KGW laser (PHAROS from Light Conversion, Inc) with a center wavelength (λ) of 1030 nm, pulse duration (t) of 300 fs, and repetition rate (f) of 1 KHz is focused onto the W sample placed below a galvanometric scanner (AEROTECH AGV-10HPO) mounted on nano-positioning lift stage (AEROTECH ANT130-L-ZS).

A 5 $mm \times 5\ mm$ area was irradiated by raster scanning the laser beam of frequency f = 1 kHz, with a scanning velocity (v) of 4 mm/s and a line spacing (distance between two consecutive lines in X and Y directions while raster scanning) of 4 μm. The laser spot diameter (D) was measured to be 20 μm at the focus for a lens with a focal length of 48 mm. This corresponds to a pulse overlap ratio (OL) on a line drawn by the laser as [228],

$$[1 - v(fD)^{-1}]100\%, \tag{4.1}$$

i.e,

$$[1 - ((4mm/s)((1kHz)(20\mu m))^{-1}]100\%, \tag{4.2}$$

i.e., 80 % overlap with the parameters used here for the line. The peak laser fluence (F_p= (2×laser energy)/laser spot area) used for the experiments is 0.32 J/cm^2. Distance between lines,

$$d_p = D(1 - OL) = (20\mu m)(1 - 0.8) = 4\ \mu m \tag{4.3}$$

Number of pulses in a 1 mm line is,

$$n_p = 1/d_p = 1/(0.004\ mm) = 250\ number\ of\ pulses\ per\ mm \tag{4.4}$$

The number of pulses per unit area is thus,

$$N_p = (n_p)^2 = (250)^2 = 62500\ number\ of\ pulses\ per\ mm^2 \tag{4.5}$$

The effective number of pulses,

$$N_{eff} = focal\ spot\ area \times N_p = \pi \times (0.01mm)^2 \times 62500 \sim 20\ number\ of\ pulses \tag{4.6}$$

So, $N_{eff} = 20$. The experimental setup is given in figure 2.4 (b).

Laser irradiations were carried out in two processing environments, in ambient air and in high vacuum conditions (10^{-7} mbar). HSFLs were obtained for ambient and high vacuum processing conditions ($10^{-7} mbar$) for the same peak fluence $F_p = 0.32\ J/cm^2$ and an effective number of pulses of 20. The resulting HSFLs have a period of 42 nm ± 8 nm and 80 nm ± 10 nm for ambient and vacuum conditions respectively as shown in the

SEM images presented in figure 4.1 (a, b, d & e). The amplitude of the HSFLs is in the sub-20 nm range as shown by AFM in figure 4.1 (c) and (f). Conducting experiments in these two conditions is significant because

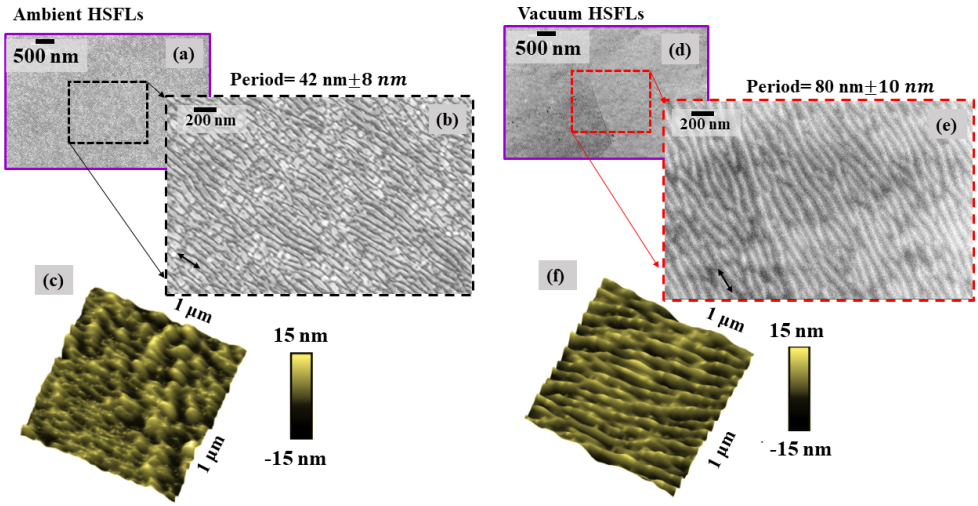

Figure 4.1: (a, b, d & e): SEM images of W sample irradiated by fs laser with $F_p = 0.32 J/cm^2$ and N= 20 for ambient HSFLs (a & b) and vacuum HSFLs (d & e). (e & f): AFM images (1 μm x 1 μm) of ambient (e) and vacuum (f) HSFLs.

one environment involves the laser interacting with atmospheric oxygen, while the other environment has a minimal oxygen presence. This will help us to distinguish between the laser-generated oxides and the oxides accumulated over time after laser irradiation, as a first step towards an understanding of the oxidation mechanics. The techniques used to better understand oxides on ambient and vacuum HSFLs are wettability measurements together with XPS analyses over a period extending up to 84 days after the fabrication of HSFLs.

4.2 Differentiating the oxides present on ambient and vacuum HSFLs

4.2.1 Laser generated oxides on HSFLs

Water Contact Angle (WCA) measurements and XPS analyses were performed on non-irradiated W and HSFLs generated on W surfaces in ambient and high vacuum to analyze the surface chemistry. The WCA was extracted with the 'contact angle' plugin in the Image J software [196].

The WCA measurement taken after the laser fabrication in ambient and vacuum conditions, and both samples exposed to the same laboratory conditions for 10 minutes is as follows: Ambient HSFLs have a WCA of $\sim 0^o$ (super hydrophilic) while HSFL generated in high vacuum have a WCA of $\sim 58^o$ (hydrophilic) (figure 4.2 (a & b)). This is very close to the WCA seen for non-irradiated, polished W samples (taken over a period of 40 days and measurements started after 2 weeks of polishing), $\sim 55^o \pm 3^o$. XPS results presented in figure 4.2 (c) & (d) show W 4f high resolution (HR) peaks one hour (with the samples exposed to the same laboratory conditions after laser irradiation) after laser irradiation. For ambient HSFLs (figure 4.2 (c)) the doublet at 31.3 eV and

33.43 eV corresponds to bulk W metal (W^0 oxidation state) and the doublet at 35.9 eV and 38 eV corresponds to W^{6+} oxidation state, indicating that the oxide formed is WO_3 [229, 230]. However, for vacuum HSFLs (figure 4.2 (d)) the doublet corresponding to W^{6+} is much weaker. The slight increase in WCA of laser irradiated samples

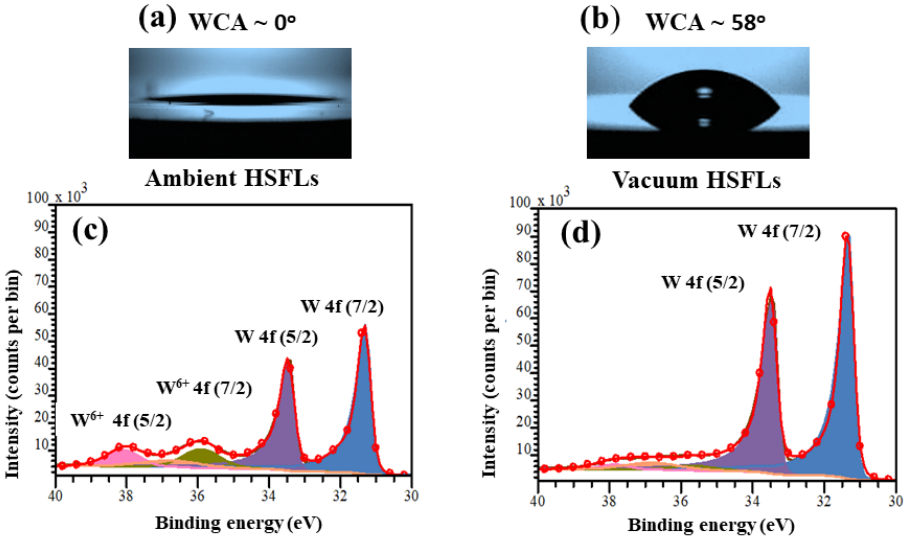

Figure 4.2: (a & b) Camera images of contact angles measured after 10 minutes of fabrication for (a) ambient HSFLs (b) and vacuum HSFLs generated by fs laser with $F_p = 0.32\ J/cm^2$ and N= 20. (c & d) HR XPS peaks for W 4f spectra one hour after fs-laser irradiation. (c)Ambient HSFLs show the doublet peaks corresponding to W^{6+} oxidation state. (d) Vacuum HSFLs have no doublet peaks corresponding to any oxidation states of W other than those corresponding to the bulk W.

fabricated in vacuum or inert gas atmosphere compared to laser irradiated samples in ambient air is well explored [150, 149]. It is usually attributed to non-polar functional groups being attached on the surface coming from the contaminations inside the vacuum chamber and the absence of laser-generated oxides which are usually polar. For laser-generated surfaces in ambient conditions the presence of oxides, being polar in nature is given as a reason for the initial super hydrophilicity [150, 231].

This may be true here considering laser-generated WO_3 makes ambient HSFLs initially super hydrophilic and the absence of this oxide increases the WCA for vacuum HSFLs. **Ambient HSFLs therefore react with atmospheric oxygen giving rise to a WO_3 film that doesn't appear for vacuum HSFLs at this stage** (i.e., 1h after laser texturing). The oxide layer generated under an ambient environment is most likely a laser-generated oxide layer formed by the interaction of atmospheric oxygen with the hot metal produced by ultrafast laser heating.

4.2.2 Influence of carbon contamination and oxides on aging

The WCA for both ambient and vacuum HSFLs were measured after 1 hour, 2 hours, 3 hours, 4 hours, 1 day, 9 days, 24 days and 84 days of same kind of laboratory exposure. The WCA measurements were done for the same irradiated area, each for ambient and vacuum HSFLs, with air blow used in between the measurements and also making the consecutive time interval measurements (1 hour to 4 hours) at different locations of the irradiated area

to ensure that there is no residual water affecting the contact angle measurements. The WCA of both ambient and vacuum HSFLs increases with time (as shown in figure 4.3 (a)), while still remaining in a hydrophilic state (i.e. $< 90^0$), as already reported in the literature for nanosecond laser-generated micro-structures on W [232].

As per literature [231, 233], the reason for this WCA increase is the accumulation of C-C/C-H hydropho-

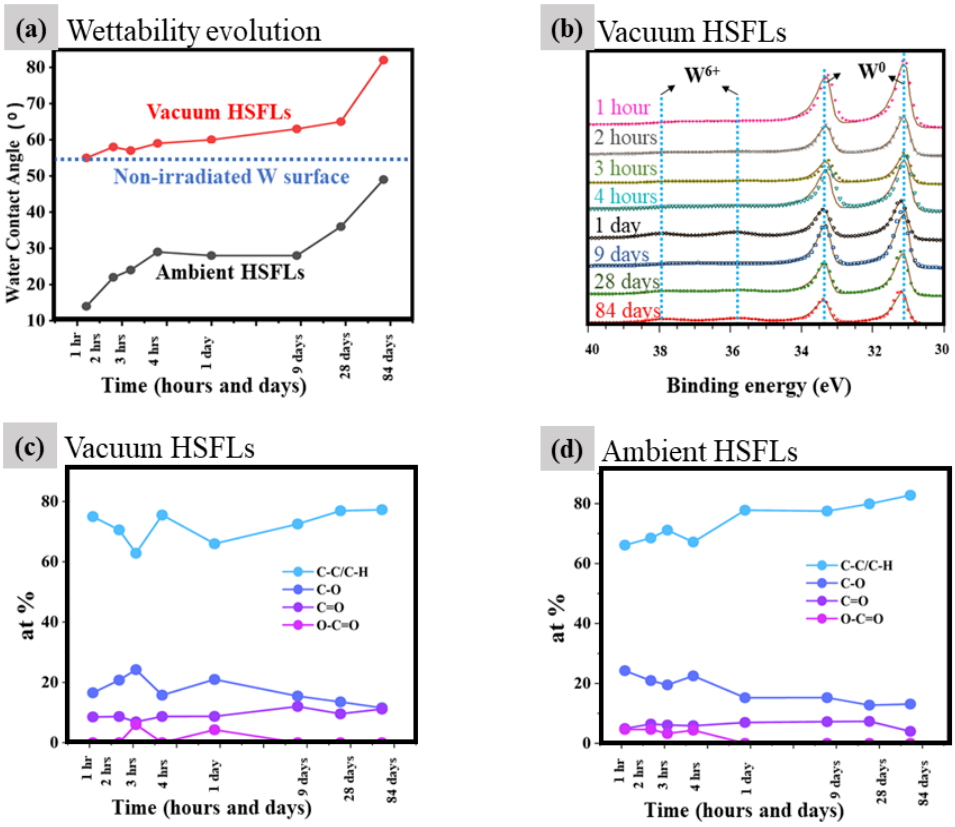

Figure 4.3: (a) WCA evolution with time over a period of 84 days after fabrication for vacuum (red) and ambient (black) HSFLs produced on W by fs laser irradiation with $F_p = 0.32\ J/cm^2$ and N= 20. The blue line indicates WCA of the non-irradiated W surface. (b): High resolution W 4f XPS spectra obtained for different time frames after fabrication for vacuum showing that the oxide accumulation does not change the peak position with 6+ oxidation state resulting in WO_3 stoichiometry. (c & d): The plot of relative concentrations (at. %) of all the functional groups associated with carbon (C-C/C-H, C-O, C=O, O-C=O) from the C1s XPS spectra for vacuum (c) and ambient (d).

bic functional group on the surface over time as seen in the XPS quantification derived from C 1s spectra for ambient HSFLs in figure 4.3 (d). The evolution of WCA for ambient HSFLs is consistent with the carbon contaminations from the atmosphere, but not for vacuum HSFLs as shown in figure 4.3 (c). For XPS measurements, 5 different samples were used to measure the data for the first four hours (one sample for each hour) to 1 day after laser irradiation both for ambient and vacuum HSFLs. Later the same sample was used to measure the variation of XPS data for 9 days, 28 days and 84 days each for ambient and vacuum HSFLs exposed to the same laboratory conditions. The W 4f peaks for vacuum HSFLs show a change in W^{6+} peak intensity corresponding to oxidized tungsten (figure 4.3 (b)). There are no recognizable W^{6+} peaks after 1 hour and clear peaks are visible after 84 days (in figure 4.3 (b)). We infer that further oxidation takes place on the vacuum HSFLs surface. Furthermore, the XPS peak positions suggest that the oxide formed over long delays is in the stoichiometry of WO_3.

As discussed in the previous section and as seen in the literature [150, 231], such an increase in WO_3 content should contribute to a decrease in WCA. But, figure 4.3 (a) clearly indicates an increase in WCA over time for vacuum HSFLs. This discrepancy may be due to **major differences between the laser-generated oxides forming over short timescales (ns) and oxides accumulated over larger time scales (days), in ambient and vacuum conditions respectively.** In order to investigate this difference we are performing STEM analysis of the HSFL cross-sections obtained for ambient and vacuum conditions (after 2 months of laser fabrication and exposed to the same laboratory environment) along with non-irradiated W as elaborated below

4.2.3 Structure of oxides from STEM-crystallography analysis

In order to further investigate the different types of oxides involved in this study, high-resolution STEM cross-sectional images are obtained for ambient HSFLs, vacuum HSFLs, and non-irradiated W lamellae as shown in figure 4.4 (a) and figure 4.5 (a), (d) respectively. These images were taken two months after the fabrication process. From figure 4.4 (a) - (e) the first few nanometers (approximately 2 nm) of the ambient HSFL are crystalline, shown by the yellow arrows in figure 4.4 (e), a conclusion supported by the diffraction pattern obtained in figure 4.4 (f) and corresponding indexing in figure 4.4 (g).

HR STEM images of vacuum HSFLs (figure 4.5 (a) & (b)) show an amorphous-like layer at the tip of the HSFL, as confirmed by the FFT in figure 4.5 (c).

A native WO_3 layer, which forms on the tungsten surface when it comes into contact with ambient air, is also evident on the non-irradiated tungsten surface. This presence has been substantiated through STEM-EDX and XPS data, as depicted in figure 4.5 (f) and (g), respectively. Edges of non-irradiated W in figure 4.5 (d) seem to have a 3 nm thick amorphous layer (FFT in figure 4.5 (e)). The literature also corroborates our results where the most common oxide of W at room temperature is amorphous WO_3 [234, 235].

For ambient HSFLs, the inter-planar distance calculated from figure 4.4 (e) is d_{130} = 0.23 nm. This measurement closely aligns with the inter-planar distance of the (130) plane in monoclinic WO_3 [236] where d_{130} = 0.22 nm. Further support for our hypothesis that the laser-generated WO_3 may indeed possess a crystalline structure, specifically monoclinic, is drawn from the FFT analysis of the inset in figure 4.4 (g). The indexing process was carried out using the Dif-Wshp21 software [194]. We employed the CIF data for monoclinic WO_3, which was downloaded from the Crystallography Open Database (COD ID: 1528915), and found it to be in agreement with our experimental FFT data, where d_{130}=0.23 nm. Haase et al. [237] have also reported similar observations on femtosecond laser irradiation of W giving rise to monoclinic WO_3 nanoparticles.

Structure and wettability are known to be closely related in the case of WO_3. C. V. Ramana et al. [238] observed a change in WCA from $\sim$ 75 degree to $\sim$ 5 degree as the structure changes from amorphous WO_3 to crystalline WO_3 (amorphous WO_3 exhibits higher WCA than crystalline WO_3). This is due to a change in surface

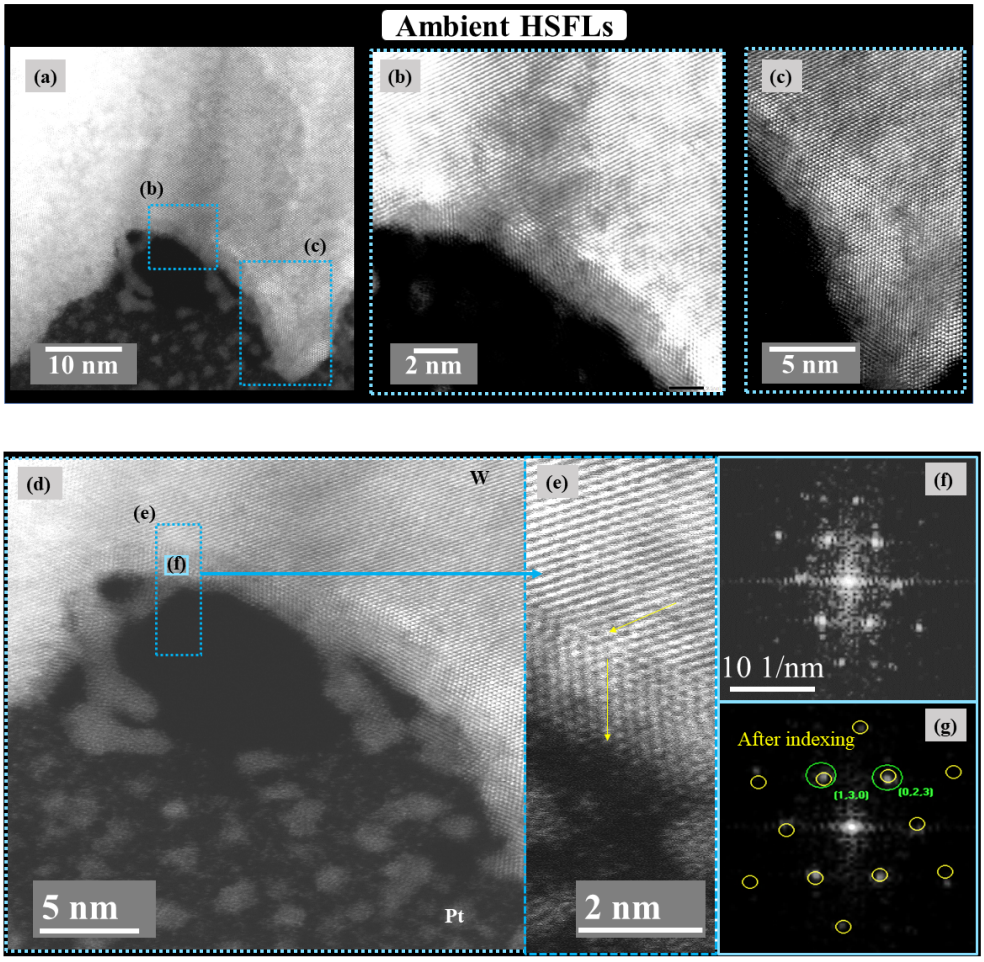

Figure 4.4: High-resolution STEM probing of W irradiated by fs laser with $F_p = 0.32\ J/cm^2$ and N= 20 for ambient HSFLs: (a, b & c): HR-STEM images with different zooms showing the contrast between the bulk of W sample and the edges (where the presence of WO_3 is supposed to be) (d & e) HR-STEM images of FIB-extracted lamellae with FFT reported in (f) and crystal indexing in (g) for HSFLs produced .

energy, where a decrease in WCA is observed with increasing surface energy [239]. Crystalline WO_3 has a higher surface energy compared to amorphous WO_3 due to its larger surface area, contributing to the observed change in WCA [240, 241]. This is in perfect agreement with our results **showing the amorphous WO_3 layer on vacuum HSFLs accumulated over time with ambient exposure is less hydrophilic than the crystalline WO_3 formed on ambient HSFLs on ultrafast laser irradiation.**

4.3 Oxidation Mechanism

As seen in Chapter 1, while the laser-induced oxidation mechanism of CW or ps or ns lasers seems to agree with the classical oxidation mechanism based on diffusion, the mechanism of femtosecond laser-induced oxides is scarcely discussed. In order to establish an oxidation mechanism, specific to the femtosecond laser parameters that we have used here, leading to the formation of monoclinic WO_3 on tungsten, along with the HSFLs we took the following approach,

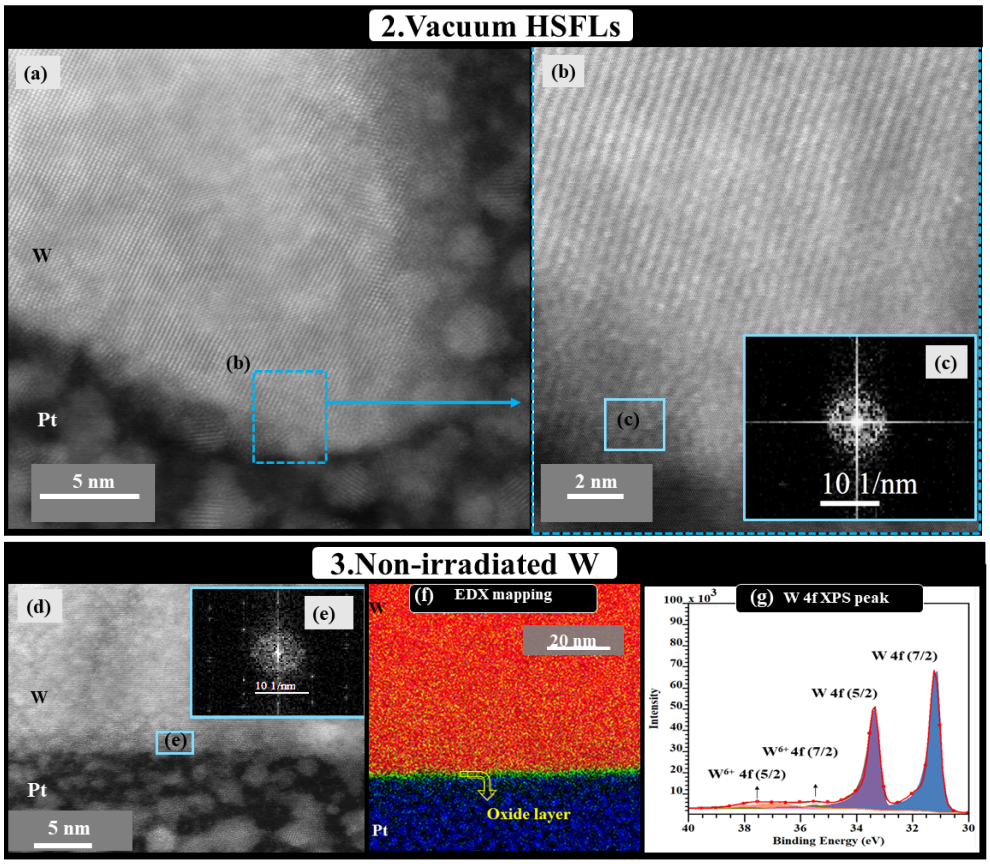

Figure 4.5: High-resolution STEM probing of W irradiated by fs laser with $F_p = 0.32\ J/cm^2$ and N= 20 in case of vacuum HSFLs and non-irradiated W: (a & b) HR STEM image of FIB-extracted with FFT reported in (c) for HSFLs produced under vacuum conditions. (d) HR-STEM image of tungsten surface without any laser irradiation with its FFT reported in (e). (f & g): STEM-EDX mapping of non-irradiated W with (f) showing a fine layer of oxide (represented by green color) on W (orange) protected with Pt layer (blue) for lamellae preparation. (g) is HR XPS W4f peaks corresponding to non-irradiated W.

- Finding the time scale (δt) for the temperature range favorable for the formation of monoclinic WO_3.
- Finding the diffusion length of oxygen during this time scale (δt) during the temperature range favorable for the oxide formation.
- Does this diffusion length/observed oxide layer thickness agree with the dissociative chemisorption rate of oxygen and the collision rate of oxygen on the W surface within δt?

From the literature, it is possible to establish a temperature range for the oxidation of tungsten resulting in the formation of monoclinic WO_3. This data can be considered conventional, collected for higher temperature ranges from mostly furnace oxidation data. After finding this temperature range (ΔT), we need to know how long this temperature range persists on our sample surface due to fs laser irradiation. This can be done by TTM-MD simulations by giving the laser parameters used to generate the HSFLs as input data.

In the next step, we need to find out whether δt obtained from TTM-MD simulations allows for the formation of 2 nm thick monoclinic WO_3 (as observed from the STEM images) by diffusion of oxygen. This is done by calculating the diffusion length of oxygen on W for ΔT and δt.

To validate the results, we have to verify that the rate of dissociative chemisorption of oxygen from the atmosphere onto the W surface and the collision rate of oxygen molecules are sufficient within δt to generate an oxide layer as thick as 2 nm.

4.3.1 TTM-MD simulations: temperature range and time scale for femtosecond laser-assisted oxidation

The cool down after the laser pulse should result in monoclinic WO_3, as confirmed by STEM. As we have already seen in chapter 1, WO_3 usually undergoes polymorphism resulting in monoclinic WO_3 below 600 K. This indicates polymorphism during laser irradiation is a possible phenomenon to explain oxide formation. Based on literature, we know that WO_3 is formed **between 1273 K and 600 K probably and undergoes polymorphism below 600 K resulting in monoclinic** WO_3 (assuming that above 1273 K WO_3 is volatile). This temperature window is the most likely temperature range where oxidation of W resulting in WO_3 will happen.

The next objective is to determine the time scale (δt) during which the sample stay at temperatures between 1273 K and 600 K following a laser pulse which can be achieved through simulations involving the solution of the heat diffusion equations within W.

Solving 1D heat equation

Before proceeding to a proper usage of TTM-MD simulations (with Dr. Djafar Ibbaden), we obtained a rough time scale (δt) by solving a 1D heat equation with a Python code as attached in the appendix of the thesis (section A.1.2). The assumptions are as follows:

- By solving the 1-D partial differential heat equation for tungsten below its melting point (below 3695 K) we can deduct an approximate time required for the formation of WO_3.
- We chose to do the program below the melting point to avoid the complexity of phase transitions. In addition, the temperature range favorable for the formation of monoclinic WO_3 (1273 K to 600 K) is below the melting point.
- We are finding the heat diffusion into one micrometer depth of tungsten, by defining specific number of locations inside this region.
- We are finding out the thermal diffusivity corresponding to the temperature variation between 300 K and 3000 K along the depth of tungsten using extrapolation of values obtained from the literature.
- As the source term, we are using an input exponential equation as obtained from TTM-MD simulations to account for the exponential heat dissipation into the depth of tungsten for the given laser parameters.
- In order to account for the source term, we are using an input exponential equation as obtained from TTM-MD simulations.

The 1-D heat equation is given by,

$$\frac{dT}{dt} = a\frac{d^2T}{dx^2} \tag{4.7}$$

where T is the temperature at time t and depth x from the surface of the tungsten with thermal diffusivity 'a' expressed in cm^2/s and is given by,

$$a = k/Cp \tag{4.8}$$

where k is the thermal conductivity (W/m K), C is the specific heat capacity (J/Kg K) at temperature T, and ρ is the density of W which is 19250 Kg/m^3 when in the solid state. k and C_p can be obtained for different values of temperature (300 K to 3000 K) by interpolation [242, 243]. Later these values can be used to find the thermal diffusivity (a) for tungsten using equation 4.8 as can be seen in figure 4.6.

Another input to give to the Python program is the source term or the initial temperature to be used,

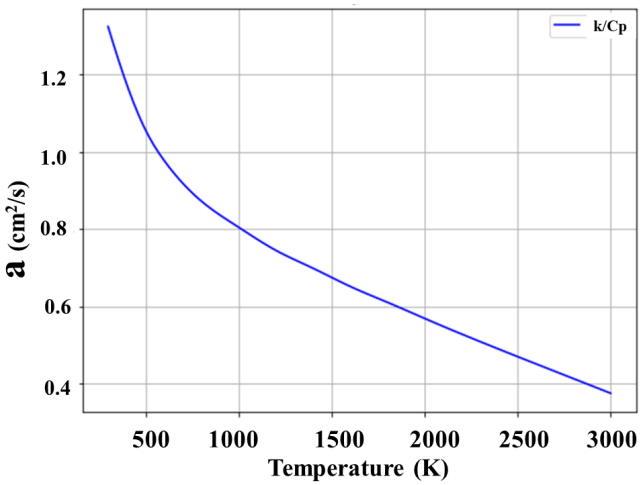

Figure 4.6: Variation of thermal diffusivity (a) of tungsten obtained from the interpolated values of k and Cp from 300K to 3000K.

which is the heat variation on the surface of tungsten around 3000 K. We used the TTM-MD to give us the temperature profiles along the depth of few tens of nanometers of W. To be more precise, we used more than one source term (giving the temperature profiles below 3000 K at various times after the laser pulse hits the surface, like, at 500 ps, at 1500 ps, etc.) for the laser parameters we used (λ = 1030 nm, 300 fs, $Fp = 0.32\ J/cm^2$). And used these curve fits as the source terms to give us different outputs to compare.

Figure 4.7 shows the variation of temperature with time and cooling rates obtained by solving the 1-D heat equation. The two outputs correspond to two source terms used in the program (at 500 ps and 1500 ps respectively for figure 4.7 (a) & (b)). The cooling rates are obtained in both cases by finding the average dT/dt of the consecutive points from the curves. Interestingly, in both cases, the cooling rates $\sim 10^{11} K/s$ are similar and are in agreement with the fast cooling associated with fs laser irradiation on metals [49].

Most importantly, the curves which give the temperature profile of laser-irradiated W at the surface at different times, enable us to find the time spent in the temperature window (1273 K to 600 K) which is given by δt = 9.5 ns and 9.4 ns as derived from figure 4.7 (a) & (b) respectively. This approximate calculation was helpful in establishing the need for wider and proper simulations and hence we utilized TTM-MD simulations.

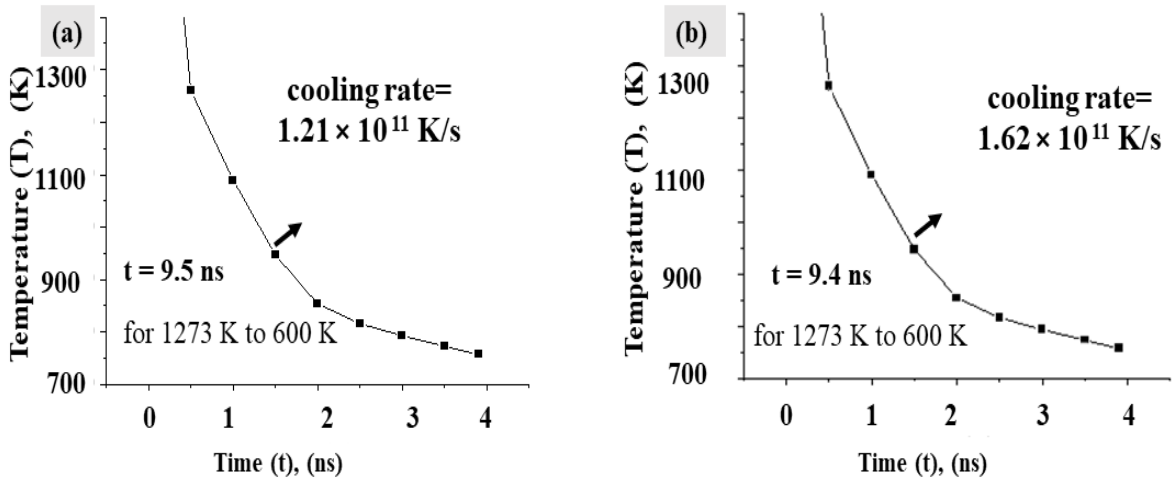

Figure 4.7: (a) & (b): Temperature variation with time after laser irradiation at W surface obtained by solving 1 D heat equation. The cooling rates are obtained by averaging the mean of the consecutive points dT/dt on the graphs. (a) is obtained by using the exponential equation at 500 K as the source term in the program and (b) is obtained by using the exponential equation at 1500 K as the source term in the program.

TTM-MD Simulations (work done by Dr. Djafar Ibbaden)

Hybrid Computational Model

A hybrid method combining the Two Temperature Model (2TM) and Molecular Dynamics (MD) is performed to simulate ultrafast light interactions with tungsten (W) using the LAMMPS package [244, 245]. The initial domain of the simulation box is defined by the dimensions Lx × Ly × Lz = 1000 a0 × 30 a0 × 30 a0 (with a0 = 3.16 Å). The tungsten atoms structure is defined as a Body-Centered Cubic (BCC) crystal spercell block that fills the region [500 a0, 900 a0] along x-direction, equivalent to 900900 atoms. A non-periodic boundary condition is set at the rear part of the system as described by Schäfer et al. [246]. The initial simulation domain is divided into two distinct regions (figure 4.8). In the TTM-MD part, both classical Newton's equation of motion and the electronic part of the TTM equation are solved [27] in a grid of 100 × 3 × 3 equivalent to 3.16 × 9.48 × 9.48 nm^3. The TTM part (bulk) is of thickness 4.5 μm and a mesh of 450 × 1 × 1 is built to ensure both heat dissipation and pressure wave absorption. The TTM-MD and TTM regions are separated by a Non-Reflecting Boundary Condition (NRBC) as described by Schäfer et al. [246]. The initial thickness of the NRBC region ∼ 8 Å is slightly larger than the cutoff radius value of ∼ 7.5 Å provided by the interatomic potential.

TTM-MD model integrates non-equilibrium coefficients as electronic specific heat $C_e(T_e)$, electron-phonon

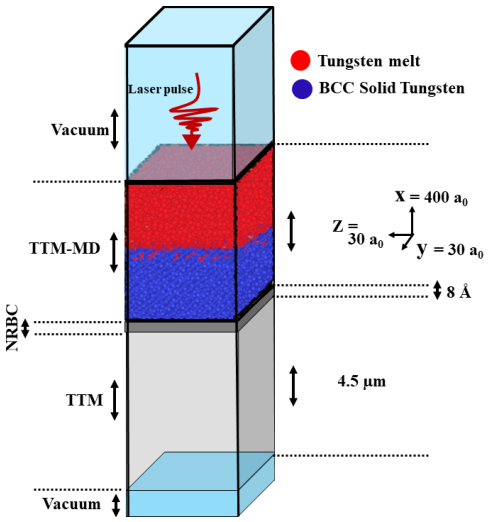

Figure 4.8: Initial setup geometry of the W sample used to model ultrafast laser interaction. The extreme upper and bottom parts represent the surface vacuum part. TTM-MD and TTM schemes are solved in the red-blue and gray-colored regions respectively. Tungsten atoms in the solid BCC and melted phase are colored in blue and red, respectively

coupling factor ($G_e(T_e)$), and electron thermal conductivity ($\kappa_e(T_e)$)). $C_e(T_e)$ used in this work is computed by first-principles calculations as described in the study of Bevillon et al [247]. The $\kappa_e(T_e)$ is computed using Anisimov approximation [248] as,

$$\kappa_e(T_e) = \kappa_0 T_e / T_l \tag{4.9}$$

where $\kappa_0 = 170\ Wm^1K^1$ at T0 = 300 K (initial temperature of the system) as reported in the work of Stojanovic et al. [221] and T_l is the ionic temperature. $G_e(T_e)$ is also a function of electronic temperature (T_e) where the values estimated by Lin et al. [249]. The source term S of the laser has a Gaussian temporal shape and an exponentially decreasing amplitude in depth x following a Beer-Lambert law:

$$S(x,t) = (\frac{2F}{t_p l_p})\sqrt{\frac{ln(2)}{\pi}} e^{(-4ln(2).\frac{(t-t_0)^2}{t_p^2}} e^{\frac{-x}{/}l_p} \tag{4.10}$$

where t_p is the pulse duration, and t_0 corresponds to the time of the laser pulse maximum. F is the absorbed fluence defined by,

$$F = F_0(1 - R(T_e)) \tag{4.11}$$

with $R_e(T_e)$ the reflectivity and $l_p(T_e)$ the laser penetration depth computed at the wavelength $\lambda = 1030$ nm. Both $R_e(T_e)$ and $l_p(T_e)$ are temperature-dependent, as provided by ab initio calculations reported by Bevillon et al. [250].

The initial atomic configuration is heated up to 300 K using a micro-canonical ensemble (NVE) for 50 ps. Additionally, the electronic temperature in the TTM continuum part is set to an initial temperature of 300 K. Laser operating conditions similar to the experimental conditions with t_p= 300 fs and $F_p = 0.32\ J/cm^2$ for pulse duration and peak fluence are considered respectively. After the laser energy deposition, the thermodynamics of the system was tracked for 9 ns. We employed a time step δt = 1 fs and Embedded Atom Model (EAM) type

potential developed by Marinica et al. [220]. The local atomic structures are investigated using the Common Neighbor Analysis algorithm (CNA) [247, 251] as implemented within the OVITO software [225].

Temperature variation and time scale

From TTM-MD simulations, we obtain the temperature profile across W at different snapshots of time as shown in figure 4.9 (a). From this, we have deduced the temperature profile at the surface of W as shown in figure 4.9 (b) and we can extract the **time for the temperature to change from 600 K to 1273 K and should result in monoclinic WO_3 is δt = 7.2 ns** (close to the result obtained from solving the 1-D heat equation) for a single pulse, for the laser parameters used (λ=1030 nm, 300 fs, $Fp = 0.32\ J/cm^2$). The second step is to see if oxygen can diffuse through W within this short time scale to cause oxidation.

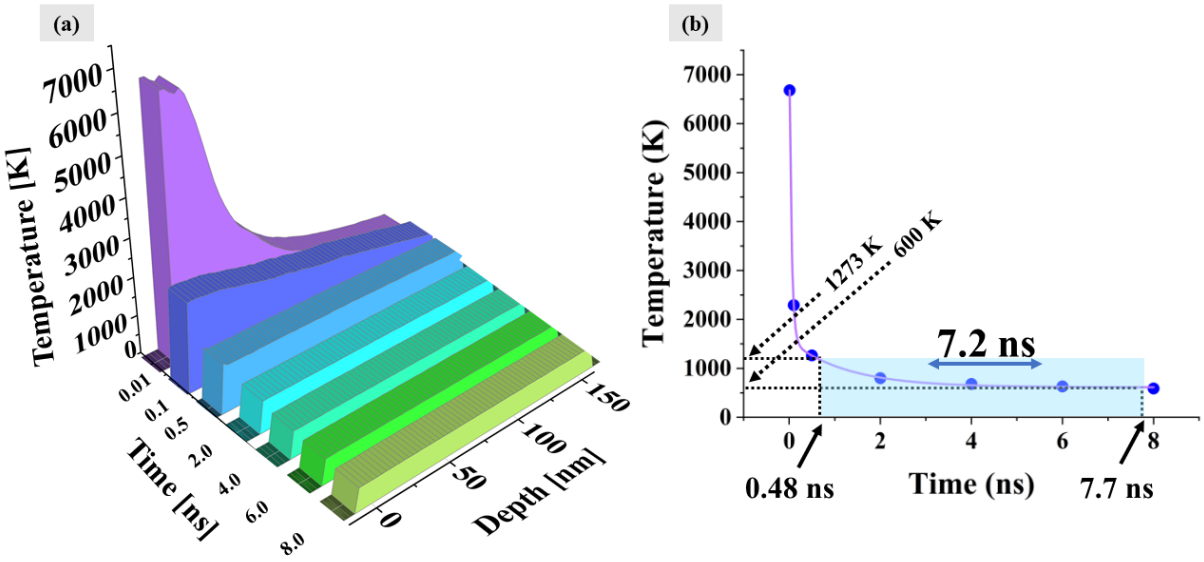

Figure 4.9: (a) Temperature depth profile in W irradiated by femtosecond laser with $Fp = 0.32\ J/cm^2$ and N= 20 at different snapshots of time obtained from TTM-MD simulations (b) Temperature evolution versus time at the surface of the W sample.

4.3.2 Diffusion of oxygen

The diffusion length (λ) of oxygen during this 7.2 ns can be calculated knowing the diffusion coefficient (D) and the diffusion time (τ) using the equation [252],

$$\lambda = (\tau D)^{0.5} \tag{4.12}$$

Or

$$D = \lambda^2/\tau \tag{4.13}$$

The sample only spends 0.82 ns in the temperature range 1273K to 1000K, a range for which the diffusion coefficient value for oxygen in tungsten is approximately $D = 10^{-8}\ m^2/s$. The temperature transition from 1000

K to 600 K takes a longer time span of 6.38 ns, but the diffusion coefficient is lower in this range is $D = 10^{-9}\ m^2/s$ [253]. According to equation 4.13, the diffusion lengths for the temperature ranges of 1273 K to 1000 K and 1000 K to 600 K are determined to be 2.8 nm and 2.5 nm, respectively. **This result effectively confirms that the time δt is sufficient for oxygen to diffuse through a few nanometers of W and hence form oxides.**

However, the experimental results demonstrate the existence of an extremely thin oxide layer, measuring approximately 2 nm, as evidenced in the STEM ADF images (figure 4.4). This phenomenon can be attributed to a significant factor: as a few mono-layers of WO_3 form, the restricted time window during this brief interval poses a growing challenge for oxygen atoms to effectively penetrate and diffuse through these oxide mono-layers. The diffusion length of oxygen atoms through WO_3 is much smaller in the given temperature range (the diffusion constant is $5.55 \times 10^{-12}.s^{-1}$ at 1073 K) [254].

In order to confirm the formation of oxide through diffusion, we also have to make sure that the dissociation time of oxygen molecules and the collision rate of oxygen atoms is sufficient to support the observed oxide layer thickness of about 2 nm.

4.3.3 Dissociative chemisorption and Collision rate of Oxygen

Proceeding to the third step, we have to confirm if the collision rate of oxygen on the W surface at the partial pressure of oxygen in the atmosphere is enough to form a 2 nm thick oxide. To find out the collision rate, the kinetic theory of gases can provide the number of oxygen molecules n impacting a W surface at a particular pressure and temperature per square centimeter per second (n) [180],

$$n = \frac{(PN_A)}{\sqrt{(2\pi RMT)}} \tag{4.14}$$

in m^2/s, where P is pressure in Pa (oxygen pressure in the atmosphere = 21.22×10^3 pa), M is the molecular weight of oxygen (0.032 Kg) and T is the temperature in Kelvin (298 K), N_A is the Avogardo number (6.022×10^{23}) and R is the gas constant ($8.314\ J/mol\ K$).

$$n = \frac{[(21.22 \times 10^3\ pa)(6.022 \times 10^{23})]}{[\sqrt{(2\pi(8.314\ J/molK)(0.032\ Kg)(298\ K)}]} = 5.72 \times 10^{22} \tag{4.15}$$

We get the value of n is 5.72×10^{22} molecules per square centimeter per second.

i.e. the total number of oxygen atoms will become $2n = 2 \times 5.72 \times 10^{22} = 1.14 \times 10^{23}$ since one oxygen molecule will contribute to two oxygen atoms.

The next step is to find the number of tungsten atoms per centimeter square. Keeping in mind that different atomic planes have different atomic densities and the monoclinic WO_3 we obtained from STEM indexing

is in (130) configuration (figure 4.4), we assume the same configuration for the exposed W surface. The planar density of (130) plane is 6.3×10^{14} W atoms per cm^2 [180].

This means that to form a monolayer of WO_3, $3 \times 6.3 \times 10^{14}$ oxygen atoms interacts with 6.3×10^{14} W atoms per centimeter square per second. In other words, the time required to form a monolayer of WO_3 is,

$$\frac{[3 \times 6.3 \times 10^{14}]}{[2n]} = 16.58\ ns \tag{4.16}$$

Using the 7.2 ns window computed through TTM-MD for a single pulse for oxidation to happen, we can calculate that 20 pulses would lead to the formation of approximately 9 mono-layers of the oxide. This approximately agrees with the observed oxide thickness from STEM images, which is 2 nm, meaning 9 mono-layers (inter-planar spacing i.e., d = 0.22 nm, and 2 nm ÷ 0.22 nm = 9 mono-layers) of monoclinic WO_3 (130 orientation). This also corresponds to the 9 atomic planes visible in figure 4.4 (e).

To summarise, we are proposing a multiple pulse accumulation of oxide for the formation of monoclinic WO_3 seen in association with fs laser-induced HSFLs on W whose formation is based on diffusion mechanism.

The reason behind considering the potential for a pulse-by-pulse accumulation of the oxide layer stems from the apparent absence of material ablation, also evidenced by TTM-MD simulations. These calculations were performed on tungsten alone, whose evaporation point is comparatively high compared to that of WO_3 which sublimates above 1273 K. However, the simulations predict the sample remains at such temperature for less than 0.5 ns per pulse. Considering a reported sublimation rate for WO_3 of $\sim 1.5 \times 10^{-16} g.cm^{-2}.s^{-1}$ at 1643 K [255], this would lead at worse to the evaporation of less than 3 oxygen atoms per cm^2, which is negligible in any case.

Another crucial parameter to consider is the dissociation time of oxygen molecules: Literature suggests that dissociative chemisorption of oxygen molecules can take place within 10^{-13} s on W surface at high temperatures [256]. Dissociation of oxygen molecules can therefore happen within the nanosecond time scale (7.2 ns) obtained from TTM-MD simulations.

These calculations substantiate the formation of monoclinic WO_3 during femtosecond laser interaction with tungsten surface by oxygen diffusion between 1273 K and 600 K with a pulse-by-pulse accumulation of oxides. Moreover, WO_3 is known to exist at GPa pressures [257], hence making it stable at the laser-induced high-pressure regime [258].

To conclude, this chapter sheds light on the oxidation mechanism associated with femtosecond laser irradiation on tungsten resulting in HSFLs. It starts with the large area fabrication of HSFLs on W in ambient and vacuum conditions. To get an initial idea of the surface chemistry both wettability analysis and XPS analysis come in handy. These analyses reveal major differences in the laser-generated oxide and the oxides accumulated on HSFLs over time from ambient exposure. Later with the help of crystallography indexing with the FFT obtained

from STEM imaging, it is possible to differentiate these oxides - laser-generated oxides as monoclinic WO_3 and the accumulated oxides over time as amorphous oxides. In addition, the variation in the wettability behavior associated with these oxides holds the potential for tuning the physicochemical response of the laser-irradiated surfaces. Further, an oxidation mechanism is put forward which is based on the multi-pulse accumulation of oxides, in which fs laser-induced oxidation is explained by the diffusion mechanism. These main results are illustrated in figure 4.10. These observations and analysis address most of the questions associated with the fs laser-assisted oxidation seen with the formation of HSFLs on tungsten and open the door for tuning potential applications by controlling the type of oxides that can be generated. Moreover, this study also contributes to future investigations as will be discussed in the next section.

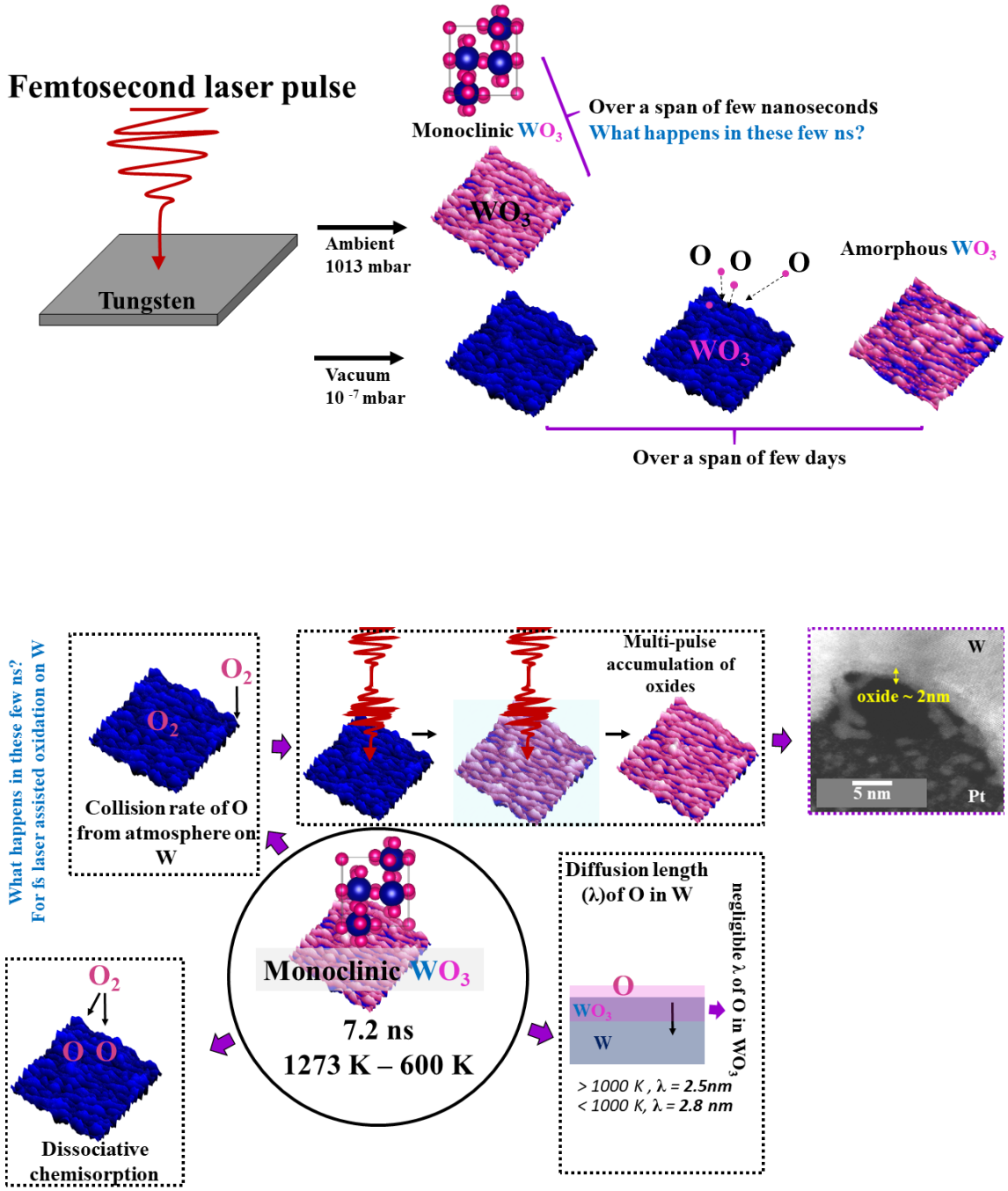

Figure 4.10: An overview of the femtosecond laser-induced oxidation mechanism on W.

* * *

Conclusion & Perspectives

While femtosecond laser-induced nanostructures have been explored greatly in the last 50-plus years, surface chemistry accompanying topographical modification is yet to be fully understood. Even though laser-generated oxides due to fs-laser irradiation are known to have a strong effect on the surface properties of materials in various industrial applications including tribology, [259], color marking [153], etc., the mechanism of oxidation and its role in nanostrucutre formation is scarcely discussed.

This thesis is aimed at understanding surface chemistry alterations accompanied during laser irradiation using a combination of surface-sensitive characterization tools and numerical simulations. This theses focused on the mechanism of laser-induced oxidation and its influence on nanostructure formation by performing experiments in ambient as well as vacuum environmental conditions.

The important findings and conclusions are detailed below:

(i) Femtosecond laser-induced high-frequency LIPSS **(HSFLs) with sub-100 nm periodicity and sub-20 nm amplitude can be generated on polished W surface for a constant set of laser parameters (λ = 800 nm, 60 fs, $F_p = 0.35\ J/cm^2$, N = 25) under five different processing environments (ambient, air 10 mbar, nitrogen 10 mbar, vacuum** 10^{-7} *mbar* **and argon** 10 *mbar*). This is an indication that the formation of HSFLs on W is mostly dependent on the laser parameters rather than the processing environments.

(ii) The much-debated topic suggesting that oxidation/oxides are a precondition for nanostructure formation is invalidated. By performing experiments with in-situ sputtering (to remove the native oxides on W) and under high vacuum conditions, we conclude that **the idea of an oxidation-based origin of nanostructures cannot be generalized for all the metals, especially for HSFLs on W.** STEM-EDX and XPS data confirm the presence of a very negligible oxide content on vacuum HSFLs.

(iii) Ambient pressure influences the period of HSFLs formed on tungsten by fs laser irradiation. **The period of HSFLs increases with the air pressure. This can be explained by a hydrodynamic concept based on Marangoni instability suggesting a hydro-dynamical origin for HSFLs on W rather than an oxidation-based origin.**

(iv) TTM-MD numerical simulations confirm the hydrodynamics origin of HSFLs by defining the temperature and pressure maps of tungsten during ultrafast laser irradiation. Sub-surface cavitation is observed (accompanying the formation of HSFLs as also observed in STEM) and is attributed to the resolidification of molten tungsten. This reaffirms that **HSFLs on W are formed due to Rayleigh-Bénard-Marangoni instability induced by the rarefaction wave upon fs laser irradiation.**

(v) **Laser-generated WO_3 is crystalline with monoclinic orientation for ambient HSFLs while oxides accumulated over time are amorphous on vacuum HSFLs.** This difference in the oxide structure leads to a **difference in the final physicochemical response** of the fs laser textured surfaces, regardless of the topography (HSFLs in vacuum and ambient conditions).

(vi) Formation of monoclinic WO_3 by polymorphism is possible due to the laser-generated temperatures on the W surface. This **oxidation accumulates by multi-pulse irradiation**. The thickness of laser-induced monoclinic WO_3 on ambient HSFLs as seen by STEM images (2 nm) can be explained by the diffusion length and the classical collision rate of oxygen on tungsten, hence **suggesting an oxidation mechanism based on diffusion due to laser-induced temperatures** and pulse-by-pulse accumulation of oxides.

These findings pave the way for potential future research as follows;

(i) An interesting future approach is to investigate the oxidation mechanism associated with **different temporal pulse shaping.** By changing the pulse duration of the laser, we can limit the diffusion length of oxygen on metals and hence the thickness of oxide. Similarly, we can investigate the influence of temporally modulating the frequency, amplitude and phase of a laser pulse on the surface chemical modification.

(ii) Considering the **wide potential for tungsten and its oxides in catalytic applications,** exploring the catalytic properties of nanostructures generated under various gaseous conditions could provide significant contributions to laser-induced surface chemistry-based applications. The photo-catalytic property of tungsten oxide is highly influenced by the percentage of amorphous to monoclinic WO_3 at the surface [172]. It is also reported that the change in the crystal structure of the tungsten oxide can influence the electro-catalytic properties of the surface [171].

(iii) An in-depth study on the **surface chemistry mechanisms during irradiations of tungsten in nitrogen environments (and other gaseous conditions)** will add to the chemical alterations associated with laser irradiations. This is because, even though we did not go deeper into the surface chemistry of the tungsten irradiated in a nitrogen environment, it is quite often seen that metals irradiated in nitrogen-rich surroundings or even in ambient shows the presence of nitrides [133, 135, 136]. Hence, it will be intriguing to examine the type, mechanism, and change over time (in ambient exposure) to the tungsten nitrides formed during ultrafast laser irradiation.

(iv) Investigation of fs-laser irradiation of other metals like those belonging to the same group as tungsten

(e.g. chromium), and from different groups (e.g. titanium) using a similar approach will shed light on **how material-specific ultrafast laser-assisted oxidation mechanism is.**

(v) Finally, a thorough examination of **the tunability of laser-based oxide for various surface-based industrial applications including electrochemical, biomedical, photovoltaic, etc. by controlling the type, etc. solely with laser parameters** can ultimately make a significant contribution to society and can ignite further research on this topic in the scientific community.

As we conclude this thesis, we are reminded that the pursuit of knowledge is a journey that never truly ends; it merely transforms into new questions and discoveries, forever illuminating the path forward.

* * *

Scientific Publications

Published Article

- Dominic, P., Bourquard, F., Reynaud, S., Weck, A., Colombier, J.-P., Garrelie, F. (2021). *On the insignificant role of the oxidation process on ultrafast high-spatial-frequency LIPSS formation on Tungsten.* Nanomaterials, 11(5), 1069. https://doi.org/10.3390/nano11051069.

Articles In Preparation

- Dominic, P., Iabbaden, D. Bourquard, F., Reynaud, S., Nakhoul, A., Weck, A., Colombier, J.-P., Garrelie, F. *Unveiling nature and consequences of tungsten oxidation upon ultrafast laser irradiation.* In nanoscale.
- Dominic, P., Iabbaden,D. Bourquard, F., Reynaud, S., Weck, A., Colombier, J.-P., Garrelie. *Emergence of Sub-100 nm Periodic Structures on Ultrafast Irradiated Tungsten Surfaces: Insights from Stretched Liquid Phenomena.* In physica status solidi (a).

Conferences

- LPM Japan 2023: Two oral presentations
- LIPSS international conference 2022: Oral presentation
- COLA 2021/2022: Poster presentation
- ARQUS 2022: Oral presentation

* * *

Bibliography

[1] J. Bonse, R. Koter, M. Hartelt, D. Spaltmann, S. Pentzien, S. Höhm, A. Rosenfeld, J. Krüger, (2015). Tribological performance of femtosecond laser-induced periodic surface structures on titanium and a high toughness bearing steel. Applied Surface Science, 336, 21–27.10.1016/j.apsusc.2014.08.111 doi:10.1016/j.apsusc.2014.08.111.

[2] Bonse, R. Koter, M. Hartelt, D. Spaltmann, S. Pentzien, S. Höhm, A. Rosenfeld, J. Krüger, (2014). Femtosecond laser-induced periodic surface structures on steel and titanium alloy for tribological applications. Applied Physics A, 117(1), 103–110. doi:10.1007/s00339-014-8229-2.

[3] Kruse, C., Lucis, M., Shield, J.E., Anderson, T., Zuhlke, C., Alexander, D., Gogos, G. and Ndao, S., (2018). Effects of femtosecond laser surface processed nanoparticle layers on Pool Boiling Heat transfer performance. Journal of Thermal Science and Engineering Applications, 10(3). doi:10.1115/1.4038763.

[4] Kruse, C., Tsubaki, A., Zuhlke, C., Alexander, D., Anderson, M., Peng, E., Shield, J., Ndao, S. and Gogos, G., (2019). Influence of copper oxide on femtosecond laser surface processed copper pool boiling heat transfer surfaces. Journal of Heat Transfer, 141(5). doi:10.1115/1.4043129.

[5] Antończak, A. J., Stępak, B., Kozioł, P. E., Abramski, K. M. (2013). The influence of process parameters on the laser-induced coloring of titanium. Applied Physics A, 115(3), 1003–1013. doi:10.1007/s00339-013-7932-8.

[6] Dostovalov, A. V., Korolkov, V. P., Okotrub, K. A., Bronnikov, K. A., Babin, S. A. (2018). Oxide composition and period variation of thermochemical LIPSS on chromium films with different thickness. Optics Express, 26(6), 7712. doi:10.1364/oe.26.007712.

[7] Zuhlke, C. A., Anderson, T. P., Alexander, D. R. (2013). Comparison of the structural and chemical composition of two unique micro/nanostructures produced by femtosecond laser interactions on nickel. Applied Physics Letters, 103(12). doi:10.1063/1.4821452.

[8] Kirner, S. V., Wirth, T., Sturm, H., Krüger, J., Bonse, J. (2017). Nanometer-resolved chemical analyses of femtosecond laser-induced periodic surface structures on Titanium. Journal of Applied Physics, 122(10), 104901. doi:10.1063/1.4993128.

[9] Xia, F., Jiao, L., Wu, D., Li, S., Zhang, K., Kong, W., Yun, M., Liu, Q. and Zhang, X. (2019). Mechanism of pulsed-laser-induced oxidation of titanium films. Optical Materials Express, 9(10), 4097. doi:10.1364/ome.9.004097.

[10] Ursu, I., Nanu, L., Mihăilescu, I. N. (1986). Diffusion model for the laser oxidation of metallic samples in air. Applied Physics Letters, 49(2), 109–111. doi:10.1063/1.97401.

[11] Wautelet, M. (1990). Laser-assisted reaction of metals with oxygen. Applied Physics A Solids and Surfaces, 50(2), 131–139. doi:10.1007/bf00343408

[12] Silfvast,W. (2008) Laser fundamentals.Cambridge: Cambridge University Press,isbn: 978-0-521-83345-5 978-0-521-54105-3.

[13] Alavi, S. H., Harimkar, S. P. (2015). Ultrasonic vibration-assisted continuous wave laser surface drilling of materials. Manufacturing Letters, 4, 1–5. doi:10.1016/j.mfglet.2015.01.002

[14] Dusser, B., Sagan, Z., Soder, H., Faure, N., Colombier, J. P., Jourlin, M., Audouard, E. (2010). Controlled nanostructrures formation by Ultra Fast Laser pulses for color marking. Optics Express, 18(3), 2913. doi:10.1364/oe.18.002913.

[15] Medical Applications of Ultrashort Laser Pulses, (2022). Retrieved from https://www.iap.uni-jena.de/ultrafast-optics/research/medical-applications-of-ultrashort-laser-pulses

[16] Vorobyev, A. Y., Guo, C. (2008). Colorizing metals with femtosecond laser pulses. Applied Physics Letters, 92(4). doi:10.1063/1.2834902.

[17] Ahmmed, K., Grambow, C., Kietzig, A.-M. (2014). Fabrication of micro/nano structures on metals by femtosecond laser micromachining. Micromachines, 5(4), 1219–1253. doi:10.3390/mi5041219.

[18] Chichkov, B. N., Momma, C., Nolte, S., Alvensleben, F., Tünnermann, A. (1996). Femtosecond, picosecond and nanosecond laser ablation of solids. Applied Physics A Materials Science Processing, 63(2), 109–115. doi:10.1007/bf01567637.

[19] Mishra, S., Yadava, V. (2015). Laser beam micromachining (LBMM) – A Review. Optics and Lasers in Engineering, 73, 89–122. doi:10.1016/j.optlaseng.2015.03.017.

[20] Fermann, M. E., Hartl, I. (2013). Ultrafast fibre lasers. Nature Photonics, 7(11), 868–874. doi:10.1038/nphoton.2013.280

[21] Shannon, G. What's the Difference Between Femtosecond and Picosecond Lasers?, Retrieved from https://www.machinedesign.com/mechanical-motion-systems/article/21836637/whats-the-difference-between-femtosecond-and-picosecond-lasers

[22] What's the difference between constant wave (CW) and pulsed lasers? (2023). Retrieved from https://405nm.com/difference-between-cw-and-pulsed-lasers.

[23] Lasers: Understanding the Basics, Inc., C. (2015). Retrieved from https://www.photonics.com/Articles/LasersunderstandingtheBasics/a25161

[24] Strickland, D., Mourou, G. (1985). Compression of amplified chirped optical pulses. Optics Communications, 55(6), 447–449. doi:10.1016/0030-4018(85)90151-8.

[25] Brito, J. (2023). Retrieved from https://novantaphotonics.com/brief-guide-femtosecond-lasers/

[26] Dusser, B., Sagan, Z., Soder, H., Faure, N., Colombier, J. P., Jourlin, M., Audouard, E. (2010a). Controlled nanostructrures formation by Ultra Fast Laser pulses for color marking. Optics Express, 18(3), 2913. doi:10.1364/oe.18.002913.

[27] Swinehart, D. F. (1962). The beer-lambert law. Journal of Chemical Education, 39(7), 333. doi:10.1021/ed039p333.

[28] Bévillon, E., Colombier, J. P., Recoules, V., Zhang, H., Li, C., amp; Stoian, R. (2016). Ultrafast switching of surface plasmonic conditions in nonplasmonic metals. Physical Review B, 93(16). doi:10.1103/physrevb.93.165416.

[29] Dominic, P., Bourquard, F., Reynaud, S., Weck, A., Colombier, J.-P., amp; Garrelie, F. (2021a). On the insignificant role of the oxidation process on ultrafast high-spatial-frequency LIPSS formation on Tungsten. Nanomaterials, 11(5), 1069. doi:10.3390/nano11051069.

[30] Hohlfeld, J., Wellershoff, S.-S., Güdde, J., Conrad, U., Jähnke, V., Matthias, E. (2000). Electron and lattice dynamics following optical excitation of Metals. Chemical Physics, 251(1–3), 237–258. doi:10.1016/s0301-0104(99)00330-4.

[31] Vorobyev, Anatoliy Y., Guo, C. (2012). Direct femtosecond laser surface nano/microstructuring and its applications. Laser Photonics Reviews, 7(3), 385–407. doi:10.1002/lpor.201200017.

[32] Gamaly, E. G. (2011). The physics of ultra-short laser interaction with solids at non-relativistic intensities. Physics Reports, 508(4–5), 91–243. doi:10.1016/j.physrep.2011.07.002.

[33] Glenzer, S.H., Landen, O.L., Neumayer, P., Lee, R.W., Widmann, K., Pollaine, S.W., Wallace, R.J., Gregori, G., Höll, A., Bornath, T. and Thiele, R. (2007). Observations of plasmons in warm dense matter. Physical Review Letters, 98(6). doi:10.1103/physrevlett.98.065002.

[34] Ernstorfer, R., Harb, M., Hebeisen, C. T., Sciaini, G., Dartigalongue, T., Miller, R. J. (2009). The formation of warm dense matter: Experimental evidence for electronic bond hardening in gold. Science, 323(5917), 1033–1037. doi:10.1126/science.1162697.

[35] Abou Saleh, A. (2019). Relation entre auto-organisation et création/résorption de défauts microstructuraux sous irradiation laser ultrabrèves (Doctoral dissertation, Université de Lyon).

[36] Wu, C., Zhigilei, L. V. (2013). Microscopic mechanisms of laser spallation and ablation of metal targets from large-scale molecular dynamics simulations. Applied Physics A, 114(1), 11–32. doi:10.1007/s00339-013-8086-4.

[37] Dash, J. G. (1999). History of the search for continuous melting. Reviews of Modern Physics, 71(5), 1737–1743. doi:10.1103/revmodphys.71.1737.

[38] Shugaev, M. V., He, M., Levy, Y., Mazzi, A., Miotello, A., Bulgakova, N. M., Zhigilei, L. V. (2020). Laser-induced thermal processes: Heat transfer, generation of stresses, melting and solidification, vaporization, and phase explosion. Handbook of Laser Micro- and Nano-Engineering, 1–81. doi:10.1007/978-3-319-69537-211-1.

[39] Ivanov, D. S., Zhigilei, L. V. (2007). Kinetic limit of heterogeneous melting in metals. Physical Review Letters, 98(19). doi:10.1103/physrevlett.98.195701.

[40] Ivanov, D. S., Zhigilei, L. V. (2003). Combined atomistic-continuum modeling of short-pulse laser melting and disintegration of metal films. Physical Review B, 68(6). doi:10.1103/physrevb.68.064114

[41] Leveugle, E., Ivanov, D. S., Zhigilei, L. V. (2004). Photomechanical spallation of molecular and metal targets: Molecular dynamics study. Applied Physics A, 79(7), 1643–1655. doi:10.1007/s00339-004-2682-2.

[42] Zhigilei, L. V., Garrison, B. J. (2000). Microscopic mechanisms of laser ablation of organic solids in the thermal and stress confinement irradiation regimes. Journal of Applied Physics, 88(3), 1281–1298. doi:10.1063/1.373816.

[43] Shugaev, M. V., Zhigilei, L. V. (2019). Thermodynamic analysis and atomistic modeling of sub-surface cavitation in photomechanical spallation. Computational Materials Science, 166, 311–317. doi:10.1016/j.commatsci.2019.05.017

[44] Stoian, R., Bonse, J. (2023). Ultrafast laser nanostructuring: The pursuit of extreme scales. Cham, Switzerland: Springer.ISBN: 9783031147517.

[45] Wu, C., Zhigilei, L. V. (2013a). Microscopic mechanisms of laser spallation and ablation of metal targets from large-scale molecular dynamics simulations. Applied Physics A, 114(1), 11–32. doi:10.1007/s00339-013-8086-4.

[46] Wu, C., Christensen, M. S., Savolainen, J.-M., Balling, P., Zhigilei, L. V. (2015). Generation of subsurface voids and a nanocrystalline surface layer in femtosecond laser irradiation of a single-crystal ag target. Physical Review B, 91(3). doi:10.1103/physrevb.91.035413

[47] Shugaev, M.V., He, M., Lizunov, S.A., Levy, Y., Derrien, T.J.Y., Zhukov, V.P., Bulgakova, N.M. and Zhigilei, L.V., (2018). Insights into laser-materials interaction through modeling on atomic and Macroscopic Scales. Advances in the Application of Lasers in Materials Science, 107–148. doi:10.1007/978-3-319-96845-25.

[48] Karim, E. T., Wu, C., Zhigilei, L. V. (2014). Molecular dynamics simulations of laser-materials interactions: General and material-specific mechanisms of material removal and generation of Crystal defects. Fundamentals of Laser-Assisted Micro- and Nanotechnologies, 27–49. doi:10.1007/978-3-319-05987-72.

[49] He, Miao Wu, Chengping & Shugaev, Maxim Samolyuk, German Zhigilei, Leonid.Computational Study of Short-Pulse Laser-Induced Generation of Crystal Defects in Ni-Based Single-Phase Binary Solid solution Alloys. doi:10.1021/acs.jpcc.8b09922.s004.

[50] Zhigilei, L. V., Lin, Z., Ivanov, D. S. (2009). Atomistic modeling of short pulse laser ablation of metals: Connections between melting, spallation, and phase explosion. The Journal of Physical Chemistry C, 113(27), 11892–11906. doi:10.1021/jp902294m.

[51] Sedao, X., Shugaev, M.V., Wu, C., Douillard, T., Esnouf, C., Maurice, C., Reynaud, S., Pigeon, F., Garrelie, F., Zhigilei, L.V. and Colombier, J.P., Growth twinning and generation of high-frequency surface nanostructures in ultrafast laser-induced transient melting and resolidification. ACS Nano, 10(7), 6995–7007. doi:10.1021/acsnano.6b02970.

[52] Shugaev, M.V., Wu, C., Armbruster, O., Naghilou, A., Brouwer, N., Ivanov, D.S., Derrien, T.J.Y., Bulgakova, N.M., Kautek, W., Rethfeld, B. and Zhigilei, L.V. (2016). Fundamentals of Ultrafast Laser–Material Interaction. MRS Bulletin, 41(12), 960–968. doi:10.1557/mrs.2016.274.

[53] Emmony, D. C., Howson, R. P., Willis, L. J. (1973). Laser mirror damage in germanium at 10.6 micrometer. Applied Physics Letters, 23(11), 598–600. doi:10.1063/1.1654761.

[54] Valiev, R. Z., Alexandrov, I. V., Zhu, Y. T., Lowe, T. C. (2002). Paradox of strength and ductility in metals processed Bysevere plastic deformation. Journal of Materials Research, 17(1), 5–8. doi:10.1557/jmr.2002.0002.

[55] Li C.M, James.Grain boundaries in Nanocrystalline Materials. (2011). Mechanical Properties of Nanocrystalline Materials, 205–224. ISBN: 9789814241977.

[56] Wu, C., Zhigilei, L. V. (2016). Nanocrystalline and polyicosahedral structure of a nanospike generated on metal surface irradiated by a single femtosecond laser pulse. The Journal of Physical Chemistry C, 120(8), 4438–4447. doi:10.1021/acs.jpcc.6b00013.

[57] Abou-Saleh, A., Karim, E.T., Maurice, C., Reynaud, S., Pigeon, F., Garrelie, F., Zhigilei, L.V. and Colombier, J.P.,(2018). Spallation-induced roughness promoting high spatial frequency nanostructure formation on Cr. Applied Physics A, 124(4). doi:10.1007/s00339-018-1716-0.

[58] Bonse, Jörn. (2020). Quo Vadis LIPSS?—recent and future trends on laser-induced periodic surface structures. Nanomaterials, 10(10), 1950. doi:10.3390/nano10101950.

[59] Abou Saleh, A., Rudenko, A., Reynaud, S., Pigeon, F., Garrelie, F., Colombier, J.-P. (2020). Sub-100 nm 2D nanopatterning on a large scale by Ultrafast Laser Energy Regulation. Nanoscale, 12(12), 6609–6616. doi:10.1039/c9nr09625f.

[60] Nakhoul, A., Maurice, C., Agoyan, M., Rudenko, A., Garrelie, F., Pigeon, F., Colombier, J.-P. (2021). Self-organization regimes induced by ultrafast laser on surfaces in the tens of nanometer scales. Nanomaterials, 11(4), 1020. doi:10.3390/nano11041020.

[61] Bonse, Jörn, Kirner, S., Griepentrog, M., Spaltmann, D., Krüger, J. (2018). Femtosecond laser texturing of surfaces for tribological applications. Materials, 11(5), 801. doi:10.3390/ma11050801.

[62] Schwarz, S., Rung, S., Esen, C. and Hellmann, R.(2018).Homogeneous low spatial frequency LIPSS on dielectric materials generated by beam-shaped femtosecond pulsed laser irradiation. . Journal of Laser Micro/Nanoengineering, 13(2). doi:10.2961/jlmn.2018.02.0007.

[63] Pan, A. F., Wang, W. J., Mei, X. S., Yang, H. Z., Sun, X. F. (2016). The formation mechanism and evolution of PS-laser-induced high-spatial-frequency periodic surface structures on Titanium. Applied Physics B, 123(1). doi:10.1007/s00340-016-6613-7.

[64] Raether, H. (1983). The dispersion relation of surface plasmons on rough surfaces; a comment on roughness data. Surface Science, 125(3), 624–634. doi:10.1016/s0039-6028(83)80051-x.

[65] Bonse, Jörn, Gräf, S. (2020). Maxwell meets Marangoni—a review of theories on laser-induced periodic surface structures. Laser ; Photonics Reviews, 14(10). doi:10.1002/lpor.202000215.

[66] van Driel, H. M., Sipe, J. E.,Young, J. F. (1982). Laser-induced periodic surface structure on solids: A universal phenomenon. Physical Review Letters, 49(26), 1955–1958. doi:10.1103/physrevlett.49.1955.

[67] Florian, C., Kirner, S. V., Krüger, J., Bonse, J. (2020). Surface functionalization by laser-induced periodic surface structures. Journal of Laser Applications, 32(2). doi:10.2351/7.0000103.

[68] Sipe, J. E., Young, J. F., Preston, J. S., van Driel, H. M. (1983). Laser-induced periodic surface structure. I. Theory. Physical Review B, 27(2), 1141–1154. doi:10.1103/physrevb.27.1141.

[69] Skolski, J. Z., Römer, G. R., Obona, J. V., Ocelik, V., Huis in 't Veld, A. J.,De Hosson, J. Th. (2012). Laser-induced periodic surface structures: Fingerprints of light localization. Physical Review B, 85(7). doi:10.1103/physrevb.85.075320

[70] Rudenko, A., Mauclair, C., Garrelie, F., Stoian, R., Colombier, J.-P. (2019). Amplification and regulation of periodic nanostructures in multipulse ultrashort laser-induced surface evolution by electromagnetic-hydrodynamic simulations. Physical Review B, 99(23). doi:10.1103/physrevb.99.235412.

[71] Rudenko, A., Abou-Saleh, A., Pigeon, F., Mauclair, C., Garrelie, F., Stoian, R., Colombier, J. P. (2020a). High-frequency periodic patterns driven by non-radiative fields coupled with Marangoni convection instabilities on laser-excited metal surfaces. Acta Materialia, 194, 93–105. doi:10.1016/j.actamat.2020.04.058.

[72] Kirichenko, N. A., Barmina, E. V., Shafeev, G. A. (2018). Theoretical and experimental investigation of the formation of high spatial frequency periodic structures on metal surfaces irradiated by ultrashort laser pulses. Physics of Wave Phenomena, 26(4), 264–273. doi:10.3103/s1541308x18040027.

[73] Ionin, A. A., Kudryashov, S. I., Ligachev, A. E., Makarov, S. V., Seleznev, L. V. Sinitsyn, D. V. (2011). Nanoscale cavitation instability of the surface melt along the grooves of one-dimensional nanorelief gratings on an aluminum surface. JETP Letters, 94(4), 266–269. doi:10.1134/s0021364011160065.

[74] Sedao, X., Abou Saleh, A., Rudenko, A., Douillard, T., Esnouf, C., Reynaud, S., Maurice, C., Pigeon, F., Garrelie, F. and Colombier (2018). Self-arranged periodic nanovoids by ultrafast laser-induced near-field enhancement. ACS Photonics, 5(4), 1418–1426. doi:10.1021/acsphotonics.7b01438.

[75] Skolski, J. Z., Römer, G. R., Vincenc Obona, J., Huis in 't Veld, A. J. (2014). Modeling laser-induced periodic surface structures: Finite-difference time-domain feedback simulations. Journal of Applied Physics, 115(10). doi:10.1063/1.4867759.

[76] Déziel, J., Dumont, J., Gagnon, D., Dubé, L. J., Messaddeq, S. H., Messaddeq, Y. (2016). Constructive feedback for the growth of laser-induced periodic surface structures. Physica Status Solidi c, 13(2–3), 121–124. doi:10.1002/pssc.201510146.

[77] Rudenko, A., Mauclair, C., Garrelie, F., Stoian, R., Colombier, J. P. (2019). Light absorption by surface nanoholes and nanobumps. Applied Surface Science, 470, 228–233. doi:10.1016/j.apsusc.2018.11.111.

[78] Skolski, J. Z. (2010). Modeling of laser induced periodic surface structures. Journal of Laser Micro/Nanoengineering, 5(3), 263–268. doi:10.2961/jlmn.2010.03.0015.

[79] Tsibidis, G. D., Barberoglou, M., Loukakos, P. A., Stratakis, E., Fotakis, C. (2012). Dynamics of Ripple Formation on silicon surfaces by ultrashort laser pulses in subablation conditions. Physical Review B, 86(11). doi:10.1103/physrevb.86.115316.

[80] Schade, M., Varlamova, O., Reif, J., Blumtritt, H., Erfurth, W., Leipner, H. S. (2009). High-resolution investigations of ripple structures formed by femtosecond laser irradiation of silicon. Analytical and Bioanalytical Chemistry, 396(5), 1905–1911. doi:10.1007/s00216-009-3342-3.

[81] Chen, X. Y., Lin, J., Liu, J. M., Liu, Z. G. (2008). Formation and evolution of self-organized hexagonal patternssilicon surface by laser irradiation in water. Applied Physics A, 94(3), 649–656. doi:10.1007/s00339-008-4894-3.

[82] Ursu, I., Dorobantu, I.A., Mihailescu, I.N., Vlad, M., Spineanu, F., Prokhorov, A.M., Konov, V.I. and Tokarev, V.N (1989). Possible mechanism for laser-induced two-dimensional periodic structures by analogy with the Bénard effect. Optics Letters, 14(16), 853. doi:10.1364/ol.14.000853.

[83] Gurevich, E. L. (2011). Self-organized nanopatterns in thin layers of superheated liquid metals. Physical Review E, 83(3). doi:10.1103/physreve.83.031604.

[84] Romano, J.-M., Garcia-Giron, A., Penchev, P., Dimov, S. (2018). Triangular laser-induced submicron textures for functionalising stainless steel surfaces. Applied Surface Science, 440, 162–169. doi:10.1016/j.apsusc.2018.01.086.

[85] Emel'yanov, V. I. (2008). Self-organization of ordered nano- and microstructures on the semiconductor surface under the action of Laser Radiation. Laser Physics, 18(6), 682–718. doi:10.1134/s1054660x08060029.

[86] Reif, J., Costache, F.,Bestehorn, M. (2006). Self-organized surface nanostructuring by femtosecond laser processing. Recent Advances in Laser Processing of Materials, 275–290. doi:10.1016/b978-008044727-8/50010-9.

[87] Varlamova, O., Costache, F., Reif, J., Bestehorn, M. (2006). Self-organized pattern formation upon femtosecond laser ablation by circularly polarized light. Applied Surface Science, 252(13), 4702–4706. doi:10.1016/j.apsusc.2005.08.120.

[88] Öktem, B., Pavlov, I., Ilday, S., Kalaycıoğlu, H., Rybak, A., Yavaş, S., Erdoğan, M. and Ilday, F.Ö., Nonlinear laser lithography for indefinitely large-area nanostructuring with femtosecond pulses. Nature Photonics, 7(11), 897–901. doi:10.1038/nphoton.2013.272.

[89] Dostovalov, A. V., Korolkov, V. P., Babin, S. A. (2015). Simultaneous formation of ablative and thermochemical laser-induced periodic surface structures on ti film at Femtosecond irradiation. Laser Physics Letters, 12(3), 036101. doi:10.1088/1612-2011/12/3/036101.

[90] Dostovalov, A. V., Korolkov, V. P., Terentyev, V. S., Okotrub, K. A., Dultsev, F. N., Babin, S. A. (2017). Study of the formation of thermochemical laser-induced periodic surface structures on cr, ti, Ni and NICR films under femtosecond irradiation. Quantum Electronics, 47(7), 631–637. doi:10.1070/qel16379.

[91] Dostovalov, A.V., Derrien, T.J.Y., Lizunov, S.A., Přeučil, F., Okotrub, K.A., Mocek, T., Korolkov, V.P., Babin, S.A. and Bulgakova, N.M., (2019a). LIPSS on thin metallic films: New insights from multiplicity of laser-excited electromagnetic modes and efficiency of metal oxidation. Applied Surface Science, 491, 650–658. doi:10.1016/j.apsusc.2019.05.171.

[92] Florian, C., Déziel, J.-L., Kirner, S., Siegel, J.,Bonse, J. (2020). The role of the laser-induced oxide layer in the formation of laser-induced periodic surface structures. Nanomaterials, 10(1), 147. doi:10.3390/nano10010147.

[93] Xie, H., Zhao, B., Lei, Y., Yu, Z., Cheng, J., Yang, J. (2021). Oxidation ruled transition from normal to anomalous periodic structures with femtosecond laser irradiation on CR/Si Films. Optics Express, 29(20), 31408. doi:10.1364/oe.433035.

[94] Kane Yee. (1966). Numerical solution of initial boundary value problems involving Maxwell's equations in isotropic media. IEEE Transactions on Antennas and Propagation, 14(3), 302–307. doi:10.1109/tap.1966.1138693.

[95] Zhang, H., Colombier, J.-P., Li, C., Faure, N., Cheng, G., Stoian, R. (2015). Coherence in ultrafast laser-induced periodic surface structures. Physical Review B, 92(17).doi:10.1103/physrevb.92.174109.

[96] Djouder, M., Itina, T. E., Deghiche, D., Lamrous, O. (2012). Modelling the formation of nanostructures on metal surface induced by femtosecond laser ablation. Applied Surface Science, 258(7), 2580–2583. doi:10.1016/j.apsusc.2011.10.097.

[97] Djouder, M., Lamrous, O., Mitiche, M. D., Itina, T. E., Zemirli, M. (2013). Electromagnetic particle-in-cell (PIC) method for modeling the formation of metal surface structures induced by femtosecond laser radiation. Applied Surface Science, 280, 711–714. doi:10.1016/j.apsusc.2013.05.047.

[98] Russell, A., Schumacher, D. W. (2017). First principles simulation of the dynamics of transient warm dense matter during the formation of ultrashort laser pulse induced damage using the particle-in-cell method. Laser-Induced Damage in Optical Materials 2017. doi:10.1117/12.2280543.

[99] Wang, B., Wang, Y., Song, H., Cheong Lam, Y., Memara Shaymaa, E., Liu, S. (2023). Threshold effect on the femtosecond laser-induced periodic subwavelength structure: An analytical approach. Optics Laser Technology, 158, 108804. doi:10.1016/j.optlastec.2022.108804.

[100] Miloshevsky, G. (2022). Ultrafast laser matter interactions: Modeling approaches, challenges, and prospects. Modelling and Simulation in Materials Science and Engineering, 30(8), 083001. doi:10.1088/1361-651x/ac8abc.

[101] Lin, Z., Zhigilei, L. V.,Celli, V. (2008a). Electron-phonon coupling and electron heat capacity of metals under conditions of strong electron-phonon nonequilibrium. Physical Review B, 77(7). doi:10.1103/physrevb.77.075133.

[102] Carpene, E. (2006). Ultrafast laser irradiation of metals: Beyond the two-temperature model. Physical Review B, 74(2). doi:10.1103/physrevb.74.024301.

[103] Colombier, J. P., Combis, P., Bonneau, F., Le Harzic, R., Audouard, E. (2005). Hydrodynamic simulations of metal ablation by femtosecond laser irradiation. Physical Review B, 71(16). doi:10.1103/physrevb.71.165406.

[104] Anisimov, S. I., Kapeliovich, B. L., & Perelman, T. L. (1974). Electron emission from metal surfaces exposed to ultrashort laser pulses.Bibcode:1974ZhETF..66..776A.

[105] Duarte, M., Lasagni, A., Giovanelli, R., Narciso, J., Louis, E., amp; Mücklich, F. (2008). Increasing lubricant film lifetime by grooving periodical patterns using laser interference metallurgy. Advanced Engineering Materials, 10(6), 554–558. doi:10.1002/adem.200700321.

[106] Gurevich, Evgeny L., Levy, Y., Gurevich, S. V., Bulgakova, N. M. (2017). Role of the temperature dynamics in formation of nanopatterns upon single femtosecond laser pulses on gold. Physical Review B, 95(5). doi:10.1103/physrevb.95.054305.

[107] Levy, Y., Derrien, T. J.-Y., Bulgakova, N. M., Gurevich, E. L., amp; Mocek, T. (2016). Relaxation Dynamics of femtosecond-laser-induced temperature modulation on the surfaces of metals and semiconductors. Applied Surface Science, 374, 157–164. doi:10.1016/j.apsusc.2015.10.159

[108] Bonse, Jörn, Höhm, S., Kirner, S., Rosenfeld, A., Krüger, J. (2016). Laser-induced periodic surface structures (LIPSS) – a scientific evergreen. Conference on Lasers and Electro-Optics. doi:10.1364/cleo-si.2016.sth1q.3.

[109] Alder, B. J., Wainwright, T. E. (1959). Studies in molecular dynamics. I. General Method. The Journal of Chemical Physics, 31(2), 459–466. doi:10.1063/1.1730376.

[110] Inogamov, N.A., Zhakhovskii, V.V., Ashitkov, S.I., Khokhlov, V.A., Petrov, Y.V., Komarov, P.S., Agranat, M.B., Anisimov, S.I. and Nishihara, K., (2009). Two-temperature relaxation and melting after absorption of femtosecond laser pulse. Applied Surface Science, 255(24), 9712–9716. doi:10.1016/j.apsusc.2009.04.139.

[111] Ivanov, D.S., Lipp, V.P., Blumenstein, A., Kleinwort, F., Veiko, V.P., Yakovlev, E., Roddatis, V., Garcia, M.E., Rethfeld, B., Ihlemann, J. and Simon, P., (2015). Experimental and theoretical investigation of periodic nanostructuring of au with ultrashort UV laser pulses near the damage threshold. Physical Review Applied, 4(6). doi:10.1103/physrevapplied.4.064006.

[112] Gnilitskyi, I., Shugaev, M. V., White, T., Zhigilei, L. V. (2018). Mechanism of single-pulse ablative generation of laser-induced periodic surface structures. Conference on Lasers and Electro-Optics. doi:10.1364/cleoat.2018.jtu3o.1.

[113] Bonse, J., Koter, R., Hartelt, M., Spaltmann, D., Pentzien, S., Höhm, S., Rosenfeld, A. and Krüger (2014a). Femtosecond laser-induced periodic surface structures on steel and titanium alloy for tribological applications. Applied Physics A, 117(1), 103–110. doi:10.1007/s00339-014-8229-2.

[114] Wang, Z., Zhao, Q.,Wang, C. (2015). Reduction of friction of metals using laser-induced periodic surface nanostructures. Micromachines, 6(11), 1606–1616. doi:10.3390/mi6111444.

[115] Voyer, J., Ausserer, F., Klien, S., Ristow, A., Velkavrh, I., Diem, A., Zehetner, J., Heidegger, S., Bertschler, C., Edlinger, J. and Stroj, S., (2017). Sub-micro laser modifications of tribological surfaces. Materials Performance and Characterization, 6(2). doi:10.1520/mpc20160015.

[116] Florian, C., Wonneberger, R., Undisz, A., Kirner, S.V., Wasmuth, K., Spaltmann, D., Krüger, J. and Bonse, J., (2020). Chemical effects during the formation of various types of femtosecond laser-generated surface structures on titanium alloy. Applied Physics A, 126(4). doi:10.1007/s00339-020-3434-7.

[117] Borcherding, K., Marx, D., Gätjen, L., Specht, U., Salz, D., Thiel, K., Wildemann, B. and Grunwald, I., (2020). Impact of laser structuring on medical-grade titanium: Surface characterization and in vitro evaluation of osteoblast attachment. Materials, 13(8), 2000. doi:10.3390/ma13082000.

[118] Raimbault, O., Benayoun, S., Anselme, K., Mauclair, C., Bourgade, T., Kietzig, A.M., Girard-Lauriault, P.L., Valette, S. and Donnet, C., (2016). The effects of femtosecond laser-textured ti-6al-4v on wettability and cell response. Materials Science and Engineering: C, 69, 311–320. doi:10.1016/j.msec.2016.06.072.

[119] Luo, X., Yao, S., Zhang, H., Cai, M., Liu, W., Pan, R., Chen, C., Wang, X., Wang, L. and Zhong, M. (2020). Biocompatible nano-ripples structured surfaces induced by femtosecond laser to rebel bacterial colonization and Biofilm Formation. Optics Laser Technology, 124, 105973. doi:10.1016/j.optlastec.2019.105973.

[120] Liu, N., Sun, Y., Wang, H., Liang, C. (2021). Femtosecond laser-induced nanostructures on FE-30MN surfaces for biomedical applications. Optics Laser Technology, 139, 106986. doi:10.1016/j.optlastec.2021.106986.

[121] Yang, J., Yang, Y., Zhao, B., Wang, Y.,Zhu, X. (2011). Femtosecond laser-induced surface structures to significantly improve the thermal emission of light from metals. Applied Physics B, 106(2), 349–355. doi:10.1007/s00340-011-4834-3.

[122] Vorobyev, A. Y., Makin, V. S.,Guo, C. (2009). Brighter light sources from black metal: Significant increase in emission efficiency of incandescent light sources. Physical Review Letters, 102(23). doi:10.1103/physrevlett.102.234301.

[123] Dai, Y., He, M., Bian, H., Lu, B., Yan, X.,Ma, G. (2011). Femtosecond laser nanostructuring of silver film. Applied Physics A, 106(3), 567–574. doi:10.1007/s00339-011-6705-5.

[124] Chang, H.-W., Tsai, Y.-C., Cheng, C.-W., Lin, C.-Y., Lin, Y.-W., Wu, T.-M. (2011). Nanostructured AG surface fabricated by femtosecond laser for surface-enhanced Raman scattering. Journal of Colloid and Interface Science, 360(1), 305–308. doi:10.1016/j.jcis.2011.04.005.

[125] Karthikeyan, A., Coulombe, S., Kietzig, A. M. (2018). Boiling heat transfer enhancement with stable nanofluids and laser textured copper surfaces. International Journal of Heat and Mass Transfer, 126, 287–296. doi:10.1016/j.ijheatmasstransfer.2018.05.118.

[126] Abderazek, Talbi. (2017). Effect of ultra-short laser nanostructuring of material surfaces on the evolution of their thermoelectric properties.E-MRS 2017 Spring Meeting (Symposium H).

[127] Vorobyev, A. Y., Guo, C. (2013). Nanochemical effects in femtosecond laser ablation of metals. Applied Physics Letters, 102(7). doi:10.1063/1.4793521.

[128] Chuang, T. J. (1983). Laser-induced gas-surface interactions. Surface Science Reports, 3(1), 1–105. doi:10.1016/0167-5729(83)90005-5.

[129] Chuang, T. J. (1982). Laser-enhanced gas–surface chemistry: Basic processes and applications. Journal of Vacuum Science and Technology, 21(3), 798–806. doi:10.1116/1.571827.

[130] Chuang, T. J. (1980). Electron spectroscopy study of silicon surfaces exposed to XEF2 and the chemisorption of SIF4 on Silicon. Journal of Applied Physics, 51(5), 2614–2619. doi:10.1063/1.327990.

[131] Schafer, S. A.,Lyon, S. A. (1982). Wavelength dependence of laser-enhanced oxidation of silicon. Journal of Vacuum Science and Technology, 21(2), 422–425. doi:10.1116/1.571669.

[132] Petro, W. G., Hino, I., Eglash, S., Lindau, I., Su, C. Y., amp; Spicer, W. E. (1982). Effect of low-intensity laser radiation during oxidation of the gaas(110) surface. Journal of Vacuum Science and Technology, 21(2), 405–408. doi:10.1116/1.571665.

[133] Lahoz, R., Espinós, J. P., Yubero, F., González-Elipe, A. R., amp; de la Fuente, G. F. (2015). "In situ" XPS studies of laser-induced surface nitridation and oxidation of tantalum. Journal of Materials Research, 30(19), 2967–2976. doi:10.1557/jmr.2015.190.

[134] NIKITIN, P. I., UGLOV, S. A., KONOV, V. I. (1991). Pulsed laser plasmotrons. Le Journal de Physique IV, 01(C7). doi:10.1051/jp4:1991738.

[135] Hammouti, S., Holybee, B., Zhu, W., Allain, J. P., Jurczyk, B., amp; Ruzic, D. N. (2018). Titanium nitride formation by a dual-stage femtosecond laser process. Applied Physics A, 124(6). doi:10.1007/s00339-018-1824-x.

[136] Ohtsu, N., Kodama, K., Kitagawa, K., Wagatsuma, K. (2010). Comparison of surface films formed on Titanium by pulsed nd:YAG laser irradiation at different powers and wavelengths in nitrogen atmosphere. Applied Surface Science, 256(14), 4522–4526. doi:10.1016/j.apsusc.2010.02.040.

[137] Joy, N.,Kietzig, A.-M. (2023). Role of machining and exposure conditions on the surface chemistry modification of femtosecond laser-machined copper surfaces. Surfaces and Interfaces, 37, 102657. doi:10.1016/j.surfin.2023.102657.

[138] Adams, D. P., Murphy, R. D., Saiz, D. J., Hirschfeld, D. A., Rodriguez, M. A., Kotula, P. G.,Jared, B. H. (2014). Nanosecond pulsed laser irradiation of titanium: Oxide growth and effects on underlying metal. Surface and Coatings Technology, 248, 38–45. doi:10.1016/j.surfcoat.2013.12.052.

[139] Li, X., Yuan, C., Yang, H., Li, J., Huang, W., Tang, D., Xu, Q. (2010). Morphology and composition on al surface irradiated by femtosecond laser pulses. Applied Surface Science, 256(13), 4344–4349. doi:10.1016/j.apsusc.2010.02.029.

[140] Balchev, I., Minkovski, N., Marinova, Ts., Shipochka, M., Sabotinov, N. (2006). Composition and structure characterization of aluminum after laser ablation. Materials Science and Engineering: B, 135(2), 108–112. doi:10.1016/j.mseb.2006.08.042.

[141] Kirner, S. V., Wirth, T., Sturm, H., Krüger, J., Bonse, J. (2017a). Nanometer-resolved chemical analyses of femtosecond laser-induced periodic surface structures on Titanium. Journal of Applied Physics, 122(10), 104901. doi:10.1063/1.4993128.

[142] Kietzig, A.-M., Hatzikiriakos, S. G., Englezos, P. (2009). Patterned superhydrophobic metallic surfaces. Langmuir, 25(8), 4821–4827. doi:10.1021/la8037582.

[143] Long, J., Zhong, M., Zhang, H., Fan, P. (2015). Superhydrophilicity to superhydrophobicity transition of picosecond laser microstructured aluminum in ambient air. Journal of Colloid and Interface Science, 441, 1–9. doi:10.1016/j.jcis.2014.11.015.

[144] Yang, Z., Liu, X., Tian, Y. (2019). Corrigendum to "insights into the wettability transition of nanosecond laser ablated surface under ambient air exposure" [J. colloid interface sci. 533 (2019) 268–277]. Journal of Colloid and Interface Science, 539, 672. doi:10.1016/j.jcis.2018.11.090.

[145] Long, J., Fan, P., Gong, D., Jiang, D., Zhang, H., Li, L. Zhong, M. (2015). Superhydrophobic surfaces fabricated by femtosecond laser with tunable water adhesion: From Lotus Leaf to Rose Petal. ACS Applied Materials Interfaces, 7(18), 9858–9865. doi:10.1021/acsami.5b01870.

[146] Giannuzzi, G., Gaudiuso, C., Di Mundo, R., Mirenghi, L., Fraggelakis, F., Kling, R., ... Ancona, A. (2019). Short and long term surface chemistry and wetting behaviour of stainless steel with 1D and 2D periodic structures induced by bursts of femtosecond laser pulses. Applied Surface Science, 494, 1055–1065. doi:10.1016/j.apsusc.2019.07.126.

[147] Yan, H., Abdul Rashid, M. R., Khew, S. Y., Li, F.,Hong, M. (2018). Wettability transition of laser textured brass surfaces inside different mediums. Applied Surface Science, 427, 369–375. doi:10.1016/j.apsusc.2017.08.218.

[148] Kietzig, A.-M., Negar Mirvakili, M., Kamal, S., Englezos, P., Hatzikiriakos, S. G. (2011). Laser-patterned super-hydrophobic pure metallic substrates: Cassie to Wenzel Wetting Transitions. Journal of Adhesion Science and Technology, 25(20), 2789–2809. doi:10.1163/016942410x549988.

[149] Gregorčič,P. Comment on Bioinspired Reversible Switch between Underwater Superoleophobicity/Superaerophobicity and Oleophilicity/Aerophilicity and Improved Antireflective Property on the Nanosecond Laser-Ablated Superhydrophobic Titanium Surfaces. doi:10.1021/acsami.9b23462.s001.

[150] Pou, P., Del Val, J., Riveiro, A., Comesaña, R., Arias-González, F., Lusquiños, F., Bountinguiza, M., Quintero, F. and Pou, J., (2019). Laser texturing of stainless steel under different processing atmospheres: From superhydrophilic to superhydrophobic surfaces. Applied Surface Science, 475, 896–905. doi:10.1016/j.apsusc.2018.12.248.

[151] Cheng, H.-C., Jiang, Z.-X., Chang, T.-L., Chen, P.-H. (2020). Roughness and wettability properties of plain and silica-coated copper surfaces textured with picosecond laser. Applied Surface Science, 514, 145918. doi:10.1016/j.apsusc.2020.145918.

[152] Exir, H., Weck, A. (2019). Mechanism of superhydrophilic to superhydrophobic transition of femtosecond laser-induced periodic surface structures on Titanium. Surface and Coatings Technology, 378, 124931. doi:10.1016/j.surfcoat.2019.124931.

[153] Jwad, T., Walker, M., Dimov, S. (2018). Erasing and rewriting of titanium oxide colour marks using laser-induced reduction/oxidation. Applied Surface Science, 458, 849–854. doi:10.1016/j.apsusc.2018.07.152.

[154] Killaire, G., Walia, J., Rashid, S., Berini, P., Weck, A. (2022). Structural and oxide-based colours on laser textured copper. Applied Surface Science, 583, 152440. doi:10.1016/j.apsusc.2022.152440

[155] Nánai, L., Vajtai, R., F. George, T. (1997). Laser-induced oxidation of metals: State of the art. Thin Solid Films, 298(1–2), 160–164. doi:10.1016/s0040-6090(96)09390-x.

[156] CABRERA, N., MOTT, N. F. (1995). Theory of the oxidation of metals. World Scientific Series in 20th Century Physics, 185–207. doi:10.1142/9789812794086-0016.

[157] Xia, F., Jiao, L., Wu, D., Li, S., Zhang, K., Kong, W., Yun, M., Liu, Q. and Zhang, (2019a). Mechanism of pulsed-laser-induced oxidation of titanium films. Optical Materials Express, 9(10), 4097. doi:10.1364/ome.9.004097.

[158] Wagner, C. (1933). Contributions to the Theory of the Tarnishing Process. Z. Phys. Chem. B, 21, 25. Accession Number: AD0805602.

[159] Lian, J., Dong, Q., Guo, Z., Xu, Q., Yang, J., Hu, J., Guan, Q. and Chen, B., (2005). Surface oxidation kinetics of CR film by Nd-YAG Laser. Materials Science and Engineering: A, 391(1–2), 210–220. doi:10.1016/j.msea.2004.08.077.

[160] Dostovalov, A.V., Derrien, T.J.Y., Lizunov, S.A., Přeučil, F., Okotrub, K.A., Mocek, T., Korolkov, V.P., Babin, S.A. and Bulgakova, N.M., (2019). LIPSS on thin metallic films: New insights from multiplicity of laser-excited electromagnetic modes and efficiency of metal oxidation. Applied Surface Science, 491, 650–658. doi:10.1016/j.apsusc.2019.05.171.

[161] Ursu, I., Nanu, L., Mihăilescu, I. N. (1986a). Diffusion model for the laser oxidation of metallic samples in air. Applied Physics Letters, 49(2), 109–111. doi:10.1063/1.97401.

[162] Pereira, A., Delaporte, P., Sentis, M., Cros, A., Marine, W., Basillais, A., Thomann, A.L., Leborgne, C., Semmar, N., Andreazza, P. and Sauvage, T.,(2004). Laser treatment of a steel surface in ambient air. Thin Solid Films, 453–454, 16–21. doi:10.1016/j.tsf.2003.11.072.

[163] Zeng, C., Wen, H., Zhang, B., Sprunger, P. T., Guo, S. M. (2020). Diffusion of oxygen and nitrogen into titanium under laser irradiation in air. Applied Surface Science, 505, 144578. doi:10.1016/j.apsusc.2019.144578.

[164] Wautelet, M. (1990a). Laser-assisted reaction of metals with oxygen. Applied Physics A Solids and Surfaces, 50(2), 131–139. doi:10.1007/bf00343408.

[165] Kotsedi, L., Furlan, V., Bharadwaj, V., Kaviyarasu, K., Sotillo, B., Mtshali, C.B., Matinise, N., Demir, A.G., Previtali, B., Ramponi, R. and Eaton, S.M., (2019). Chromium oxide formation on nanosecond and femtosecond laser irradiated thin chromium films. Optical Materials, 95, 109206. doi:10.1016/j.optmat.2019.109206.

[166] Dostovalov, A. V., Korolkov, V. P., Okotrub, K. A., Bronnikov, K. A., Babin, S. A. (2018a). Oxide composition and period variation of thermochemical LIPSS on chromium films with different thickness. Optics Express, 26(6), 7712. doi:10.1364/oe.26.007712.

[167] Zuhlke, C. A., Anderson, T. P., Alexander, D. R. (2013a). Comparison of the structural and chemical composition of two unique micro/nanostructures produced by femtosecond laser interactions on nickel. Applied Physics Letters, 103(12). doi:10.1063/1.4821452.

[168] Peng, E., Bell, R., Zuhlke, C. A., Wang, M., Alexander, D. R., Gogos, G., Shield, J. E. (2017). Growth mechanisms of multiscale, mound-like surface structures on titanium by femtosecond laser processing. Journal of Applied Physics, 122(13). doi:10.1063/1.4990709.

[169] Li, G., Li, J., Li, X., Zhu, Z., Hu, Y., Chu, J., Huang, W. (2013). Evolution of titanium surfaces irradiated by femtosecond laser pulses with different wavelengths. SPIE Proceedings. doi:10.1117/12.2021098.

[170] Zhang, D., Sugioka, K. (2019). Hierarchical microstructures with high spatial frequency laser induced periodic surface structures possessing different orientations created by femtosecond laser ablation of silicon in liquids. Opto-Electronic Advances, 2(3), 19000201–19000218. doi:10.29026/oea.2019.190002.

[171] Yang, J., Chen, X., Liu, X., Cao, Y., Huang, J., Li, Y., Liu, F. (2021). From hexagonal to monoclinic: Engineering crystalline phase to boost the intrinsic catalytic activity of tungsten oxides for the hydrogen evolution reaction. ACS Sustainable Chemistry Engineering, doi:10.1021/acssuschemeng.1c00485.

[172] Nandiyanto, A. B., Oktiani, R., Ragadhita, R., Sukmafitri, A., amp; Zaen, R. (2020). Amorphous content on the photocatalytic performance of micrometer-sized tungsten trioxide particles. Arabian Journal of Chemistry,doi:10.1016/j.arabjc.2018.07.021

[173] Tungsten. Retrieved from https://www.britannica.com/science/tungsten-chemical-element

[174] Ramana, C. V., Utsunomiya, S., Ewing, R. C., Julien, C. M., Becker, U. (2006). Structural stability and phase transitions in wo3 thin films. The Journal of Physical Chemistry B, 110(21), 10430–10435. doi:10.1021/jp056664i.

[175] Thummavichai, K., Wang, N., Xu, F., Rance, G., Xia, Y., Zhu, Y. (2018). in situinvestigations of the phase change behaviour of tungsten oxide nanostructures. Royal Society Open Science, 5(4), 171932. doi:10.1098/rsos.171932.

[176] Mardare, C. C., Hassel, A. W. (2019). Review on the versatility of tungsten oxide coatings. Physica Status Solidi (a), 216(12). doi:10.1002/pssa.201900047.

[177] Migas, D. B., Shaposhnikov, V. L., Borisenko, V. E. (2010). Tungsten oxides. II. the metallic nature of Magnéli Phases. Journal of Applied Physics, 108(9). doi:10.1063/1.3505689.

[178] Fehlner, F. P., Mott, N. F. (1970). Low-temperature oxidation. Oxidation of Metals, 2(1), 59–99. doi:10.1007/bf00603582.

[179] Cifuentes, S. C., Monge, M. A., Pérez, P. (2012). On the oxidation mechanism of pure tungsten in the temperature range 600–800°C. Corrosion Science, 57, 114–121. doi:10.1016/j.corsci.2011.12.027.

[180] Barth, V. D., P., R. G. W. (1961). Oxidation of tungsten. Columbus, OH: Defense Metals Information Center, Battelle Memorial Institute.

[181] Gulbransen, E. A., Andrew, K. F., Brassart, F. A. (1964). Kinetics of oxidation of pure tungsten, 1150°–L615°C. Journal of The Electrochemical Society, 111(1), 103. doi:10.1149/1.2426043.

[182] Sakun Duwal, Minseob Kim, and Choong-Shik Yoo. Seven-coordinated metallic WO3 at High Pressures. doi:10.1021/acs.jpcc.0c09005.s001.

[183] Bouvier, P., Crichton, W. A., Boulova, M., Lucazeau, G. (2002). X-ray diffraction study of WO3 at high pressure. Journal of Physics: Condensed Matter, 14(26), 6605–6617. doi:10.1088/0953-8984/14/26/301.

[184] Boulova, M. (2002). Crystallite nanosize effect on the structural transitions of WO3 studied by Raman spectroscopy. Journal of Solid State Chemistry, 167(2), 425–434. doi:10.1016/s0022-4596(02)99649-0.

[185] Pagnier, T., Pasturel, A. (2003). Anab initiostudy of WO3 under pressure up to 30 GPA. Journal of Physics: Condensed Matter, 15(19), 3121–3133. doi:10.1088/0953-8984/15/19/313.

[186] EDS spectra of W. Retrieved from https://www.globalsino.com/EM/page3109.html

[187] Liu, J. M. (1982). Simple technique for measurements of pulsed gaussian-beam spot sizes. Optics Letters, 7(5), 196. doi:10.1364/ol.7.000196.

[188] Retrieved from http://web.iyte.edu.tr/ serifeyalcin/lectures/chem502/L8

[189] Retrieved from https://commons.wikimedia.org/wiki/File:Electron-matter interaction volume and various types of signal generated-v2.svg

[190] SEM resolution. Retrieved from https://www.thermofisher.com/in/en/home/materials-science/learning-center/applications/sem-resolution.html

[191] Leng, Y. (2013). Materials characterization introduction to microscopic and spectroscopic methods. Weinheim: J. Wiley.

[192] Retrieved from https://nanoscience.gatech.edu/zlwang/research/afm.html

[193] Retrieved from mvascientificconsultants.com/tem-imaging-of-nanomaterials

[194] Retrieved from https://www.ircelyon.univ-lyon1.fr/en/syrcel-en/card/TEP/

[195] Law, K.-Y. (2014). Definitions for hydrophilicity, hydrophobicity, and superhydrophobicity: Getting the basics right. The Journal of Physical Chemistry Letters, 5(4), 686–688. doi:10.1021/jz402762h.

[196] Schneider, C. A., Rasband, W. S., Eliceiri, K. W. (2012). NIH image to imagej: 25 years of image analysis. Nature Methods, 9(7), 671–675. doi:10.1038/nmeth.2089.

[197] Kawakami, Y., Ozawa, E., Sasaki, S. (1999). Coherent array of tungsten ultrafine particles by laser irradiation. Applied Physics Letters, 74(26), 3954–3956. doi:10.1063/1.124248.

[198] Kawakami, Y., Ozawa, E. (2000). Self-assembled coherent array of ultra-fine particles on single-crystal tungsten substrate using SHG Nd:YAG Laser. Applied Physics A: Materials Science Processing, 71(4), 453–456. doi:10.1007/s003390000581.

[199] Kuznetsov, A. I., Unger, C., Koch, J., Chichkov, B. N. (2012). Laser-induced jet formation and droplet ejection from thin metal films. Applied Physics A, 106(3), 479–487. doi:10.1007/s00339-011-6747-8.

[200] Ivanov, Dmitriy S., Rethfeld, B., O'Connor, G. M., Glynn, T. J., Volkov, A. N., Zhigilei, L. V. (2008). The mechanism of nanobump formation in femtosecond pulse laser nanostructuring of thin metal films. Applied Physics A, 92(4), 791–796. doi:10.1007/s00339-008-4712-y.

[201] Nakhoul, A., Rudenko, A., Maurice, C., Reynaud, S., Garrelie, F., Pigeon, F., Colombier, J. (2022). Boosted spontaneous formation of high-aspect ratio Nanopeaks on ultrafast laser-irradiated ni surface. Advanced Science, 9(21). doi:10.1002/advs.202200761.

[202] Rudenko, A., Abou-Saleh, A., Pigeon, F., Mauclair, C., Garrelie, F., Stoian, R., Colombier, J. P. (2020a). High-frequency periodic patterns driven by non-radiative fields coupled with Marangoni convection instabilities on laser-excited metal surfaces. Acta Materialia, 194, 93–105. doi:10.1016/j.actamat.2020.04.058.

[203] Slowinski, E. J., Gates, E. E., Waring, C. E. (1957). The effect of pressure on the surface tensions of liquids. The Journal of Physical Chemistry, 61(6), 808–810. doi:10.1021/j150552a028.

[204] Bévillon, E., Colombier, J. P., Recoules, V., Zhang, H., Li, C., Stoian, R. (2016a). Ultrafast switching of surface plasmonic conditions in nonplasmonic metals. Physical Review B, 93(16). doi:10.1103/physrevb.93.165416.

[205] Colombier, J.P., Rudenko, A., Silaeva, E., Zhang, H., Sedao, X., Bévillon, E., Reynaud, S., Maurice, C., Pigeon, F., Garrelie, F. and Stoian, R., (2020). Mixing periodic topographies and structural patterns on silicon surfaces mediated by ultrafast photoexcited charge carriers. Physical Review Research, 2(4). doi:10.1103/physrevresearch.2.043080.

[206] Sedao, X., Maurice, C., Garrelie, F., Colombier, J.-P., Reynaud, S., Quey, R., Pigeon, F. (2014). Influence of crystal orientation on the formation of femtosecond laser-induced periodic surface structures and lattice defects accumulation. Applied Physics Letters, 104(17). doi:10.1063/1.4874626.

[207] Tsibidis, George D., Fotakis, C., Stratakis, E. (2015). From ripples to spikes: A hydrodynamical mechanism to interpret femtosecond laser-induced self-assembled structures. Physical Review B, 92(4). doi:10.1103/physrevb.92.041405.

[208] Savolainen, J.-M., Christensen, M. S., Balling, P. (2011). Material swelling as the first step in the ablation of metals by ultrashort laser pulses. Physical Review B, 84(19). doi:10.1103/physrevb.84.193410.

[209] Sedao, X., Abou Saleh, A., Rudenko, A., Douillard, T., Esnouf, C., Reynaud, S., Maurice, C., Pigeon, F., Garrelie, F. and Colombier,J.P. (2018a). Self-arranged periodic nanovoids by ultrafast laser-induced near-field enhancement. ACS Photonics, 5(4), 1418–1426. doi:10.1021/acsphotonics.7b01438.

[210] Zhigilei, L. V., Kodali, P. B., Garrison, B. J. (1997). Molecular dynamics model for laser ablation and desorption of organic solids. The Journal of Physical Chemistry B, 101(42), 8624–8624. doi:10.1021/jp972527c.

[211] Duff, W. H., Zhigilei, L. V. (2007). Computational study of cooling rates and recrystallization kinetics in short pulse laser quenching of metal targets. Journal of Physics: Conference Series, 59, 413–417. doi:10.1088/1742-6596/59/1/088.

[212] Retrieved from https://docs.lammps.org/fix-ttm.html

[213] Duffy, D. M., Rutherford, A. M. (2006). Including the effects of electronic stopping and electron–ion interactions in radiation damage simulations. Journal of Physics: Condensed Matter, 19(1), 016207. doi:10.1088/0953-8984/19/1/016207.

[214] Rutherford, A. M., Duffy, D. M. (2007). The effect of electron–ion interactions on radiation damage simulations. Journal of Physics: Condensed Matter, 19(49), 496201. doi:10.1088/0953-8984/19/49/496201.

[215] Chen, J. K., Tzou, D. Y., Beraun, J. E. (2006). A semiclassical two-temperature model for ultrafast laser heating. International Journal of Heat and Mass Transfer, 49(1–2), 307–316. doi:10.1016/j.ijheatmasstransfer.2005.06.022.

[216] Stegailov, V., Starikov, S., Norman, G. (2012). Atomistic simulation of laser ablation of gold: The effect of electronic pressure. AIP Conference Proceedings. doi:10.1063/1.3686424.

[217] Pisarev, V. V., Starikov, S. V. (2014). Atomistic simulation of ion track formation in UO2. Journal of Physics: Condensed Matter, 26(47), 475401. doi:10.1088/0953-8984/26/47/475401.

[218] Seaton, M. A., Todorov, I. T., Daraszewicz, S. L., Khara, G. S., Duffy, D. M. (2018). Domain decomposition of the two-temperature model in DLPOLY4. Molecular Simulation, 47(2–3), 180–187. doi:10.1080/08927022.2018.1511902.

[219] Daraszewicz, S. L., Giret, Y., Tanimura, H., Duffy, D. M., Shluger, A. L., amp; Tanimura, K. (2014). Determination of the electron–phonon coupling constant in tungsten. Applied Physics Letters, 105(2). doi:10.1063/1.4890413.

[220] Marinica, M.C., Ventelon, L., Gilbert, M.R., Proville, L., Dudarev, S.L., Marian, J., Bencteux, G. and Willaime, F. (2013). Interatomic potentials for modelling radiation defects and dislocations in tungsten. Journal of Physics: Condensed Matter, 25(39), 395502. doi:10.1088/0953-8984/25/39/395502.

[221] Stojanovic, N., Maithripala, D. H., Berg, J. M., Holtz, M. (2010). Thermal conductivity in metallic nanostructures at high temperature: Electrons, phonons, and the Wiedemann-franz law. Physical Review B, 82(7). doi:10.1103/physrevb.82.075418.

[222] Retrieved from https://docs.lammps.org/fix-viscous.html

[223] Zhigilei, Leonid V., Lin, Z., Ivanov, D. S. (2009a). Atomistic modeling of short pulse laser ablation of metals: Connections between melting, spallation, and phase explosion. The Journal of Physical Chemistry C, 113(27), 11892–11906. doi:10.1021/jp902294m.

[224] Larsen, P. M., Schmidt, S., Schiøtz, J. (2016). Robust structural identification via polyhedral template matching. Modelling and Simulation in Materials Science and Engineering, 24(5), 055007. doi:10.1088/0965-0393/24/5/055007.

[225] Stukowski, Alexander. (2009a). Visualization and analysis of atomistic simulation data with OVITO–The Open Visualization Tool. Modelling and Simulation in Materials Science and Engineering, 18(1), 015012. doi:10.1088/0965-0393/18/1/015012.

[226] Stukowski, A, Arsenlis, A. (2012). On the elastic–plastic decomposition of crystal deformation at the atomic scale. Modelling and Simulation in Materials Science and Engineering, 20(3), 035012. doi:10.1088/0965-0393/20/3/035012.

[227] Terekhin, P.N., Oltmanns, J., Blumenstein, A., Ivanov, D.S., Kleinwort, F., Garcia, M.E., Rethfeld, B., Ihlemann, J. and Simon, P.,(2021). Key role of surface plasmon polaritons in generation of periodic surface structures following single-pulse laser irradiation of a gold step edge. Nanophotonics, 11(2), 359–367. doi:10.1515/nanoph-2021-0547.

[228] Kaldos, A., Pieper, H. J., Wolf, E., Krause, M. (2004). Laser Machining in die making—a modern rapid tooling process. Journal of Materials Processing Technology, 155–156, 1815–1820. doi:10.1016/j.jmatprotec.2004.04.258.

[229] Vasilopoulou, M., Soultati, A., Georgiadou, D.G., Stergiopoulos, T., Palilis, L.C., Kennou, S., Stathopoulos, N.A., Davazoglou, D. and Argitis, P., (2014). Hydrogenated under-stoichiometric tungsten oxide anode interlayers for efficient and stable organic photovoltaics. J. Mater. Chem. A, 2(6), 1738–1749. doi:10.1039/c3ta13975a.

[230] Weinhardt, L., Blum, M., Bär, M., Heske, C., Cole, B., Marsen, B., Miller, E. L. (2008). Electronic surface level positions of wo3 thin films for photoelectrochemical hydrogen production. The Journal of Physical Chemistry C, 112(8), 3078–3082. doi:10.1021/jp7100286.

[231] Yang, Z., Liu, X., Tian, Y. (2019a). Corrigendum to "insights into the wettability transition of nanosecond laser ablated surface under ambient air exposure" [J. colloid interface sci. 533 (2019) 268–277]. Journal of Colloid and Interface Science, 539, 672. doi:10.1016/j.jcis.2018.11.090.

[232] He, H., Qu, N., Zeng, Y. (2016). Lotus-leaf-like microstructures on tungsten surface induced by one-step nanosecond laser irradiation. Surface and Coatings Technology, 307, 898–907. doi:10.1016/j.surfcoat.2016.10.033.

[233] Long, J., Zhong, M., Zhang, H., Fan, P. (2015a). Superhydrophilicity to superhydrophobicity transition of picosecond laser microstructured aluminum in ambient air. Journal of Colloid and Interface Science, 441, 1–9. doi:10.1016/j.jcis.2014.11.015.

[234] Hickman, J. W., Gulbransen, E. A. (1947). An electron diffraction study of oxide films formed on high temperature oxidation resistant alloys. Transactions of The Electrochemical Society, 91(1), 605. doi:10.1149/1.3071794.

[235] McCarroll, B. (1967). Chemisorption and oxidation: Oxygen on Tungsten. The Journal of Chemical Physics, 46(3), 863–869. doi:10.1063/1.1840818.

[236] Afify, H. H., Hassan, S. A., Obaida, M., Moussa, I., Abouelsayed, A. (2019a). Preparation, characterization, and optical spectroscopic studies of Nanocrystalline Tungsten Oxide WO3. Optics Laser Technology, 111, 604–611. doi:10.1016/j.optlastec.2018.10.036.

[237] Haase, T. A., Chan, A., Kihara, S., Broderick, N. G. R., Aguergaray, C. (2023). Tungsten oxide nanoparticle and aggregate formation through direct femtosecond laser ablation in air. Nano-Structures Nano-Objects, 33, 100935. doi:10.1016/j.nanoso.2022.100935.

[238] Ramana, C. V., Battu, A. K., Dubey, P., Lopez, G. A. (2020). Phase-control-enabled enhancement in hydrophilicity and mechanical toughness in nanocrystalline tungsten oxide films for energy-related applications. ACS Applied Nano Materials, 3(4), 3264–3274. doi:10.1021/acsanm.9b02576 .

[239] Praveen, K. M., Pious, C. V., Thomas, S., Grohens, Y. (2019). Relevance of plasma processing on polymeric materials and interfaces. Non-Thermal Plasma Technology for Polymeric Materials, 1–21. doi:10.1016/b978-0-12-813152-7.00001-9.

[240] Santos, L., Wojcik, P., Pinto, J.V., Elangovan, E., Viegas, J., Pereira, L., Martins, R. and Fortunato, E., (2015). Structure and morphologic influence of wo3nanoparticles on the electrochromic performance of dual-phasea-wo3/wo3inkjet printed films. Advanced Electronic Materials, 1(1–2), 1400002. doi:10.1002/aelm.201400002.

[241] Gulbransen, E. A., Andrew, K. F., Brassart, F. A. (1964a). Kinetics of oxidation of pure tungsten, 1150°–L615°C. Journal of The Electrochemical Society, 111(1), 103. doi:10.1149/1.2426043.

[242] Retrieved from https://www.researchgate.net/publication/283010587 Gruneisen's law for the classroom

[243] Shabalin, I. L. (2014). Ultra-High Temperature Materials I. doi:10.1007/978-94-007-7587-9.

[244] Yuan, W., Sizyuk, T. (2021). Ablation study in gold irradiated by single femtosecond laser pulse with electron temperature dependent interatomic potential and electron–phonon coupling factor. Laser Physics, 31(3), 036002. doi:10.1088/1555-6611/abdcb8.

[245] Plimpton, S. (1993). Fast Parallel Algorithms for Short-Range Molecular Dynamics. doi:10.2172/10176421.

[246] Schäfer, C., Urbassek, H. M., Zhigilei, L. V., Garrison, B. J. (2002). Pressure-transmitting boundary conditions for molecular-dynamics simulations. Computational Materials Science, 24(4), 421–429. doi:10.1016/s0927-0256(01)00263-4.

[247] Bévillon, E., Colombier, J. P., Recoules, V., Stoian, R. (2014). Free-electron properties of metals under ultrafast laser-induced electron-phonon nonequilibrium: A first-principles study. Physical Review B, 89(11). doi:10.1103/physrevb.89.115117.

[248] Anisimov, S. I., Rethfeld, B. (1997). Nonresonant Laser-Matter Interaction (NLMI-9). doi:10.1117/12.271674.

[249] Lin, Z., Zhigilei, L. V., Celli, V. (2008a). Electron-phonon coupling and electron heat capacity of metals under conditions of strong electron-phonon nonequilibrium. Physical Review B, 77(7). doi:10.1103/physrevb.77.075133.

[250] Bévillon, E., Stoian, R., Colombier, J. P. (2018). Nonequilibrium optical properties of transition metals upon ultrafast electron heating. Journal of Physics: Condensed Matter, 30(38), 385401. doi:10.1088/1361-648x/aad8e5.

[251] Anisimov, S. I., Rethfeld, B. (1997a). Nonresonant Laser-Matter Interaction (NLMI-9). doi:10.1117/12.271674.

[252] Oxygen concentration and defect structure in molybdenum and Tungsten. (2002). Metal Powder Report, 57(9), 39–40. doi:10.1016/s0026-0657(02)80434-9.

[253] Alkhamees, A., Liu, Y.-L., Zhou, H.-B., Jin, S., Zhang, Y., Lu, G.-H. (2009). First-principles investigation on dissolution and diffusion of oxygen in Tungsten. Journal of Nuclear Materials, 393(3), 508–512. doi:10.1016/j.jnucmat.2009.07.012.

[254] Sikka, V. K., Rosa, C. J. (1980). The oxidation kinetics of tungsten and the determination of oxygen diffusion coefficient in tungsten trioxide. Corrosion Science, 20(11–12), 1201–1219. doi:10.1016/0010-938x(80)90092-x.

[255] Milshtein, J. D., Gratz, E., Basu, S. N., Gopalan, S., Pal, U. B. (2013). Study of the two-step W/WO3 solar to fuel conversion cycle for syngas production. Journal of Power Sources, 236, 95–102. doi:10.1016/j.jpowsour.2013.02.038.

[256] Auerbach, D., Becker, C., Cowin, J., Wharton, L. (1977). Mechanism and speed of initial step of oxygen chemisorption-O2 on W. Applied Physics, 14(4), 411–413. doi:10.1007/bf00883448.

[257] Duwal, S., Kim, M., Yoo, C.-S. (2020). Seven-coordinated “metallic” wo3 at high pressures. The Journal of Physical Chemistry C, 124(49), 27040–27048. doi:10.1021/acs.jpcc.0c09005.

[258] Chen, J. K., Beraun, J. E., Grimes, L. E., Tzou, D. Y. (2002). Modeling of femtosecond laser-induced nonequilibrium deformation in metal films. International Journal of Solids and Structures, 39(12), 3199–3216. doi:10.1016/s0020-7683(02)00242-1.

[259] Bonse, J., Koter, R., Hartelt, M., Spaltmann, D., Pentzien, S., Höhm, S., Rosenfeld, A. and Krüger, J. (2015a). Tribological performance of femtosecond laser-induced periodic surface structures on titanium and a high toughness bearing steel. Applied Surface Science, 336, 21–27. doi:10.1016/j.apsusc.2014.08.111.

[260] Shinotsuka, H., Tanuma, S., Powell, C. J., Penn, D. R. (2015). Calculations of electron inelastic mean free paths. X. Data for 41 elemental solids over the 50EV to 200kev range with the relativistic full Penn algorithm. Surface and Interface Analysis, 47(9), 871–888. doi:10.1002/sia.5789.

[261] Retrieved from http://www.xpsfitting.com/2009/04/tungsten.html

[262] Retrieved from https : / / www . thermofisher . cn / cn / zh / home / materials - science / learning - center / periodic-table/non-metal/oxygen.html

[263] Chiu, N.-F., Tai, M.-J., Nurrohman, D. T., Lin, T.-L., Wang, Y.-H., Chen, C.-Y. (2021). Immunoassay-amplified responses using a functionalized mos2-based SPR Biosensor to detect Papp-A2 in maternal serum samples to screen for Fetal Down's syndrome. International Journal of Nanomedicine, Volume 16, 2715–2733. doi:10.2147/ijn.s296406.

[264] Gengenbach, T. R., Major, G. H., Linford, M. R., Easton, C. D. (2021). Practical guides for X-ray photoelectron spectroscopy (XPS): Interpreting the carbon 1s spectrum. Journal of Vacuum Science Technology A: Vacuum, Surfaces, and Films, 39(1). doi:10.1116/6.0000682.

* * *

Appendix A

XPS Analysis

A.1 XPS Acquisition

XPS data were extracted with the help of Dr. Gabriele Schatte of Queen's University, Canada, and Oltion Kodra of the National Research Council, Canada.

The XPS spectra were measured on a Kratos Axis Nova spectrometer equipped with an Al X-ray source. The tungsten sample was mounted onto a coated aluminum plate using double-sided adhesive Cu tape and was kept under a high vacuum (10^{-8} Torr) overnight inside the preparation chamber before it was transferred into the analysis chamber (ultrahigh vacuum, 10^{-9} Torr) of the spectrometer. The data is measured in the center of the spot using an aperture of 55 μm. The XPS data were collected using Al Kα radiation at 1486.69 eV (375 W, 25 mA), a charge neutralizer, and a delay-line detector (DLD) consisting of three multi-channel plates. Survey spectra were recorded from -5 to 1200 eV at a pass energy of 160 eV (number of sweeps: 3) using an energy step size of 1 eV and a dwell time of 200 ms. High-resolution spectra for O1s, C1s, and W4f were recorded in the appropriate regions at pass energy of 40 eV for 9 number of sweeps/dwell time: O1s, 12/300 ms; C1s, 15/300 ms; W4f, 10/300 ms; using an energy step size of 0.1 eV (resolution: 0.5472 eV). The analyzed area on the specimens was about 55 $\times$ 55 μm^2 (lens mode: FOV 2) at their positions.

The sampling depth for W for this particular energy of Al X-rays (1486.69 eV) is 6 nm. Given, the IMFP (Inelastic Mean Free Path) of W= 20.16 Å (calculated with QUASES-IMFP-TPP2M Ver. 3.0 TPP-2M formula calculator based on [260]) and sampling depth = 3 $\times$ IMFP. For WO_3 IMFP is 23.66 Å and hence the sampling depth is 7 nm.

A.2 Data used for XPS fitting

W 4f, O 1s, and C1s are the main peaks that were analyzed with CASA XPS software to have a good fit by adding appropriate component peaks. After fitting, by carefully choosing the FWHM, peak positions, line shapes, etc.

the quantitative information can be derived from the software.

W 4f has doublet peaks because of unfilled shells containing unpaired electrons in the f orbital. This means that there will be two peaks in XPS corresponding to a single oxidation state for the f orbital in W. For example W^{6+} oxidation state has two peaks corresponding to W^{6+} 7/2 and W^{6+} 5/2 due to spin orbit splitting. The 4f 7/2 and 4f 5/2 doublet separation is $\sim$ 2.18 eV and with area ratios of 4:3. W 4f spectrum contains an additional component corresponding to the W 5p 3/2 peak. But its RSF (Relative Sensitivity Factor, which is a factor used for deriving quantitative information) should be set to 0. The W 5p 3/2 peak is set at 5.5 eV above the W 4f 7/2 peak [261].

The O 1s peak is usually seen at 532 eV with the component peaks considered here are O=W, O=C, O-C, O-C=O. For C 1s, peak at 285 eV, the component peaks are C-C/C-H, C-O, C=O, and O-C=O and this peak is used for the calibration of the spectra. As you will see in the table below as the number of bonds between O and C increases the binding energy will increase, similar to O 1s and W 4f.

The FWHM is usually set between 0.3 and 1.5 for almost all the XPS peaks. The background is given a Shirley fit with line shapes GL (Gaussian Lorentzian) used for W 5p and C 1s and LA (asymmetric Lorentzian) for W 4f and O 1s peaks.

Approximate component peak positions and references			
Component Peaks	Binding Energy (eV)	std. deviation (eV)	References
W 4f: W^0 7/2	31.3	0.2	[261]
W 4f: W^{6+} 7/2	35.8	0.4	[261]
W 5p 3/2	36.87	-	[261]
O 1s: O=W	530.7	0.3	[261]
O 1s: O=C	533	-	[262]
O 1s: O-C	531.5 to 532	-	[262]
O 1s: O-C=O	533.2	-	[263]
C 1s: C-C/C-H	284.6 to 285	-	[264]
C 1s: C-O	(C-C/C-H)+(1.2 or 1.5)	-	[264]
C 1s: C=O	(C- O)+ (1.2 or 1.5)	-	[264]
C 1s: O-C=O	(C= O)+ (1.2 or 1.5)	-	[264]

Appendix B

Python Program

B.1 Algorithm for Python program solving 1-D heat equation

Step 1: Define fixed parameters like L =depth of W, nx =number of locations on W, (dx = L) / (nx - 1) (distance between two consecutive locations).

Step 2: interpolate the values of Cp and k from 300 K to 3000K.

Step 3: define, alpha = Cp/(k*density of W).

Step 4: set the initial temperature, define a source term with the fit equations at 500 ps or 1500 ps.

Step 5: Define the 1 D heat equation in a loop for each point of temperature.

Step 6: Define the no. of steps to compute.

Step 7: Define the time steps.

Step 8: print the time steps.

Step 9: plot the temperature-depth graph.

Step 10: print the temperature corresponding to the surface of tungsten.

B.2 Program

Created on Thu Oct 13 18:16:55 2022 @author: dop08358

```
import numpy
from matplotlib import pyplot
# Set the font family and size to use for matplotlib figures.
pyplot.rcParams['font.family'] = 'serif'
pyplot.rcParams['font.size'] = 16
# Set parameters.
L = 1.1e-6 # in meter depth of W
nx = 1000 # number of locations on the rod
```

dx = L / (nx - 1) # distance between two consecutive locations

#Finding alpha for each T by interpolating Cp and k
#alpha=k/(rho*Cp) :rho=19250 Kg/m*3 ,Cp=f1 J/Kg*K, k=f2 W/m-K
#interpolating Cp J/kg*K

import numpy as np
from scipy import interpolate
T_2 = [300,500,700,900,1100,1300,1500,1700,1900,2100,2300,2500,2700,2900,3100]
Cp = [131.31,138,141.6,144.8,148.33,152.31,156.95,162.4,168.7,176.18,184.75,194.59,205.81,218.53,232.86]

f1 = interpolate.interp1d(T_1, Cp, kind='cubic')

Tnew = np.arange(300,3100)
Cnew = f1(Tnew)

#interpolating k W/m-K
T_2= [300,400,500,600,800,1000,1200,1400,1600,1800,2000,2500,3000]
k = [174,159,146,137,125,118,112,108,104,101,98,91.4,84.5]
f2 = interpolate.interp1d(T_2, k, kind='cubic')
Tnew = np.arange(300,3000)
knew = f2(Tnew)
alpha = lambda x:f2(x)/(f1(x)*19250) #unit is m^2/s

# Define the locations along the rod.
x = numpy.linspace(0.0, L, num=nx)

# Set the initial temperature along the rod.
T0 = numpy.zeros(nx)
T0 =300+942/(1+np.exp ((x-330e-9)*0.017e9)) #in Kelvin,in meters
def ftcs(T0, nt, dt, dx, alpha):
Computes and returns the temperature along the rod after a provided number of time steps, given the initial temperature and thermal diffusivity. The diffusion equation is integrated using forward differencing in time and central differencing in space.

Parameters
T0 : numpy.ndarray
The initial temperature along the rod as a 1D array of floats.
nt : integer

The number of time steps to compute.

dt: float

The time-step size to integrate.

dx : float

The distance between two consecutive locations.

alpha : float

The thermal diffusivity of the rod.

Returns

T : numpy.ndarray

The temperature along the rod as a 1D array of floats.

```
T = T0.copy()
sigma = lambda T:alpha(T) * dt / dx**2
for n in range(nt):
T[1:-1] = (T[1:-1] + sigma(T[1:-1]) * (T[2:] - 2.0 * T[1:-1] + T[:-2]))
T[0]=(T[0] + sigma(T[1]) * (T[1] - 1.0 * T[0]))
T[-1]=(T[-1] + sigma(T[-1]) * (T[-2] - 1.0 * T[-1]))
return T

# Set the time-step size based on the CFL limit.
nt = 1000000 # number of time steps to compute
sigma = 0.06
dt = sigma * dx**2 / np.amax(alpha(Tnew))  time-step size in seconds
print(dt)

# Compute the temperature along the rod.
T = ftcs(T0, nt, dt, dx, alpha)
# Plot the temperature along the rod.
pyplot.figure(figsize=(6.0, 4.0))
pyplot.xlabel('Distance [m]')
pyplot.ylabel('Temperature [K]')
pyplot.grid()
pyplot.plot(x, T, color='C0', linestyle='-', linewidth=2)
pyplot.xlim(0.0, L)
pyplot.ylim(0.0, 4100)
Temp=np.interp(1e-9,x,T) #Temperature at x=...nm
print(Temp)
pyplot.show()
```

***